Improvement of Muon Neutrino Charged-Current Single Pion production cross-section measurement with the Upgraded ND280 at T2K

Jakkapu Mahesh

March 2024

ABSTRACT

To explore violation of neutrino CP symmetry, it is crucial to measure neutrino interactions with matter with unprecedented precision. The Tokai to Kamioka long-baseline neutrino oscillation experiment, T2K, is progressing with the development and construction of a new neutrino detector called SuperFGD, aiming for a detailed measurement of neutrino interactions. SuperFGD consists of approximately 2 million plastic scintillator cubes with a $1\times1\times1$ cm^3 each. SuperFGD detects charged particles by recording the deposit energy in the cubes. The scintillator light signal is read with WLS fibers passing in 3 directions. SuperFGD consists of over 56000 MPPC readout channels and new electronic boards called Front End Boards (FEB) were designed and developed to read signal data from the MPPCs. This detector allows for the capture of high position resolution of tracks with low energy threshold in three dimensions enabling a more detailed study of neutrino interactions.

In this thesis, we first describe the verification of the newly developed readout electronics boards for the SuperFGD detector. We developed a system required to efficiently verify the operation of multiple-channel readout electronics for about 56000 MPPCs in a short time. A new injection board (Kaladin) was developed so that we can multiply and inject the test signal from function generator into all 256 channels of FEB to speed up the FEB testing process. We successfully conducted the verification of around 240 electronics boards using this system, thereby completing the construction of the SuperFGD detector in time.

Next, we describe the evaluation of the measurement capability of neutrino interaction using the SuperFGD detector using the Monte Carlo simulations. The unique features of SuperFGD enable the measurement of low-momentum particles that were previously impossible with traditional scintillator detectors. In order to fully utilize the capabilities of the SuperFGD, optimization of the selection of muon neutrino charged-current interactions with a charged pion in the final-state (CC1π^+) was carried out, contributing to the improvement of neutrino oscillation measurements. Due to the size and geometry of SuperFGD cubes (1cm^3 each), the detection efficiency of short tracks has been improved with respect to the FGD in ND280 before the upgrade. Moreover, the timing precision of new electronics combined with track matching allowed reconstructing decay electron tracks coming from pion to muon to electron decay chain using the characteristic decay time of muon ($\sim$2.2μs). Implementing cuts based on this information we are able to reconstruct the 89% of the pion tracks stopping inside SuperFGD for CC1π^+ interactions with J-PARC neutrino beam. We found that momentum reconstruction threshold for charged pions is improved from 160 MeV in the original detector (FGD) to 50 MeV in SuperFGD. The CC1π selection efficiency was improved from $\sim$25% in FGD to $\sim$60% in SuperFGD while purity was improved from $\sim$60% in FGD to $\sim$68% in SuperFGD.

Table of Contents

List of Figures

List of Tables

Chapter 1

Introduction

1.1 Neutrino physics

Neutrinos are a type of elementary particle, carrying no electric charge and having a spin of 1/2. Particles with a spin of 1/2 are called fermions, and neutrinos are the only fermions that do not carry an electric charge. Figure 1.1 shows a table of known elementary particles. Neutrinos come in three types: electron neutrinos, muon neutrinos, and tau neutrinos. In this thesis, we discuss the crucial phenomenon namely 'neutrino oscillation' to understand the properties of neutrinos. First, we briefly discuss the introduction of the elementary particle neutrino and its

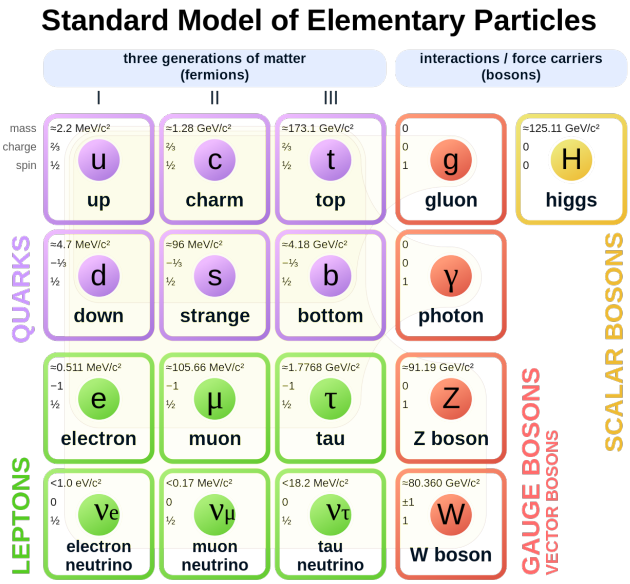

Figure 1.1: Particles in standard model[1].

discovery.

They were first postulated in by 1930 W. Pauli [2] to explain the electron energy spectrum in radioactive β decay:

$$ {}^{A}_{Z}X \rightarrow {}^{A}_{Z+1}X' + e^{-} \tag{1.1} $$

In this two-body decay, the electron energy spectrum is expected to be monochromatic; however it was observed to have a continuous distribution with the end point at predicted two-body value (Fig. 1.2). This prompted an addition of new neutral particle to conserve energy. According to Pauli, this charge less particle should have negligible mass to fit the missing energy

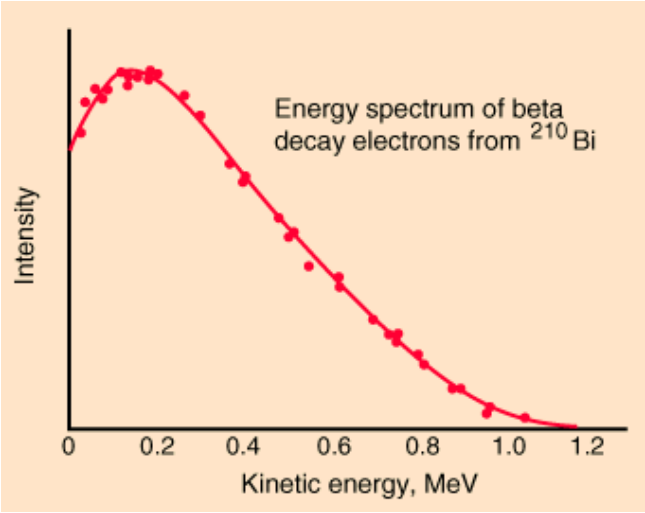

Figure 1.2: Electron energy spectrum from Bismuth beta decay. Energy from the decay is shared by electron (E_{el}) and neutrino (E_ν) [3].

from beta decay. Now we know that there is an anti-electron neutrino ($\bar{\nu}_e$) produced in the β decay. Based on Pauli's letter Enrico Fermi developed the theory of beta decay with electron and neutrino in the outgoing particles.

First observational evidence of neutrinos is published in 1956[4] by Cowan-Reines neutrino experiment using reactor neutrinos as source with water tanks as target along with scintillators to act as detectors. The anti-neutrinos from reactors have a small chance of interacting with proton the in water tanks to emit a neutron and a positron. The positron will then annihilate to produce two photons which can be detected by the scintillator detector to detect the anti-neutrinos. This result paved way for several new experiments to measure the properties of neutrinos.

Our sun is a constant source of neutrinos. In the period from 1970 to 1994 Homestake experiment[5] has taken the solar neutrino data to study the neutrino flux. The experimental apparatus contains 615 tons of C_2Cl_4 and chlorine is used to detect neutrinos mainly from $^8B \rightarrow {}^8B^* + e^+ + \nu_e$ reaction in sun via $^{37}Cl + \nu_e \rightarrow {}^{37}Ar + e^-$. Using this method the measured flux of neutrinos is about 30% of the expected flux. This mismatching observation is come to be known as famous "Solar neutrino problem"[6].

Kamiokande experiment is made of water tank surrounded by PMTs to study proton decay that is later repurposed to detect solar neutrinos using cherenkov radiation. In 1987, Kamiokande detected neutrinos from super nova explosion. Kamiokande has also observed the deficit in solar neutrino events.

Super-Kamiokande experiment[7] discovered neutrino oscillations, where muon neutrino (ν_μ) is measured with less flux than expected value (ν_μ disappearance), with the atmospheric neutrino measurement in 1998, which implied that at least 2 out of 3 neutrinos have non-zero mass. The observed neutrino flux from above the earth is almost double the flux coming from other side of earth and this deficit in flux of neutrinos passing through the earth is explained by muon neutrinos oscillating to tau neutrinos during travel. Together with K2K accelerator experiment looking at ν_μ disappearance, SK is able to constrain θ_{23} and Δm^2_{23}.

SNO[8], another water based detector, and it is sensitive to solar neutrinos. SNO was also able to confirm neutrino oscillations from ν_e to ν_μ or ν_τ. KamLAND[6] is designed to detect $\bar{\nu}_e$ coming from reactors. Together SNO, KamLAND and Super-Kamiokande played vital roles in constraining θ_{12} and Δm^2_{21}. Solar neutrino problem can also be explained by

neutrino oscillations.

1.2 Neutrino oscillations

Neutrinos have flavor and mass states. Since neutrinos can be seen as particles and waves at the same time. Mass states, we can refer to them as $V_{1,2,3}$, have unique masses and propagate through space as waves. The flavor states are the observable state of neutrinos and each of them are superimposition of mass states. Due to the quantum nature of neutrinos, they can change into a different flavor of neutrino spontaneously. This phenomenon is called "neutrino oscillation".

Neutrino flavor and mass eigenstates are related as follows:

$$|V_\alpha\rangle = \sum_i U^*_{\alpha j} |V_i\rangle \tag{1.2}$$

where $|V_\alpha\rangle$ (α = e, μ, τ) is a flavor eigenstate and $|V_i\rangle$ (j=1,2,3) is a mass eigenstate of neutrino. The 3×3 unitary matrix ($U_{\alpha j}$) called Pontecorvo–Maki–Nakagawa–Sakata (PMNS) matrix gives mixing of neutrino flavor and mass eigenstates as follows:

$$U_{PMNS} = \begin{pmatrix} 1 & 0 & 0 \\ 0 & c_{23} & s_{23} \\ 0 & -s_{23} & c_{23} \end{pmatrix} \begin{pmatrix} c_{13} & 0 & s_{13}e^{-i\delta_{CP}} \\ 0 & 1 & 0 \\ -s_{13}e^{-i\delta_{CP}} & 0 & c_{13} \end{pmatrix} \begin{pmatrix} c_{12} & s_{12} & 0 \\ -s_{12} & c_{12} & 0 \\ 0 & 0 & 1 \end{pmatrix} \tag{1.3}$$

where $c_{jk} = \cos\theta_{jk}$, $s_{jk} = \sin\theta_{jk}$, θ_{jk} is the mixing angle and δ_{CP} is CP violating phase. The flavor state of neutrino with energy (E) and momentum (p) after travelling for a distance (L) and time (t) can be written as:

$$|V_\alpha\rangle (t, L) = \sum_j U^*_{\alpha j} e^{-iE_j t + ip_j L} |V_j\rangle \tag{1.4}$$

and the neutrino flavor observed by the detector is:

$$\langle V_\beta| = \sum_j U_{\beta j} \langle V_\beta| \tag{1.5}$$

The oscillation probability of neutrinos from flavor α to β is then becomes:

$$\begin{aligned} P_{\alpha\beta} &= |\langle V_\beta | V_\alpha(t, L)\rangle|^2 \\ P_{\alpha\beta} &= \sum_{j,k} U^*_{\alpha j} U_{\beta j} U_{\alpha k} U^*_{\beta k} e^{-i(E_j - E_k)t + i(p_j - p_k)L} \end{aligned} \tag{1.6}$$

Neutrinos travel near speed of light and have negligible mass compared to their energy. Assuming $p_j \approx p_k \equiv p \approx E$, $t \approx L$ for natural units and $E_j = \sqrt{p^2 + m_j^2} \approx p + \frac{m_j^2}{2E}$, we get:

$$P_{\alpha\beta} = \sum_{j,k} U^*_{\alpha j} U_{\beta j} U_{\alpha k} U^*_{\beta k} e^{-i\frac{\Delta m^2_{jk} L}{2E}} \tag{1.7}$$

1.2.1 2 flavor oscillation

We first discuss the simple case of oscillation between 2 flavors of neutrinos. The simplest neutrino mixing is between 2 flavors with $U = \begin{bmatrix} \cos\theta & \sin\theta \\ -\sin\theta & \cos\theta \end{bmatrix}$, using this matrix the probability of ν_μ oscillating to ν_e can be written using previous equation as follows:

$$\begin{aligned} P_{\mu e} &= U_{\mu 1}^2 U_{e1}^2 + U_{\mu 2}^2 U_{e2}^2 + U_{\mu 1} U_{e1} U_{\mu 2} U_{e2} (e^{i\frac{\Delta m^2 L}{2E}} + e^{-i\frac{\Delta m^2 L}{2E}}) \\ &= 2\sin^2\theta\cos^2\theta - 2\sin^2\theta\cos^2\theta\cos\frac{\Delta m^2 L}{2E} \\ &= \sin^2 2\theta \sin^2\frac{\Delta m^2 L}{4E} \end{aligned} \tag{1.8}$$

Using units of neutrino travel length (km), Δm^2 (ev^2) and E (GeV) we get the factor of 1.27.

$$P_{\mu e} = \sin^2 2\theta \sin^2\frac{1.27\Delta m^2 L}{E} \tag{1.9}$$

1.2.2 Matter effect

The oscillation probability derived so far is valid for neutrinos travelling in vacuum but for usual detectors we use neutrinos might travel through earth and undergo scattering while interacting with the matter. Matter in neutrino path influences neutrinos in two ways:

- **W exchange**: Neutrino (ν_α) can exchange W boson with corresponding lepton (l_α). Since earth contains only electrons, this W boson exchange can only happen with ν_e or $\bar{\nu}_e$ flavors. The interaction potential is proportional to the electron density (N_e) in matter and Fermi coupling constant (G_F).

$$V_W = \begin{cases} +\sqrt{2} G_F N_e & \text{for } \nu_e \\ -\sqrt{2} G_F N_e & \text{for } \bar{\nu}_e \end{cases} \tag{1.10}$$

- **Z exchange**: All flavors for neutrinos can interact with electrons, protons and neutrons in matter via Z boson exchange. Since the Z coupling to electrons and protons is equal but opposite overall effect cancels out between the two due to similar number density of proton and electrons in earth. Only remaining contribution is the neutral component proportional to neutron density (N_n) and Fermi coupling constant.

$$V_Z = \begin{cases} -\frac{\sqrt{2}}{2} G_F N_n & \text{for } \nu \\ +\frac{\sqrt{2}}{2} G_F N_n & \text{for } \bar{\nu} \end{cases} \tag{1.11}$$

Hamiltonian for the neutrino propagation in vacuum can be written as: $\mathcal{H}_{\text{vac}} |\nu_j\rangle = E_j |\nu_j\rangle$. To extract the hamiltonian we need to solve for this for each parameter of the matrix using $\langle\nu_\alpha| \mathcal{H}_{\text{vac}} |\nu_\beta\rangle$.

$$\begin{aligned} \langle\nu_\alpha| \mathcal{H}_{\text{vac}} |\nu_\beta\rangle &= \sum_j \langle U_{\alpha i}| \mathcal{H}_{\text{vac}} |U_{\beta j}\rangle \\ &= \sum_j U_{\alpha j}^* U_{\beta j} E_j \langle\nu_j|\nu_j\rangle \\ &= \sum_j U_{\alpha j}^* U_{\beta j} E_j \sqrt{p^2 + m_j^2} \end{aligned} \tag{1.12}$$

using $U = \begin{bmatrix} \cos\theta & \sin\theta \\ -\sin\theta & \cos\theta \end{bmatrix}$, The Hamitonian $\mathcal{H}_{\text{vac}}$ becomes,

$$\mathcal{H}_{\text{vac}} = \frac{\Delta m^2}{4p} \begin{bmatrix} -\cos 2\theta & \sin 2\theta \\ \sin 2\theta & \cos 2\theta \end{bmatrix} + \left(p + \frac{m_1^2 + m_2^2}{4p} \right) \begin{bmatrix} 1 & 0 \\ 0 & 1 \end{bmatrix} \tag{1.13}$$

Since the hamiltonian can be shifted by any multiple of unitary matrix and approximating $p \approx E$

$$\mathcal{H}_{\text{vac}} = \frac{\Delta m^2}{4E} \begin{bmatrix} -\cos 2\theta & \sin 2\theta \\ \sin 2\theta & \cos 2\theta \end{bmatrix} \tag{1.14}$$

The hamiltonian for matter effect is the sum of vacuum, W and Z interaction contributions. W effect is only for ν_e whereas Z is uniform for all flavors and a digonal matrix.

$$\begin{aligned} \mathcal{H}_{\text{Matter}} &= \mathcal{H}_{\text{vac}} + V_W \begin{bmatrix} 1 & 0 \\ 0 & 0 \end{bmatrix} + V_Z \begin{bmatrix} 1 & 0 \\ 0 & 1 \end{bmatrix} \\ &= \mathcal{H}_{\text{vac}} + V_W \begin{bmatrix} 1 & 0 \\ 0 & -1 \end{bmatrix} + V_W \begin{bmatrix} 1 & 0 \\ 0 & 1 \end{bmatrix} + V_Z \begin{bmatrix} 1 & 0 \\ 0 & 1 \end{bmatrix} \end{aligned} \tag{1.15}$$

Like before, the contribution from factors of unitory matrix can ignored in the hamiltonian using terms from unitary matrix.

$$\begin{aligned} \mathcal{H}_{\text{Matter}} &= \mathcal{H}_{\text{vac}} + V_W \begin{bmatrix} 1 & 0 \\ 0 & 0 \end{bmatrix} + V_Z \begin{bmatrix} 1 & 0 \\ 0 & 1 \end{bmatrix} \\ &= \frac{\Delta m^2}{4E} \begin{bmatrix} -\left(\cos 2\theta - \frac{V_W/2}{\Delta m^2/4E} \right) & \sin 2\theta \\ \sin 2\theta & \left(\cos 2\theta - \frac{V_W/2}{\Delta m^2/4E} \right) \end{bmatrix} \\ &= \frac{\Delta m^2}{4E} \begin{bmatrix} -(\cos 2\theta - x) & \sin 2\theta \\ \sin 2\theta & (\cos 2\theta - x) \end{bmatrix} \end{aligned} \tag{1.16}$$

where,

$$x = \frac{V_W/2}{\Delta m^2/4E} = \frac{2\sqrt{2} G_F N_e E}{\Delta m^2} \tag{1.17}$$

To get a simpler similar to vacuum hamiltonian we can replace the terms as follows,

$$\begin{aligned} \cos 2\theta_M &= (\cos 2\theta - x) X \\ \sin 2\theta_M &= (\sin 2\theta) X \\ \Delta m_M^2 &= \frac{\Delta m^2}{X} \\ \implies X &= \frac{1}{\sqrt{\sin^2 2\theta + (\cos 2\theta - x)^2}} \end{aligned} \tag{1.18}$$

then hamiltonian can be rewritten as,

$$\mathcal{H}_{\text{Matter}} = \frac{\Delta m_M^2}{4E} \begin{bmatrix} -\cos 2\theta_M & \sin 2\theta_M \\ \sin 2\theta_M & \cos 2\theta_M \end{bmatrix} \tag{1.19}$$

The oscillation probability is then,

$$P_M \ (\nu_\mu \to \nu_e) = \sin^2 2\theta_M \sin^2 \frac{\Delta m_M^2 L}{4E} \tag{1.20}$$

Compared to vacuum oscillation, matter effect can dramaticaly change the probability function depending the value of x which has contributions from matter density, neutrino energy and mass difference between eigen states.

1.2.3 3 flavor oscillation

Here we 3 flavor oscillation Neutrino oscillation probability of 3 flavor can be expressed as:

$$P\ (\nu_\alpha \to \nu_\beta / \bar{\nu}_\alpha \to \bar{\nu}_\beta) = \delta_{\alpha\beta} - 4\sum_{j>i} Re(U_{\alpha i}U^*_{\beta i}U^*_{\alpha j}U_{\beta j}) \sin^2\left(\frac{\Delta m^2_{ij}L}{4E}\right) \mp 2\sum_{j>i} Im(U_{\alpha i}U^*_{\beta i}U^*_{\alpha j}U_{\beta j}) \sin\left(\frac{\Delta m^2_{ij}L}{2E}\right) \quad (1.21)$$

Here, oscillation happens from flavor α to β. The neutrino and anti-neutrino flavor is denoted by $\mp$.

Probability of $\nu_\mu \to \nu_e$ appearance including matter effect can be expressed as follows:

$$\begin{aligned} P\ (\nu_\mu \to \nu_e) = {} & 4C^2_{13}S^2_{13}S^2_{23}\sin^2\phi_{31} \\ & + 8C^2_{13}S_{12}S_{13}S_{23}(C_{12}C_{23}\cos\delta - S_{12}S_{13}S_{23})\cos\phi_{32}\sin\phi_{31}\sin\phi_{21} \\ & - 8C^2_{13}C_{12}C_{23}S_{12}S_{13}S_{23}\sin\delta\sin\phi_{32}\sin\phi_{31\sin\phi_{21}} \\ & + 4S^2_{12}C^2_{13}(C^2_{12}C^2_{23} + S^2_{12}S^2_{23}S^2_{13} - 2C_{12}C_{23}S_{12}S_{23}S_{13}\cos\delta)\sin^2\phi_{21} \\ & - 8C^2_{13}S^2_{13}S^2_{23}(1 - S^2_{13})\frac{2\sqrt{2}G_F n_e L}{4E}\cos\phi_{32}\sin\phi_{31} \end{aligned} \quad (1.22)$$

, where $C_{jk} = \cos\theta_{jk}$, $S_{jk} = \sin\theta_{jk}$ and $\phi_{jk} = \frac{\Delta m^2_{jk}L}{E}$ For the calculation of probability for anti neutrinos $\delta \to -\delta$ and $a \to -a$. In this probability function, $\sin\delta$ is the CP violating term and matter effect is expressed in $\frac{2\sqrt{2}G_F n_e L}{4E}$ term. The matter effect could be large or small depending on the experimental parameters L, E and matter density.

1.3 Current status of neutrino oscillation

Neutrino oscillation can be understood by 6 parameters that are 3 mixing angles $(\theta_{12}, \theta_{23}, \theta_{13})$, 2 mass differences $(\Delta m^2_{12}, \Delta m^2_{23})$ and CP violating phase (δ_{CP}). Various experiments around the world contribute towards these measurements. The sensitivity for each parameter depends on the experimental approach, for example accelerator long baseline experiments are designed to be suitable for measuring θ_{23} and Δm^2_{23} whereas solar neutrino measurements provide better understanding of θ_{12} due to L/E value. The latest experimental results of these parameters are listed in Table. 1.1

There are many important questions in neutrino oscillations yet to be answered.

- Neutrino mass ordering: Order of neutrino mass eigen values plays a crucial role in the oscillation probability. They are expressed in terms of mass square difference in the probability calculations. Normal ordering (NO) or Inverted ordering (IO) (Fig. 1.3) is yet to be determined. This also plays a role in the neutrinoless double beta decay $(0\nu\beta\beta)$ search. $0\nu\beta\beta$ search experiments are looking to see if neutrinos are majorana particle which means particle and anti-particle are the same. In the case of neutrinos being majorana particle the double beta decay may not have any neutrinos in the final state hence the name. $0\nu\beta\beta$ experiments can probe the absolute mass of neutrinos and their mass hierarchy too.

- CP violating phase: Only imaginary part of the oscillation probability and is expressed as the difference of neutrino and anti-neutrino oscillation probability. CP violation in lepton

sector could explain the matter-antimatter asymmetry in our universe. Lepton asymmetry could originate from heavy majorana neutrinos and translate to baryonic asymmetry to explain universe mostly made of matter with very little antimatter. Knowing the CP violating phase via neutrino experiments will improve the models to explain the matter-antimatter asymmetry.

- θ_{23} Octant: θ_{23} is measured experimentally by looking at the ν_μ disappearance probability. Long baseline experiments such as T2K have sensitivity to $\sin^2 2\theta_{23}$. Calculating θ_{23} here introduces ambiguity in the octant since there are two solutions (larger of smaller than $\pi/4$).

Table 1.1: Neutrino oscillation parameters for normal and inverted ordering. Error values corresponding to one sigma[9].

	Normal ordering	Interveted ordering
$\theta_{12}/^\circ$	$34.3^{+1.0}_{-1.0}$	$34.3^{+1.0}_{-1.0}$
$\theta_{23}/^\circ$	$49.26^{+0.79}_{-0.79}$	$49.46^{+0.60}_{-0.97}$
$\theta_{13}/^\circ$	$8.53^{+0.13}_{-0.12}$	$8.58^{+0.12}_{-0.14}$
$\frac{\Delta m^2_{21}}{10^{-5}eV^2}$	$7.50^{+0.22}_{-0.20}$	$7.50^{+0.22}_{-0.20}$
$\frac{\lvert\Delta m^2_{31}\rvert}{10^{-3}eV^2}$	$+2.55^{+0.02}_{-0.03}$	$+2.45^{+0.02}_{-0.03}$
$\delta_{CP}/^\circ$	194^{+24}_{-22}	284^{+26}_{-28}

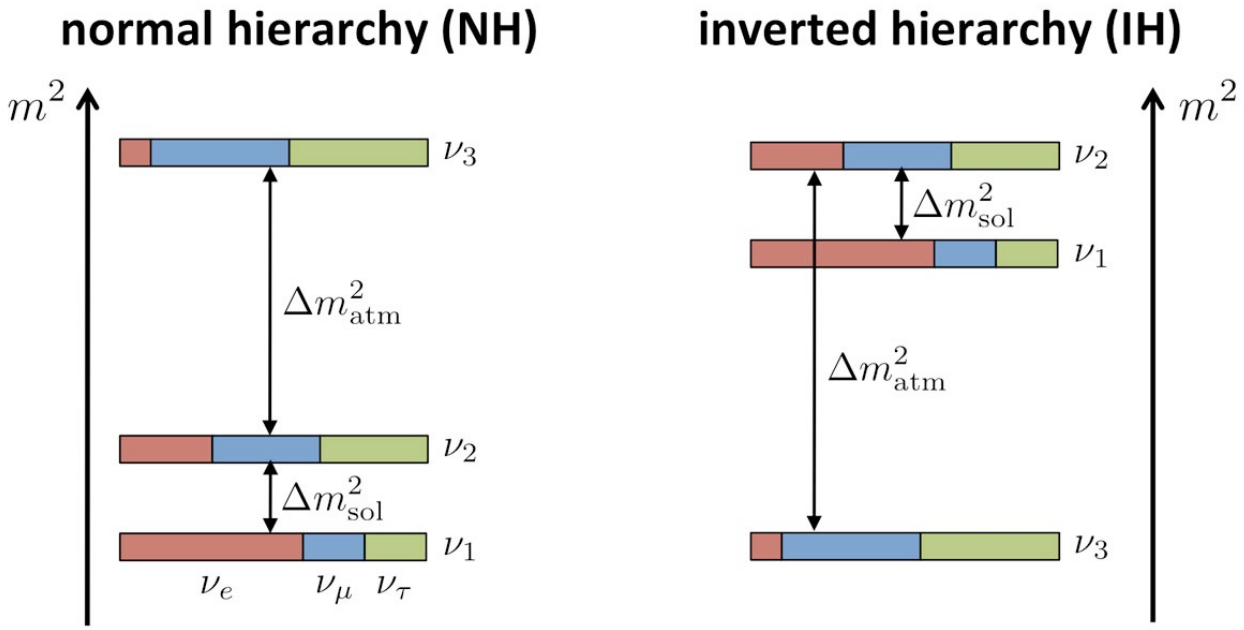

Figure 1.3: Neutrino mass ordering[10].

1.3.1 Neutrino interaction with matter

Neutrinos are neutral particles that can only undergo weak interaction. Majority of the neutrinos pass through the matter without any interaction. Neutrinos can only be studied indirectly, by measuring particles produced from neutrino interactions.

Neutrino can undergo two types of interactions with nucleus: Charged Current (CC) and Neutral Current (NC). The Feynman diagrams for these processes are shown in Fig. 1.4. In Fig. 1.4 (a) ν_μ interacts with a neutron in nucleus by exchanging W boson to produce μ^- and proton. The flavor of the neutrino can be identified by measuring the outgoing charged lepton. In Fig. 1.4 (b) ν_μ and neutron exchanges Z boson to give out ν_μ and neutron. In this case we cannot experimentally determine the neutrino flavor because there is no outgoing charged lepton.

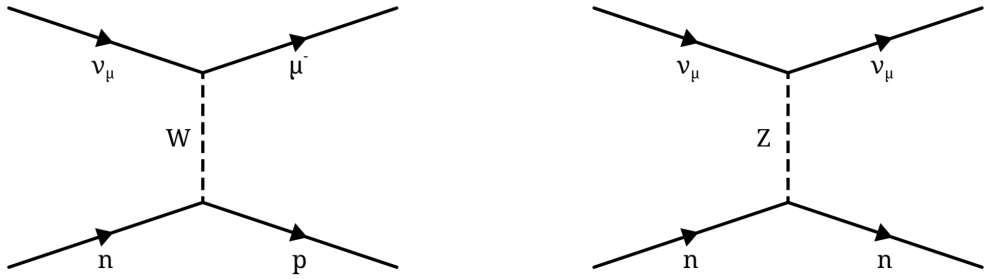

(a) Charged-Current **(b)** Neutral-Current

Figure 1.4: Feynman diagrams for charged current quasi-elastic (a) and neutral current elastic interactions (b).

Neutrino interaction can be further classified into 5 categories: Quasi-Elastic scattering (QE), Resonant pion production (RES), Coherent pion production, Deep inelastic scattering (DIS) and Meson exchange current (MEC). Cross-section contributions of these interactions are shown in Fig. 1.5.

1. Quasi-elastic scattering When neutrino has low energy, it may not be able to excite nucleon; therefore it simply transfers the 4 momentum to the nucleon. It results in a lepton and a nucleon in the final state. This interaction is called quasi elastic interaction in charged current because unlike elastic interaction, it can have different incoming and outgoing particles.

$$\begin{aligned} \nu_\mu n &\to \mu^- p & \bar{\nu}_\mu p &\to \mu^+ n \\ \nu_\mu n &\to \nu_\mu n & \bar{\nu}_\mu p &\to \bar{\nu}_\mu p \\ \nu_\mu p &\to \nu_\mu p & \bar{\nu}_\mu n &\to \bar{\nu}_\mu n \end{aligned} \tag{1.23}$$

2. Resonant pion production When a neutrino has sufficient energy, it can excite the nucleon, then the excited nucleon or delta decays into nucleon and a charged or a neutral pion. This process is called resonant pion production (Fig. 1.6). The outgoing particles are lepton, recoil nucleon and a pion.

There are 6 charged current RES:

$$\begin{aligned} \nu_\mu p &\to \mu^- p\pi^+ & \bar{\nu}_\mu n &\to \mu^+ n\pi^- \\ \nu_\mu n &\to \mu^- p\pi^0 & \bar{\nu}_\mu p &\to \mu^+ n\pi^0 \\ \nu_\mu n &\to \mu^- n\pi^+ & \bar{\nu}_\mu p &\to \mu^+ p\pi^- \end{aligned} \tag{1.24}$$

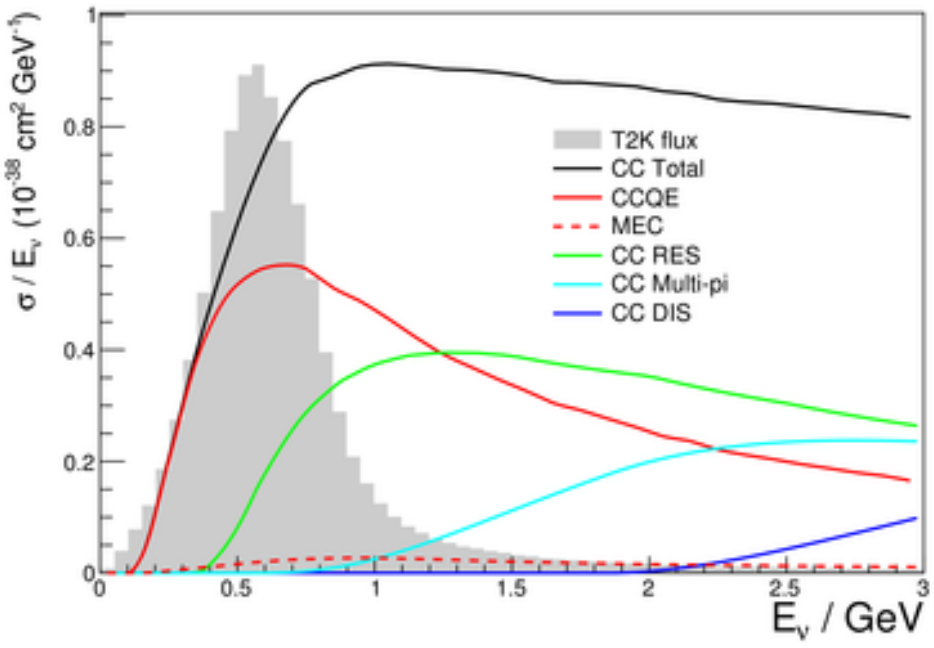

Figure 1.5: ν_μ cross-section contribution from CC interaction modes.

and 8 neutral current RES:

$$\begin{aligned} \nu_\mu p &\to \nu_\mu p\pi^0 & \bar{\nu}_\mu p &\to \bar{\nu}_\mu p\pi^0 \\ \nu_\mu p &\to \nu_\mu n\pi^+ & \bar{\nu}_\mu p &\to \bar{\nu}_\mu n\pi^+ \\ \nu_\mu n &\to \nu_\mu p\pi^- & \bar{\nu}_\mu n &\to \bar{\nu}_\mu p\pi^- \\ \nu_\mu n &\to \nu_\mu n\pi^0 & \bar{\nu}_\mu n &\to \bar{\nu}_\mu n\pi^0 \end{aligned} \tag{1.25}$$

Majority of the pion contribution comes from these modes with T2K beam flux. The important modes for this thesis study are those with a charged pion and charge lepton in the outgoing particles.

3. Coherent pion production A neutrino can interact with a nucleus. In addition to outgoing lepton, it produces pions and a small fraction of energy is transferred to the nucleus itself. Unlike resonant pion production, we do not have any nucleons in the out-going tracks. Interactions of this type are the following :

$$\begin{aligned} \nu_\mu N &\to \mu^- N\pi^+ & \bar{\nu}_\mu N &\to \mu^+ N\pi^- \\ \nu_\mu N &\to \nu_\mu N\pi^0 & \bar{\nu}_\mu N &\to \bar{\nu}_\mu N\pi^0 \end{aligned} \tag{1.26}$$

where N represents nucleus.

4. Deep inelastic scattering DIS occurs when high energy neutrinos probe inside nucleons and interact with the individual quarks inside them. A shower of hadrons is produced as an outcome of this interaction. At lower energy, DIS could produce a pion in addition to outgoing lepton and recoil nucleon; therefore, it can resemble resonant pion production. At higher energy there can be multiple hadrons in the outgoing particles.

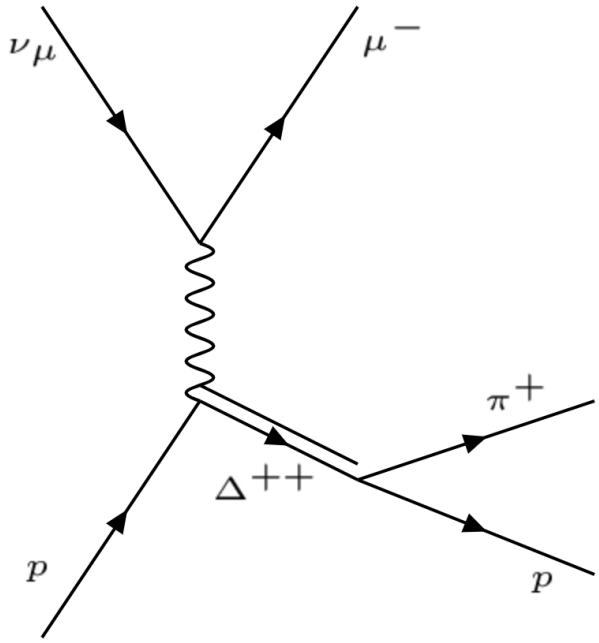

Figure 1.6: Feynman diagram of Resonant pion production.

5. Meson exchange current Unlike the Quasi-elastic interaction, another type of interaction can take place due to nuclear effects; a neutrino interacts with a pair of nucleons in a nucleus, and two nucleons appear in the final state. These are called two-particle two-hole (2p2h) process [11], and dominated by Meson exchange current (MEC) (Fig. 1.7).

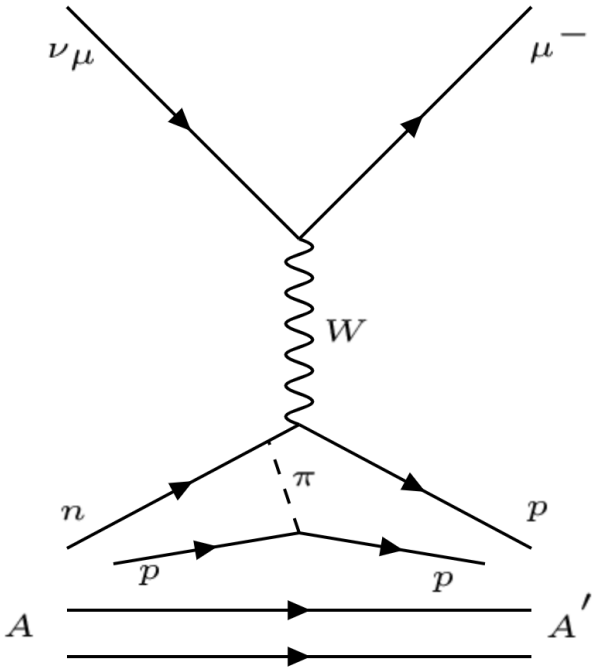

Figure 1.7: Feynman diagram of Meson Exchange Current.

In order to study neutrino interactions experimentally, we need to heavily rely on the measurement of final-state particles to "reconstruct" the incoming neutrino information. Therefore,

instead of categorizing the measurements by interaction types, we categorize them based on final state particles as follows:

- CC0π - a charged lepton, nucleon/nucleons and no charged pions as products.
- CC1π - a charged lepton, nucleon/nucleons and one charged pion as products.
- CC other - Rest of the CC topologies.

Topology of CC0π final-state with one nucleon is the same as CCQE. Due to nuclear effects after the neutrino interaction, pions produced in CCnπ can re-interact and not appear in the final state. They introduce contribution into CCQE like topology from non-CCQE modes in experimental measurement.

1.4 Latest result of T2K

T2K is Tokai to Kamioka long baseline neutrino oscillation experiment [12] located in Japan. T2K started from 2010 and so far it successfully confirmed the ν_e appearance. The current goal is to measure the neutrino oscillation parameters θ_{13}, θ_{23}, Δm^2_{32} and CP violating phase in $\nu_\mu \to \nu_e$ ($\bar{\nu}_\mu \to \bar{\nu}_e$) appearance and $\nu_\mu \to \nu_\mu$ ($\bar{\nu}_\mu \to \bar{\nu}_\mu$) disappearance. Initial ν_μ ($\bar{\nu}_\mu$) beam is produced at Japan Proton Accelerator Research Complex (J-PARC) [13] located in Tokai. A near detector complex composed of off-axis (ND280) and on-axis (INGRID) detectors is placed 280 meters downstream of the beam production point to measure neutrino interactions and flux before oscillation. Far detector, Super Kamiokande (SK) [14], is located at Kamioka 295 km away from the neutrino beam origin (Fig. 1.8) to measure neutrino flavor after oscillation. Details of the experimental apparatus will be discussed in Ch. 2.

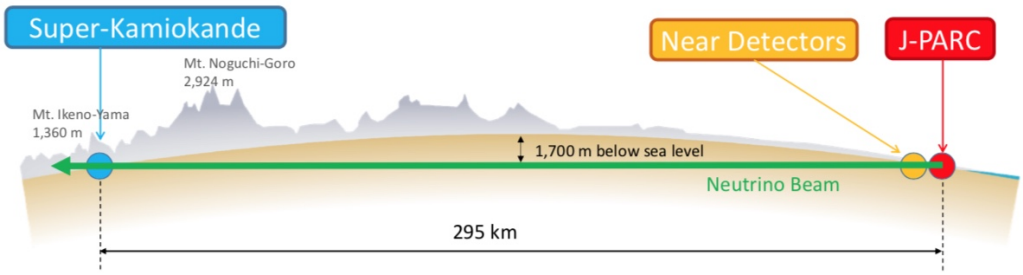

Figure 1.8: Overview of T2K experiment.

T2K oscillation analysis utilizes ND280 and SK detected neutrino events to extract oscillation parameters. Equations (1.27) and (1.28) show the number of neutrino events (N^ν) at near detector and far detector as function of these parameters: neutrino beam flux (ϕ_{flux}), interaction cross-section with the detector material (σ), mass of the detector (M), detector efficiency (ϵ_{det}) and neutrino oscillation probability (P_{osc}).

$$N_\nu^{ND}(E_\nu) = \phi_{flux}^{ND} \times \sigma^{ND} \times M^{ND} \times \epsilon_{det}^{ND} \tag{1.27}$$

$$N_\nu^{FD}(E_\nu) = \phi_{flux}^{FD} \times \sigma^{FD} \times M^{FD} \times \epsilon_{det}^{FD} \times P_{osc} \tag{1.28}$$

P_{osc} is extracted from measurement of $N^\nu_{FD}(E_\nu)$ by constraining ϕ_{flux} and σ utilizing the measurement of $N^\nu_{ND}(E_\nu)$. T2K analysis separates events of near detector measurement into various samples as shown in Table. 1.2. The detectors FGD1 and FGD2 are the scintillator volumes for

neutrino interaction and track detection. From this table, 1π samples are utilized in oscillation analysis to constrain σ. Furthermore, T2K oscillation analysis recently started utilizing CC1π in addition to CC0π events for far detector analysis. In CC1π case, the reconstruction looks for two delayed michel electrons, one from muon and another from pion via Cherenkov rings in the SK detector. Adding 1π sample increased overall statistics by ∼30% (Fig.1.9). Therefore, understanding of CC1π is crucial to improve T2K oscillation analysis.

Table 1.2: Near detector(ND) samples used for T2K oscillation analysis with the detector efficiency and purity[15].

Selection	Topology	Detector	Eff. (%)	Pur. (%)
ν_μ in ν-mode	0π	FGD1	48.0	71.3
		FGD2	48.0	68.2
	$1\pi^+$	FGD1	29.0	52.5
		FGD2	24.0	51.3
	Other	FGD1	30.0	71.4
		FGD2	30.0	71.2
$\bar{\nu}_\mu$ in $\bar{\nu}$-mode	0π	FGD1	70.0	74.5
		FGD2	69.0	72.7
	$1\pi^-$	FGD1	19.3	45.4
		FGD2	17.2	41.0
	Other	FGD1	26.5	26.3
		FGD2	25.2	26.0
ν_μ in $\bar{\nu}$-mode	0π	FGD1	60.3	55.9
		FGD2	60.3	55.8
	$1\pi^+$	FGD1	30.3	44.4
		FGD2	26.0	44.8
	Other	FGD1	27.4	68.3
		FGD2	27.1	69.5

The main function of near detector in the oscillation analysis is to constrain the systematic uncertainties in the neutrino events detected at far detector. Table. 1.3 shows the errors divided into event samples with contribution from ND constrained and unconstrained along with detector uncertainties of SK. Improving the near detector efficiency and acceptance will translate into improved errors in the T2K analysis. Figure 1.10 shows the improvement of $\sin\delta_{CP} = 0$ exclusion as a function of protons on target (POT) for 2016 and newer systematics (≈4%), better systematics allows us to achieve results with fewer statistics.

T2K continuously strive for improvement in neutrino oscillation and cross-section measurements by accumulating more beam data and novel approach in analysis to reduce systematics. Figure 1.11 show the δ_{CP} plots from the latest published results.

1.5 Outline of this thesis

In this thesis, the work done on the upgraded near detector of T2K long baseline neutrino experiment is explained. Chapter 2 will introduce the various components in T2K experiment such as beam, near detectors and far detector. Chapter 3 will give an overview of the ND280 upgrade focusing on the new detector installed as a part of upgrade. The detector (SFGD) is first of its kind in the world capable of precise vertex and 3D track reconstruction for neutrino

Table 1.3: Systematic uncertainties of Far detector using ND constraints for various samples[16]. Samples are divided into CC0π(1R) and CC1π^+ for ν_μ and ν_e detection. Errors are separated as Flux+Xsec constrained and unconstrained by ND, uncertainties by far detector(SK), secondary interactions(SI) and photo-nuclear effects(PN).

	1R(μ)		MR	1R(e)			
Error source (%)	FHC	RHC	FHC CC1π^+	FHC	RHC	FHC CC1π^+	FHC/RHC
Flux+Xsec (ND constr)	2.7	2.6	2.2	2.8	2.7	3.4	2.3
Xsec (ND unconstr)	0.7	2.4	1.4	2.9	3.3	2.8	3.7
SK+SI+PN	2.0	1.7	4.1	3.1	3.8	13.6	1.2
Total	3.4	3.9	4.9	5.2	5.8	14.3	4.5

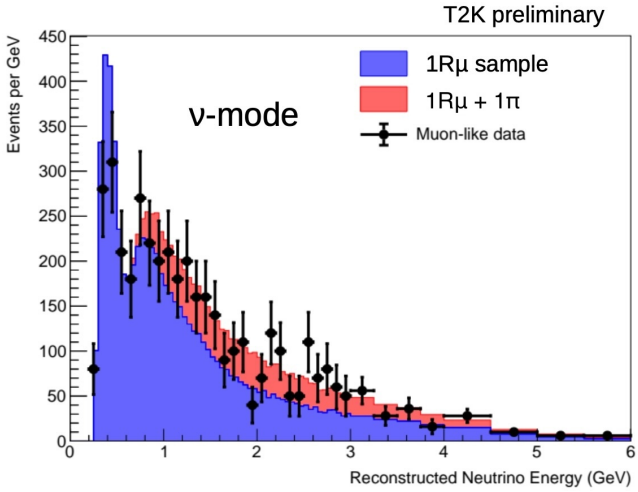

Figure 1.9: Neutrino distribution at SK for 1 muon and 1 muon+1 pion reconstruction samples. There is a $\sim$ 30% increase in statistics by including CC1π^+ sample[16].

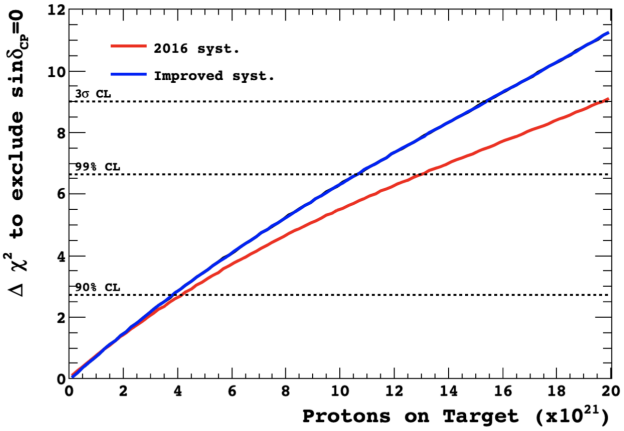

Figure 1.10: Sensitivity to exclusion of CP conserving hypotheses as a function of POT. Improved systematics are projected to 3.8 %[17].

interactions. Brand-new electronics are designed and mass-produced for SFGD. Chapter 4 of this thesis contain the work done to evaluate these electronic boards by using a test bench. A new injection board is designed and developed by me to be used in the test bench. A precise 3D tracking detector brings a lot of benefits to the event analysis with better energy deposition and

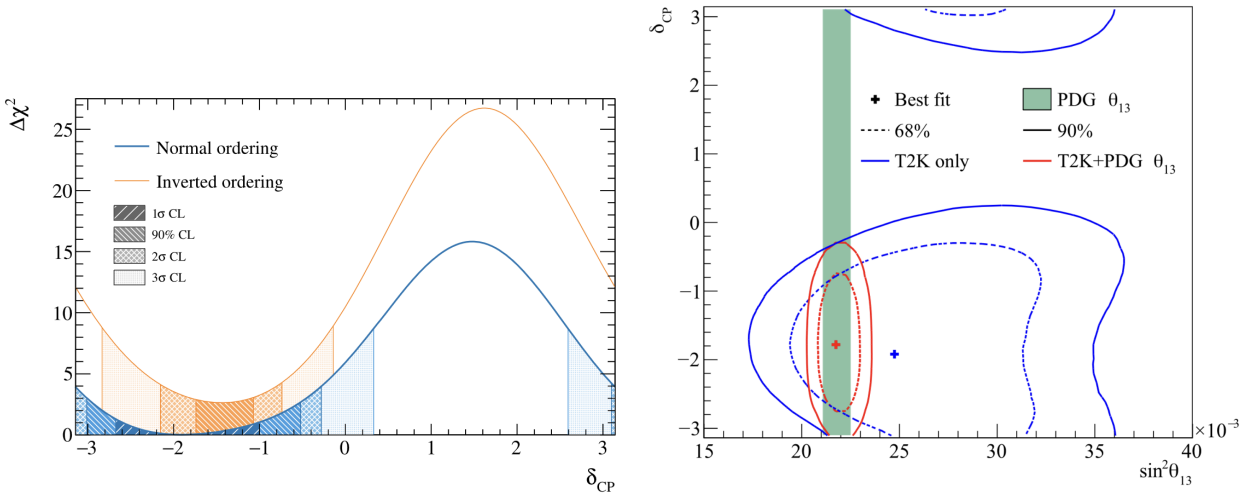

(a) χ^2 distribution of δ_{CP} for various confidence intervals.

(b) $\sin^2\theta_{13}$-δ_{CP} with (red) and without (blue) reactor constaints.

Figure 1.11: Latest results of T2K[18].

directional information of the charged particles but at the same the method of reconstructing track information from electronic readouts is challenging and requires new methods of data analysis. Chapter 5 explains the work done while developing near detector software for event reconstruction mainly focusing on improvement of CC1π^+ event selection in comparison of older and new detector performance. We will summarize the results in chapter 6.

Chapter 2

T2K Experiment

This chapter will explain the various components of T2K experiment.

2.1 Neutrino beam

The ν_μ ($\bar{\nu}_\mu$) beam originates from J-PARC utilizing the 3 accelerators. H^- beam is produced and accelerated in linear accelerator (LINAC) up to 400 MeV kinetic energy. H^- is then injected to the rapid cycling synchrotron (RCS), converted to proton, and accelerated to 3 GeV. Proton beam is transferred to the main ring (MR) and accelerated to 30 GeV. Beam is then extracted in 2.48 s[1] intervals (spills), bent 80° towards SK, delivered to neutrino target (graphite) and mainly produce pions. Each spill contains 8 bunches. Pions are focused towards SK using horn magnets [19]. Neutrino and anti-neutrino mode of operation is controlled by the polarity of horn magnets. They focus π^- (π^+) which decays into μ^- (μ^+) and $\bar{\nu}_\mu$ (ν_μ). Beam center direction is 2.5° off-axis from ND280 and SK locations (Fig. 2.1). This allows the detectors to detect neutrinos in the energy range 0.5 GeV - 0.7 GeV with sharp peak around 0.6 GeV. The setup maximizes the neutrino oscillation probability for 295 km flight distance (Fig. 2.2). Further details of neutrino beam for T2K is described in [19]. T2K started data taking in January 2010 and, by April 2023, accumulated about 3.83×10^{21} POT (protons on target) with maximum beam power of 541 kW (Run 12) for continuous operation (Fig. 2.3).

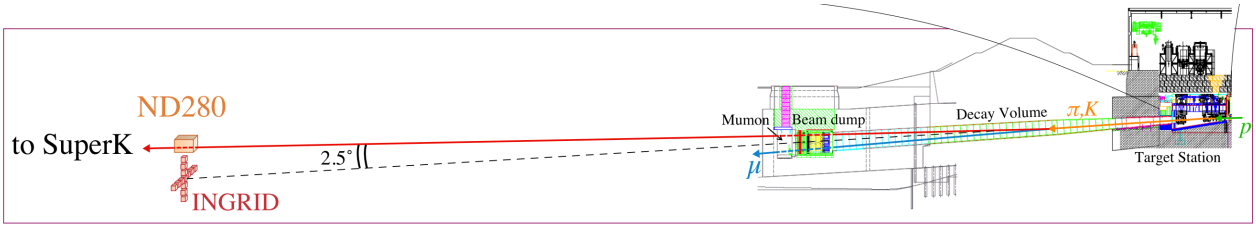

Figure 2.1: J-PARC neutrino beam operation.

2.2 Near detectors

T2K has three near detectors located at 280 m downstream of the beam target; ND280, INGRID and WAGASCI-BabyMind. The layout of these detectors is shown in Fig. 2.4.

[1]Repetition time was reduced to 1.36 seconds from 2023

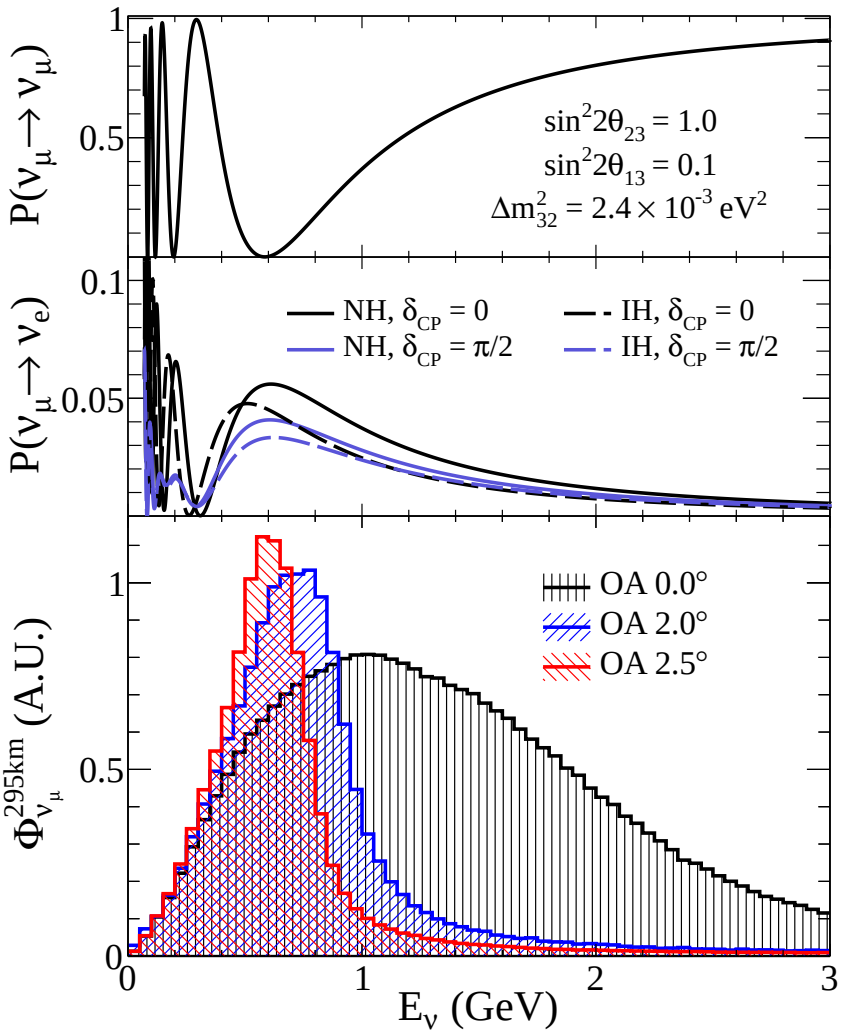

Figure 2.2: Oscillation probability as a function of energy (top and middle) and neutrino energy spectrum for various off-axis angles.

2.2.1 ND280

ND280 is located 280 m from the neutrino target and 2.5° off the beam central direction. ND280 detects particles produced by neutrino interactions to obtain neutrino information before oscillation such as neutrino beam flux, energy spectra and cross section. ND280 is enclosed in a 0.2 T magnet in horizontal direction to identify charged particles and calculate momentum from curvature. The target detectors and trackers are contained in a basket ; three time projection chambers (TPC), two scintillator bar detectors called fine grained detector (FGDs) sandwiched between TPCs, a π^0 detector (P0D) placed at the upstream position. Outside the basket, electromagnetic calorimeters (side-ECALs) and side muon detectors (SMRD) are located. Fig. 2.5 shows the full structure and components of ND280.

Pi-zero detector (P0D)

P0D is located in the upstream position of ND280 magnet basket. P0D consists of 80 scintillator planes made of triangular plastic scintillator bars aligned in horizontal and vertical directions, interleaved with fillable passive water targets and lead and brass sheets. WLS fibers and MPPCs are used to read out the deposited energy information. P0D is optimized to study neutral current (NC) π^0 production $\nu_\mu + n \rightarrow \nu_\mu + n + \pi^0 + X$. P0D contributes to the systematic uncertainty reduction in the SK event analysis by providing information for NCπ0

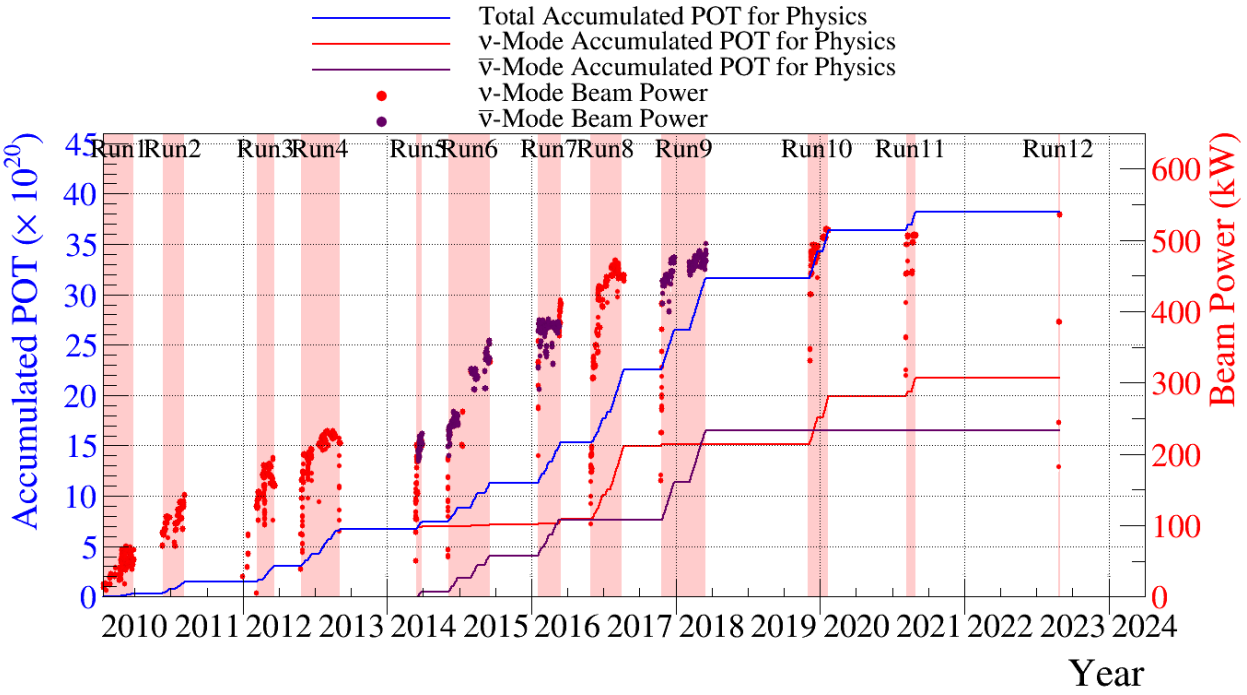

Figure 2.3: Accumulated proton on target so far for T2K.

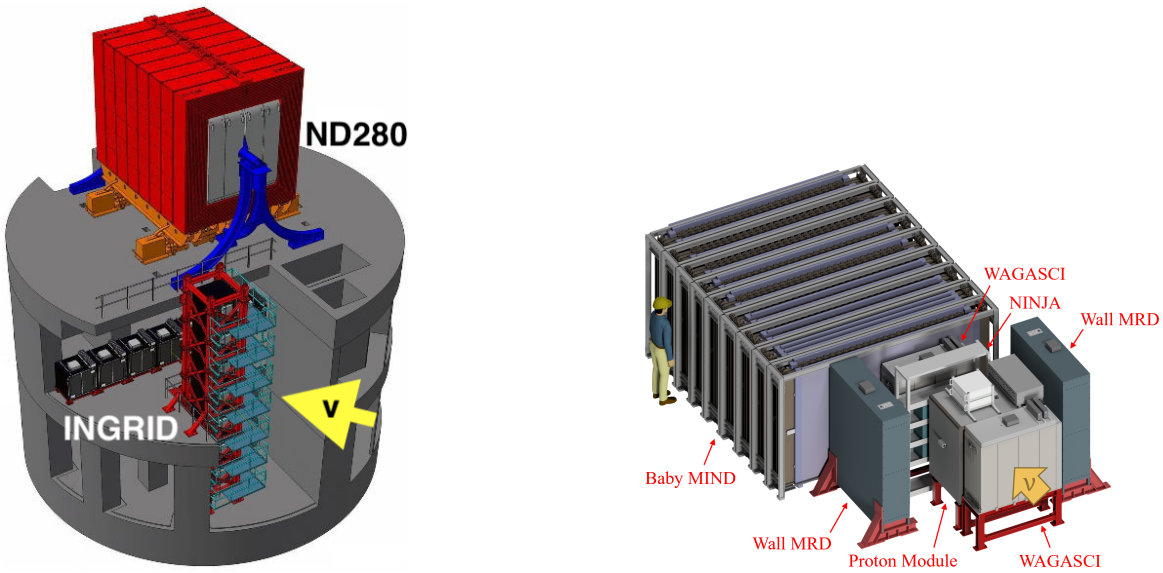

(a) ND280 and INGRID.

(b) WAGASCI BabyMind detector.

Figure 2.4: T2K near detectors.

background events, π^0 decayed gammas produce electrons which can be confused with CC produced electron, since P0D and SK contain water target.

TPCs

ND280 has three time projection chambers (TPCs) located downstream of P0D, each one consisting of approximately four cubic meters of argon gas inside electric and magnetic fields. The TPCs are designed to study momentum, charge information and provide dE/dx information of particles passing through them.

FGDs

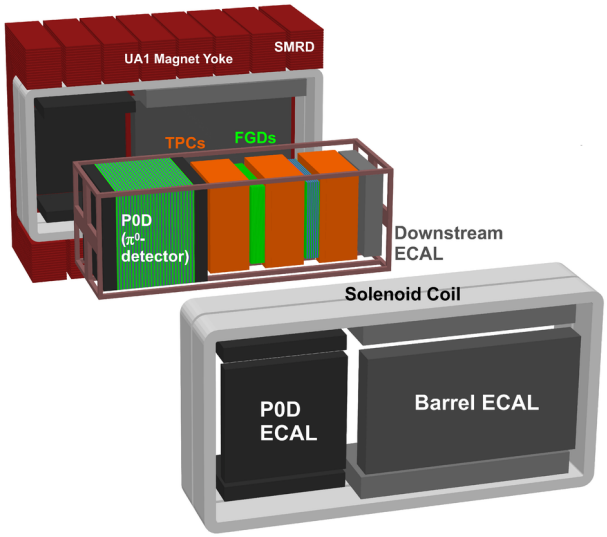

Figure 2.5: ND280 detector structure.

ND280 has two fine-grained detectors (FGD) sandwiched between three TPCs. FGD1 and FGD2 have same dimensions. FGD1 consist of plastic scintillator bars arranged alternatively in horizontal and vertical directions with WLS fibers and MPPCs attached to readout deposited energy. FGD2 has water target planes interleaved with plastic scintillator planes. The segmenting allows for track detection. Combined with TPCs, FGDs are optimized for particle identification and detecting CC interactions like $\nu_\mu n \to \mu^- p$. Main objectives are to measure the muon and electron neutrino fluxes and spectra as well as neutrino interaction cross-sections.

Electromagnetic calorimeter (ECAL)

Electromagnetic calorimeter (ECAL) surrounds P0D and tracker detectors. It consists of scintillator bars, WLS fibers and MPPCs for readout, interleaved with lead sheets. Its goal is to detect any charged particles entering or leaving the inner detector volume and to measure γs from π^0.

ECAL is made of 13 independent modules: 6 P0D ECAL (2 top, 2 bottom and 2 side), 6 barrel ECAL modules (2 top, 2 bottom and 2 side), and one downstream ECAL at the downstream of the tracker.

Side muon range detector (SMRD)

Side muon range detector consists of 440 scintillator modules installed in the magnet iron yoke gaps. Each scintillator bar has a WLS fiber attached to MPPC. Objectives of SMRD are to detect high angle muons produced in the inner detector volume which TPC cannot detect, act as a trigger for cosmic muon and detect particles from neutrino interactions in near detector pit walls and magnet.

2.2.2 INGRID

INGRID [20] measures on-axis neutrino beam intensity and profile. INGRID consists of 14 submodules arranged in the plane perpendicular to the neutrino beam direction (Fig. 2.6). Each module in INGRID weights 7.1 tons and consists of 9 iron plates and 11 scintillator tracking planes alternatively. Iron acts as the target volume for neutrino interaction. Scintillator tracking plane is made of one layer of 24 plastic scintillator bars in horizontal direction glued to another layer of 24 scintillator bars in vertical direction. WLS fibers collect scintillation light in each

bar and MPPC is connected to one end of the fiber.

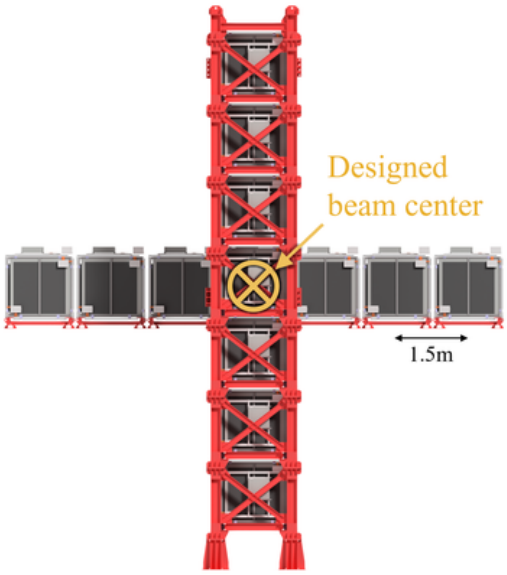

Figure 2.6: INGRID overview.

2.2.3 WAGASCI BabyMIND

The purpose of WAter-Grid-SCintillator-Detector (WAGASCI)[21] is to reduce the cross section uncertainty in T2K analysis due to difference in target material between near detector (CH) and far detector (water). WAGASCI detector is made up of alternating CH and water targets surrounded by Muon Range Detectors (MRD) to measure escaping particle momentum. Baby-MIND[22] is Magnetized Iron Neutrino Detector used to measure momentum and identify the charge of particles coming from interactions in WAGASCI. It consists of 33 magnetized metal plate and 18 scintillator modules to measure hit position and curvature of the particles.

2.3 Far detector (SK)

Super-Kamiokande (SK) is a 39.3 m diameter and 41.4 m height water tank with 50,000 tons of ultrapure water, composed of two segments, inner and outer detectors (Fig. 2.7). Inner detector, optically separated from the outer detector, has 11,129 photo multiplier tube (PMT) detectors evenly placed along the wall. Each of them have a diameter of 50 cm and facing inward. The outer detector has 1,885 of 20 cm PMTs, facing outward. The outer detector acts as veto detector for cosmic and geo backgrounds. SK has excellent electron/muon identification capability. When a neutrino interacts with the water, via charge current, it produces respective charged lepton and associated hadrons. These particles produce Cherenkov radiation in the water if the velocity is greater light velocity in the water and PMTs detect the generated light. Using the Cherenkov light distribution, the particle can be identified with momentum and direction, to reconstruct neutrino energy.

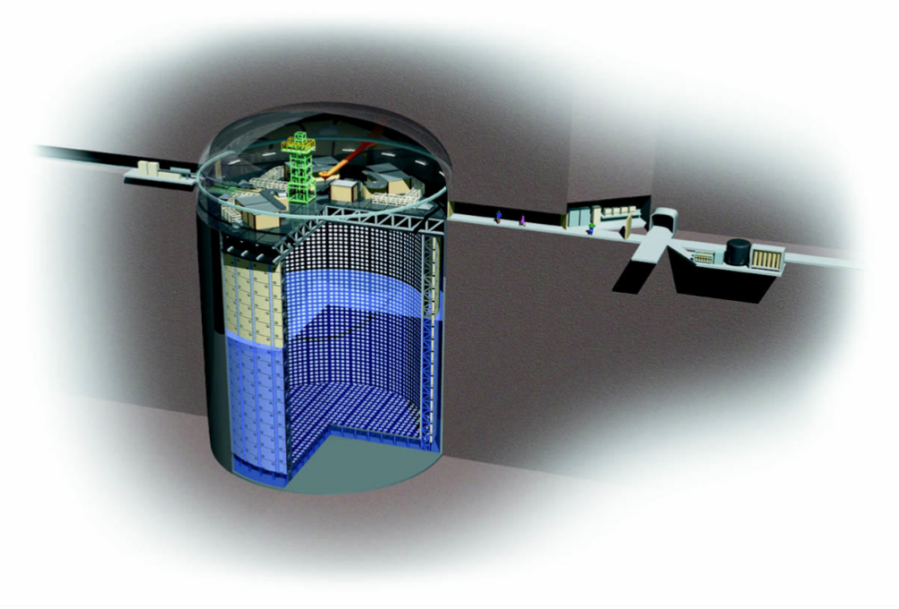

Figure 2.7: Super Kamiokande Overview.

Chapter 3

ND280 upgrade and Super Fine Grained Detector (SFGD)

ND280 is proved to have excellent particle identification and momentum reconstruction capabilities by using particle track information in FGDs and TPCs. The flux and cross-section uncertainties have been significantly improved from ∼13% to ∼3.4% for $\nu_\mu CC0\pi$ analysis when ND280 information is included for the T2K oscillation analysis.

Drawback of the current ND280 setup is that the angular acceptance of tracks is good for mainly forward going tracks and drops significantly when the track angle is above ∼50° with respect to the beam direction. On the other hand SK has uniform particle detection efficiency as a function of the production angle. (Fig. 3.2). Uniform efficiency is important to reduce the model a dependency of neutrino interaction model in the near to far detector extrapolation. In order to improve performance of cross-section measurement and systematic errors of T2K oscillation analysis, ND280 detector is upgraded[23].

3.1 ND280 upgrade detector design

P0D in the current ND280 (Fig. 2.5), except P0D-ECAL, will be replaced with a super fine-grained detector (SFGD) and two high-angle time projection chambers (HAT) placed top and bottom of SFGD. Time of flight detectors (TOF) will enclose SFGD and HATs. Fig. 3.1 shows the upgraded detector configuration. There are no changes in the downstream and barrel section of ND280.

Some new detectors are installed in ND280 and are taking neutrino data. These detectors are expected to have better position resolution and acceptance of particles, and to reduce the systematic uncertainties. They also give a better understanding of neutrino interaction models reducing also the presence of mis-modeling and consequent biases in the measurement of the neutrino oscillation probability. SFGD gives the resolution which can significantly improve the neutrino interaction vertex studies along with better reconstruction and understanding of low momentum tracks in all directions (Fig.3.3 and Fig. 3.4). HATs give better coverage for tracks escaping from SFGD and helps in identifying and reconstructing their momentum. (Fig.3.5).

3.2 Super Fine-Grained Detector (SFGD)

SFGD[24] is a three-dimensional-readout scintillator detector designed to improve the particle detection efficiency at high angle and position resolution of tracks. SFGD consists of about

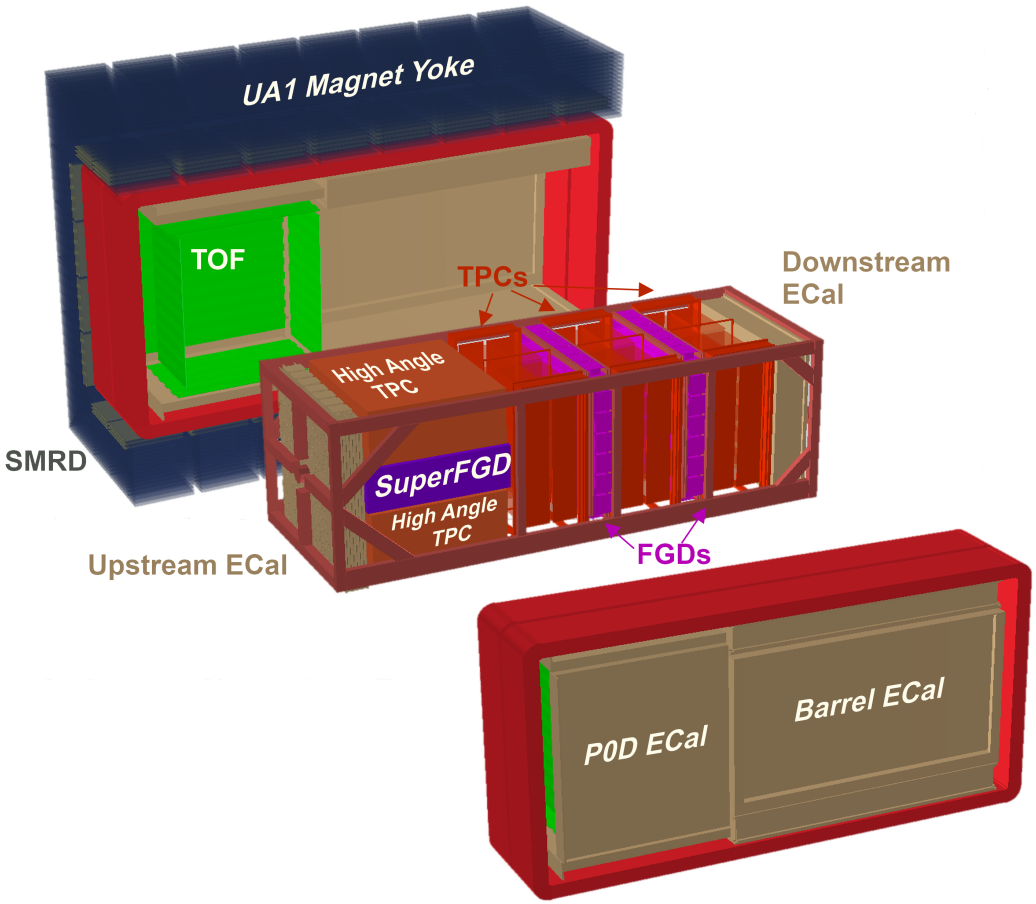

Figure 3.1: ND280 Upgrade.

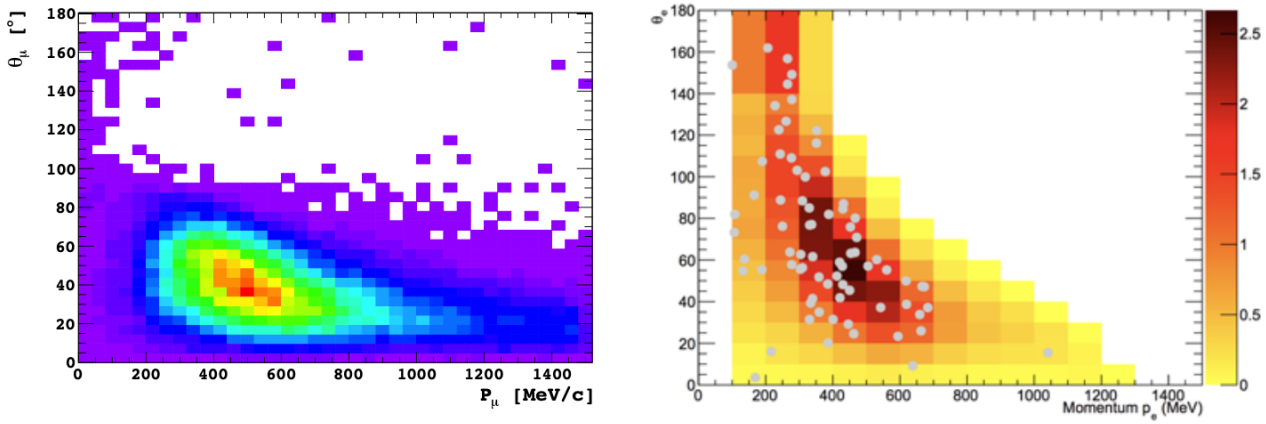

Figure 3.2: Reconstructed momentum and angle for electron at SK (right) and muons at ND280 (left).

2 million optically isolated plastic scintillator cubes, with size of 1 cm×1 cm×1 cm, are arranged in a cuboid structure, 192, 56, 184 cubes in x, y, z direction respectively. Each cube has 3 orthogonal holes drilled through it to have wavelength shifting (WLS) fibers passing through them (Fig. 3.6). At one end of each fiber, multi pixel photon counter (MPPC) is attached to measure number of photons produced by charged particles. In the ND280 upgrade configuration, it will replace upstream P0D, except P0D-ECAL. It consists of ∼2 million scintillator

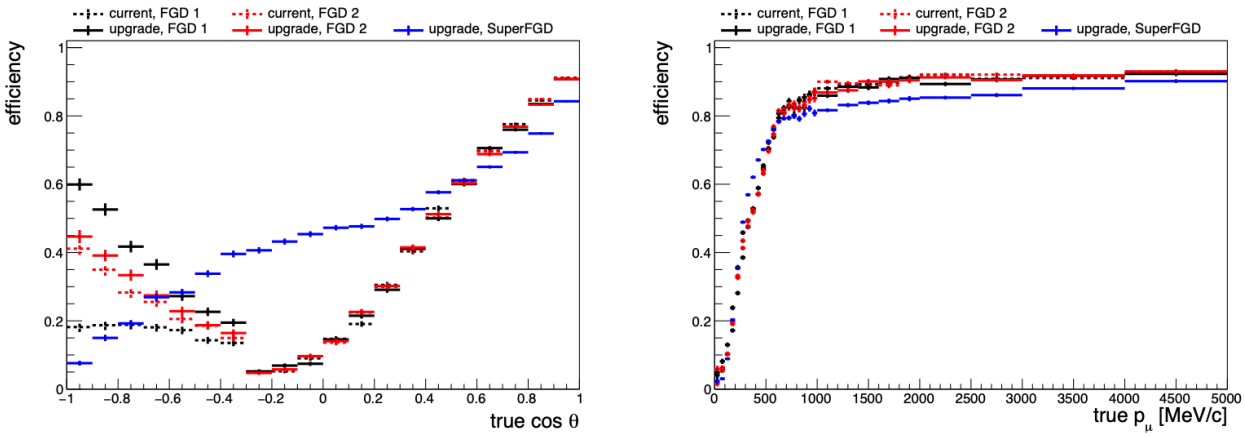

Figure 3.3: ν_μ Charged-Current (CC) selection efficiency as a function of muon angle with beam direction (left) and momentum (right).

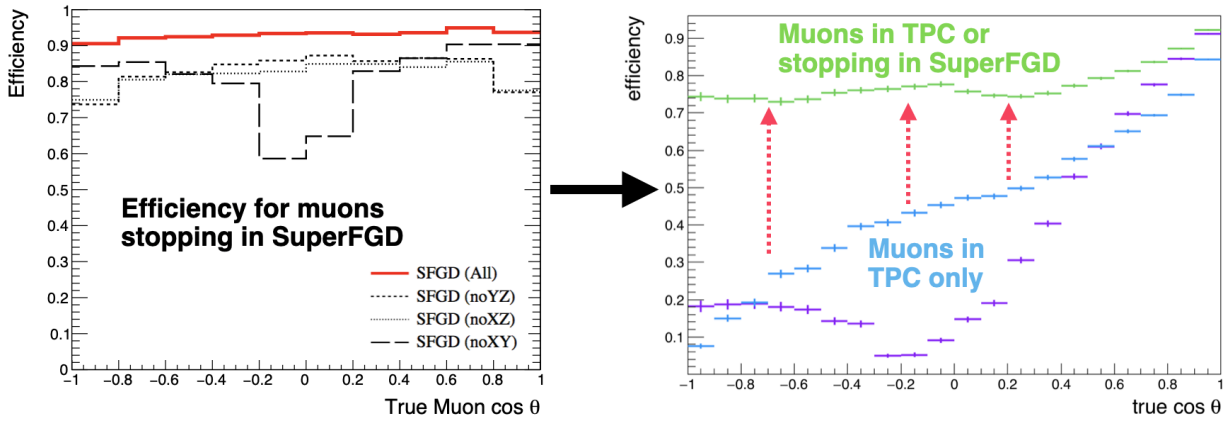

Figure 3.4: SFGD reconstruction efficiency for stopping muons (left) and improvement to muons stopping in TPC (right).

cubes with size of 1 cm×1 cm×1 cm. Number of cubes in x, y, z layers are 192×56×184, respectively. Cubes are drilled with 3 orthogonal hole (1.5 mm diameter), 3 mm from the outer edge, to insert WLS fibers through them (Fig. 3.6). Tables 3.1, 3.2 and 3.3 lists the useful design parameters for SFGD scintillator cube, fiber and readout MPPCs, respectively.

About 2 million cubes have to be assembled with WLS fibers passing in 3 directions. A small misalignment in the cubes could stop the WLS fibers from going all the way through the layer. A process called "fishing line method" is adopted to make the assembly smooth. A plastic wire of diameter ∼1.3 mm is inserted to make the skeletal plane of a cube layer (192×184). This arranges the cubes in a rigid manner. Then the plastic wires are replaced with WLS fibers and process is repeated for next layer along Y direction. In Y direction, some metallic wires are used to keep the cubes in position.

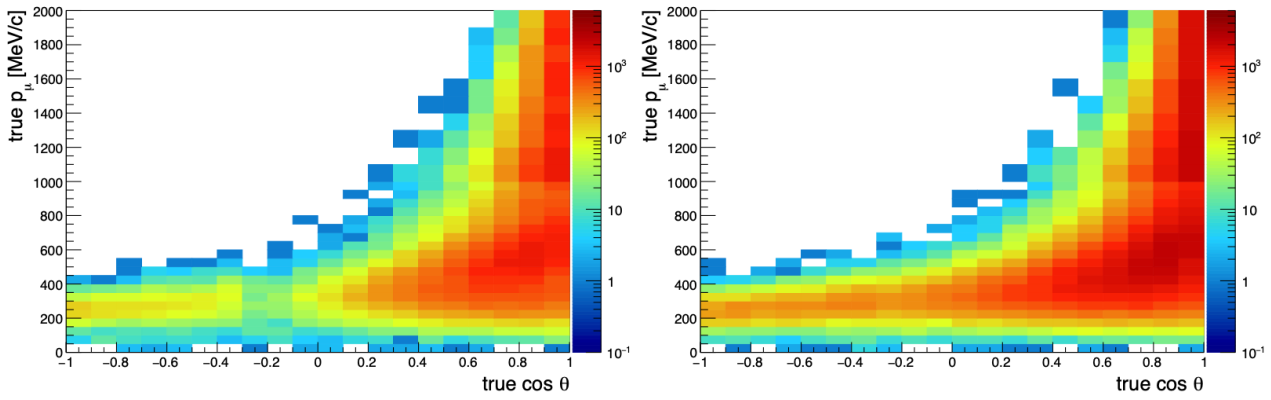

(a) Current ND280 **(b)** Upgraded ND280

Figure 3.5: Muon momentum and angle with the beam direction for selected ν_μ Charged-Current (CC) interactions in ND280 (left) and ND280 upgrade (right).

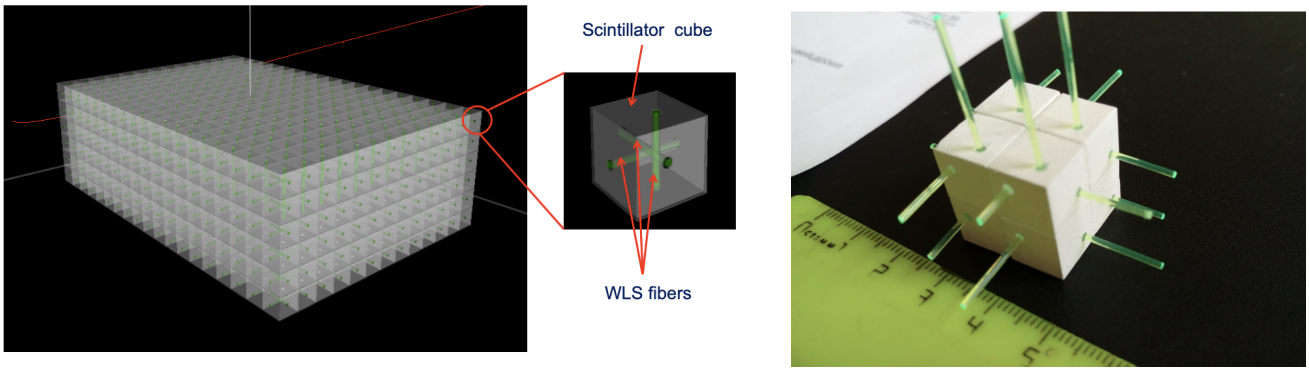

Figure 3.6: SFGD schematic; 192*56*184 cubes in (x,y,z) layers, each cube is 1×1×1 cm^3.

Table 3.1: SFGD scintillator cube parameters.

Parameter	value	comment
Count (Nx,Ny,Nz)	192,56,182	Carbon fiber box is being designed to reduce deformation
Dimensions (x,y,z) [mm]	10.27, 10.27, 10.27	
Reflective layer coating [mm]	0.1	cubes are optically isolated with chemical etching
Fiber hole radius [mm]	0.75	
Material	polystyrene doped with 1.5% of parater-phenyl (PTP) and 0.01% of POPOP	0.1 mm of optical coating is applied on all 6 surfaces
density [g/cm^3]	1.05	

3.3 SFGD vs FGD

There are 2 fine-grained detectors in ND280, FGD1 and FGD2. FGD1 consists of 30 layers of scintillator bars. Each layer has 192 bars perpendicular to beam direction, alternatively

Table 3.2: WLS fiber parameters.

Parameter	value	comment
Radius [mm]	0.5	Placed at the center of cube hole; Y-11 fiber
Material	Core: Polystyrene (PS), Middle clad: Polymethyl-methacry-late (PMMA), Outer clad: Fluorinated polymer (FP)	
Refractive Index	Core: 1.59, Middle clad: 1.49, Outer clad: 1.42	
Density (g/cm^3)	Core: 1.05, Middle clad: 1.19, Outer clad: 1.43	
Absorption wavelength [nm]	430 (peak)	
Emission wavelength [nm]	476 (peak)	
Trapping efficiency [%]	$\sim$5.4	
Attenuation length [m]	$>$3.5	

Table 3.3: SFGD MPPC parameters for model S13360-1325PE[25].

Parameter	value	comment
Effective photosensitive area [mm$\times$mm]	1.3$\times$1.3	Model S13360-1325PE
Pixel pitch [μm]	25	
Number of pixels	2668	
Fill factor [%]	47	
Package type	Surface mount	
Breakdown voltage [V_{BR}]	53$\pm$5	
Peak sensitivity wavelength [nm]	450	
Photo detection efficiency [%]	25	
Gain	7.0×10^5	
Dark count [kcps]	70	
Crosstalk probability [%]	1	

aligned in X and Y directions (horizontal and vertical directions) (Fig. 3.7). This gives FGD 2D readout in X and Y planes. Comparing FGD and SFGD selection efficiencies in Fig. 3.3, in forward direction ($\cos\theta$=1) FGD and SFGD both have good efficiency due to layer size being almost the same as cube size. But for tracks travelling to higher angle or backward direction, FGD's efficiency goes significantly down due to bar type readout and lack of segmenting in that direction. SFGD on the other hand has uniform granularity in all directions and gives better efficiency. In SFGD, 1 hit in scintillator cube give 3 readouts (XY, YZ, XZ fibers) and 3 hits corresponds to 3 cm. In FGD, 3 hits in at least two views means hits in 5 scintillator bars (5 cm). As shown in Fig. 3.8, SFGD will be able to reconstruct shorter tracks thereby improves reconstruction efficiency of low momentum pion and protons coming from neutrino interactions. The MPPCs for SFGD have higher pixel count (2668) compared to MPPCs used in FGDs ($\sim$ 800). It makes SFGD electronics more sensitive to the charge deposition and, will be able to better measure proton stopping point energy and understand neutrino vertex activity.

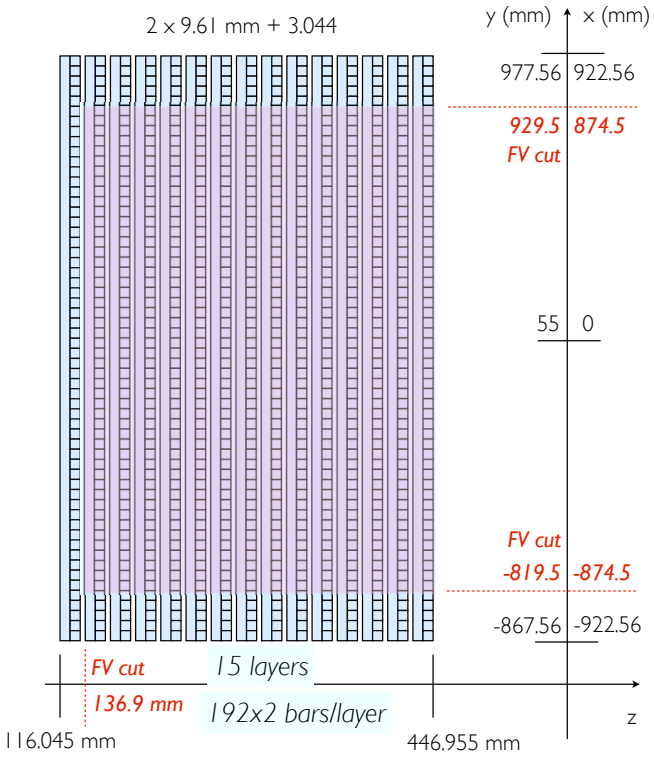

Figure 3.7: FGD schematic.

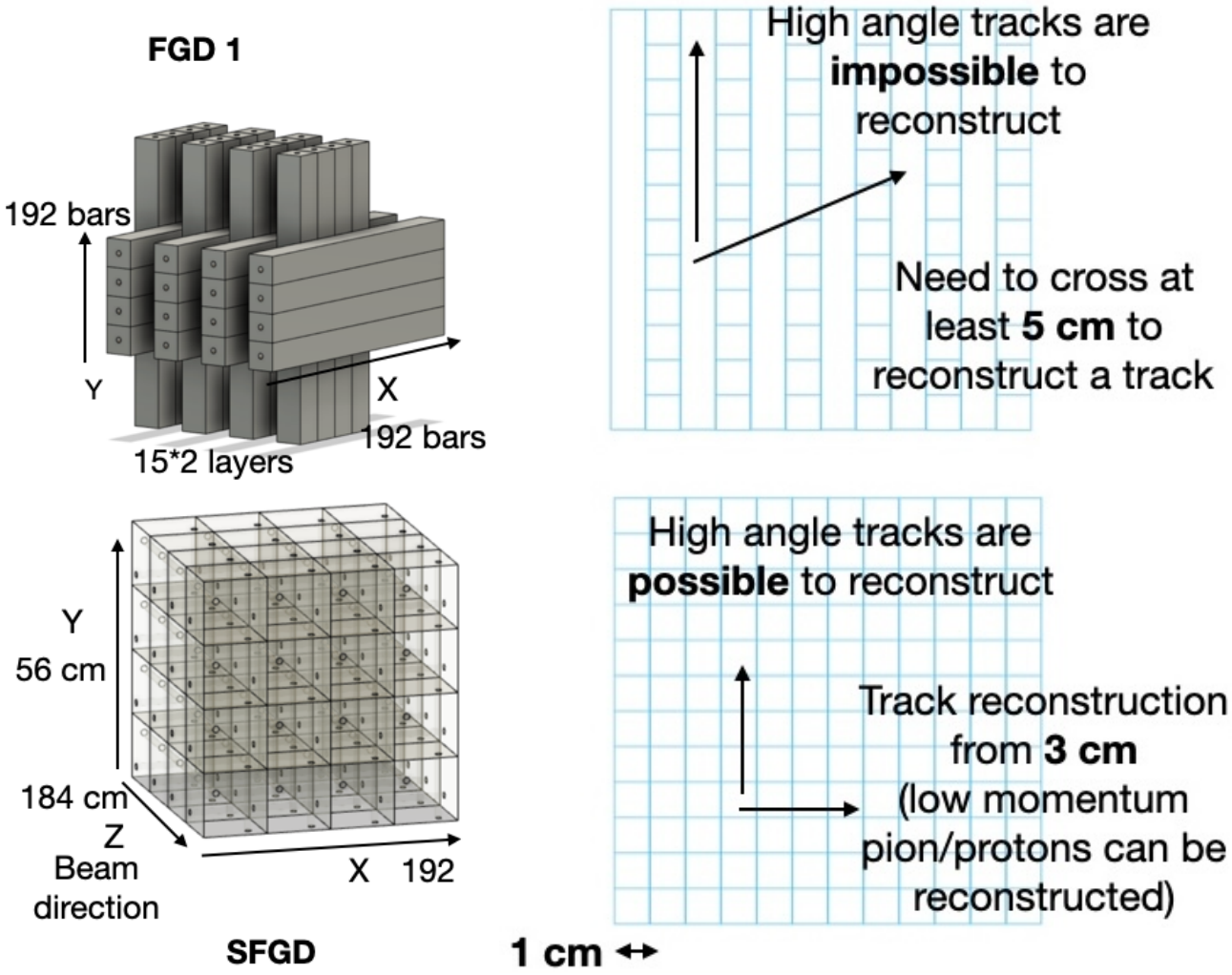

Figure 3.8: Comparison of FGD and SFGD geometry and track reconstruction capabilities.

Chapter 4

Development of SFGD electronics and quality testing

4.1 Overview

SFGD consists of over 56000 MPPC readout channels and new electronic boards called Front End Boards (FEB) were designed and developed to read signal data from the MPPCs. 64 MPPCs are mounted onto a "MPPC64" PCB (Fig. 4.1) connected to the Wavelength shifting fibers (WLS) passing through scintillator cubes. Flexible flat cable connect the MPPC64 to electronic crates (Fig. 4.2) mounted on to the side of SFGD. The major components of SFGD

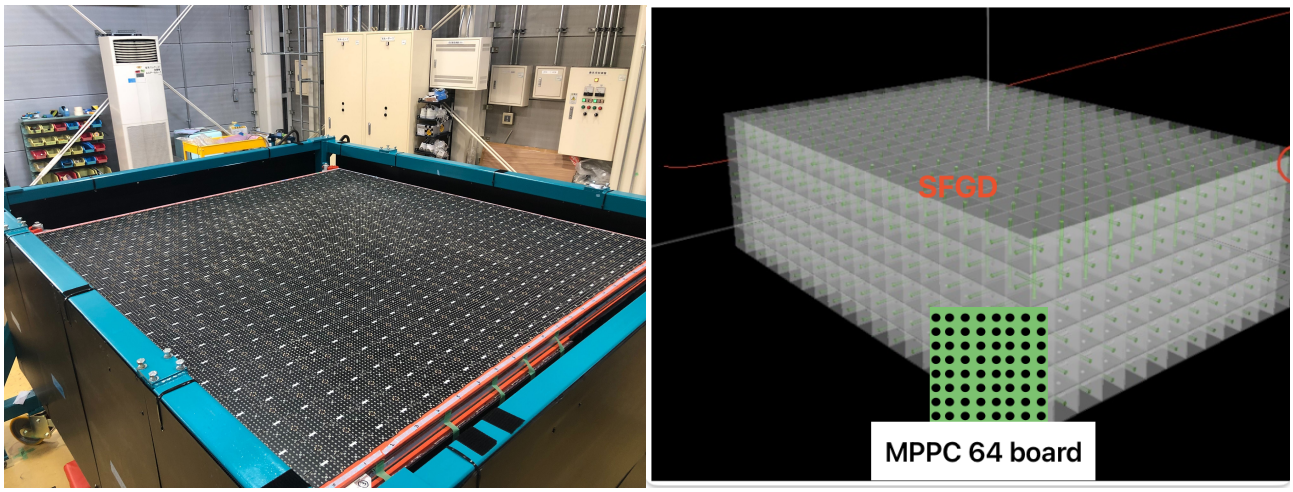

Figure 4.1: MPPC64 boards attached to SFGD. Right figure shows the top of SFGD covered with MPPC64 boards.

electronics are Front End Boards (FEB), Optical Concentrator Boards (OCB) and Master Clock Board (MCB). There are 16 crates for SFGD each containing 14 FEBs and one OCB and back plane to facilitate the communication between OCB and FEBs. MCB is unique to all the detectors present in ND280, the role of OCB is to communicate with MCB and control the FEBs in its crate. Figure 4.3 shows the flow of information across the T2K beam line, SFGD and PC. During the physics run all detectors receive their trigger and clock information from beam line via Master Clock Board.

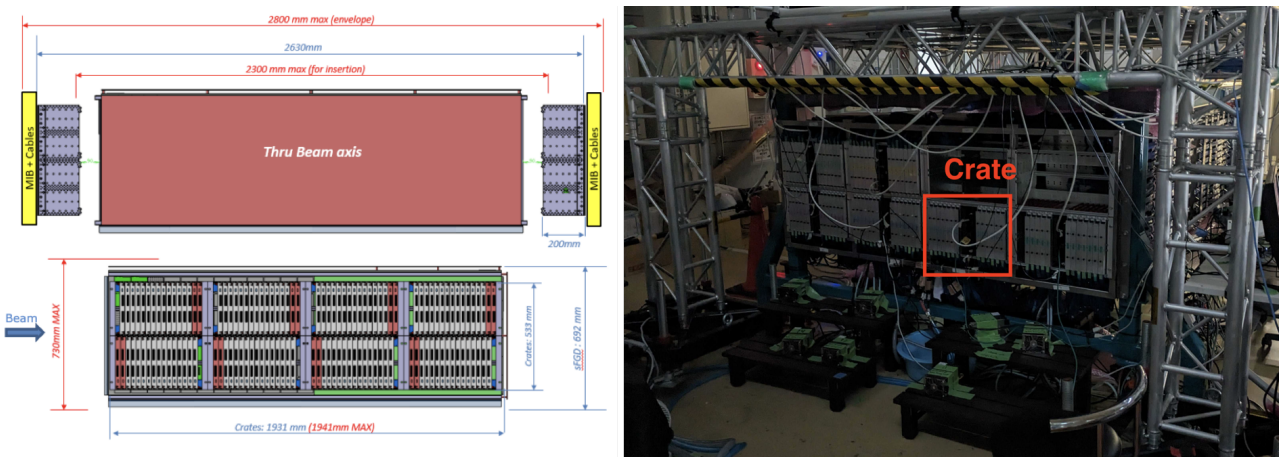

Figure 4.2: SFGD electronic crates are mounted on either side, each crate houses 14 readout boards.

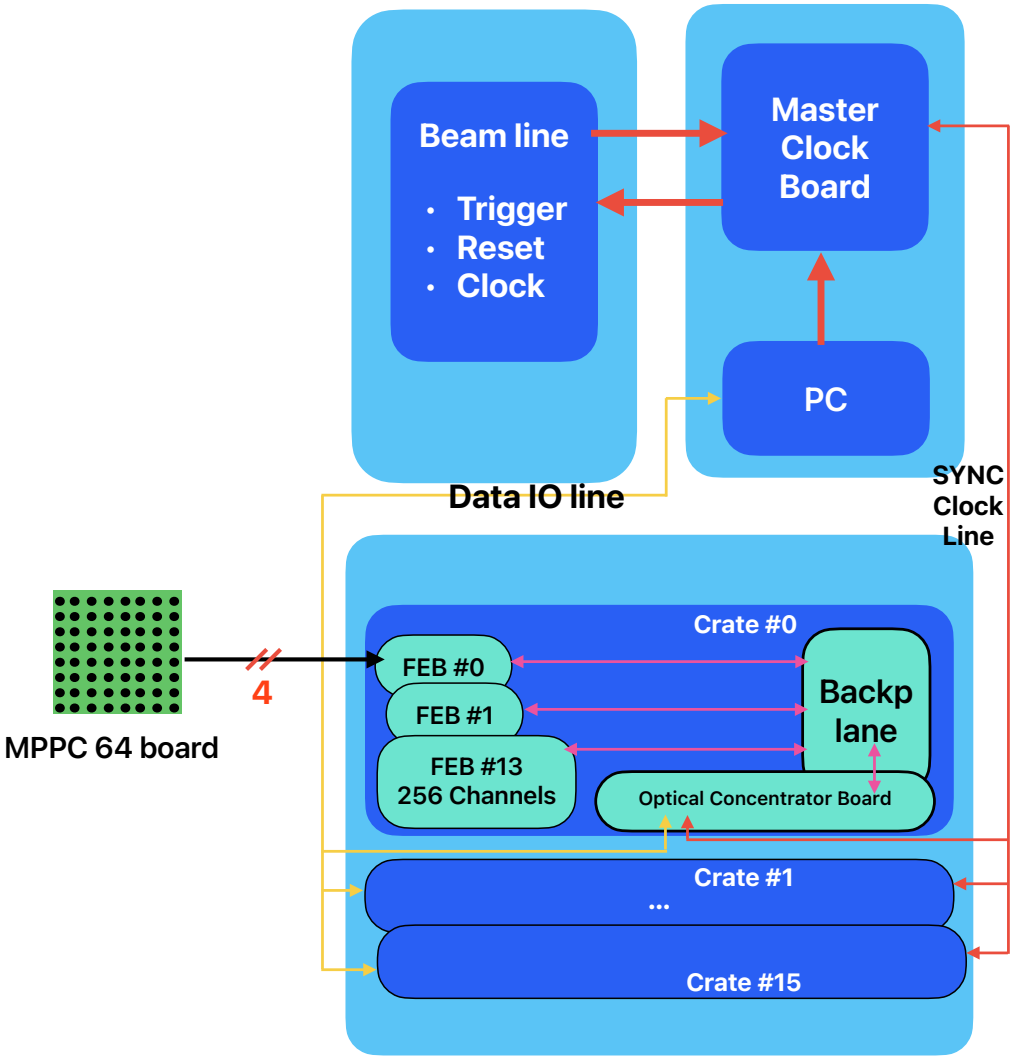

Figure 4.3: Overview of SFGD electronic system.

4.2 Front End Board

Each FEB (Fig. 4.4) is designed to readout 4 MPPC64 boards, 256 MPPCs, and in total SFGD utilizes 220 FEBs. FEB are equipped with 8 CITIROC1A (Fig. 4.5) chips, each of which processes 32 MPPC channel signals. The CITIROC chip has two main function: charge and time measurement. For charge readout, the information is propagated as voltage and digitalized using ADC (Analog to Digital Converter) as shown in Fig. 4.6. The charge input is divided into two lines with different gain (high gain and low gain) differ by a factor of 10. Two capacitors, fixed value one in series and variable one in parallel, are used to adjust the gain value. Time information is calculated based on how long the analog charge signal is above the threshold value. The CITIROC1A chip can trigger on individual channel or multiple along with gain values depending on user defined settings. A quality test of the manufactured FEBs is necessary before the FEBs are installed in the detector.

Figure 4.4: SFGD Front End Board(FEB).

4.3 Motivation

Test of FEB requires injection of test signal into each of 256 channels to check the output response. Using channel by channel injection from function generator takes almost 4 hours to test single FEB even for short 10 sec signal in each channel due to changing input channel after every time. In this way, we need 3-4 months to test all FEBs once. In addition, we may need to test some boards multiple times to fix problems. This will impact the schedule of the detector installation in 2023. Our goal is to speed up the testing process to test each board in 15-20 minutes. One way to reduce the testing time is by testing several channels of FEB at once. For this, I developed a new signal injection board that can multiply the function generator output signal and inject into several channels of FEB simultaneously.

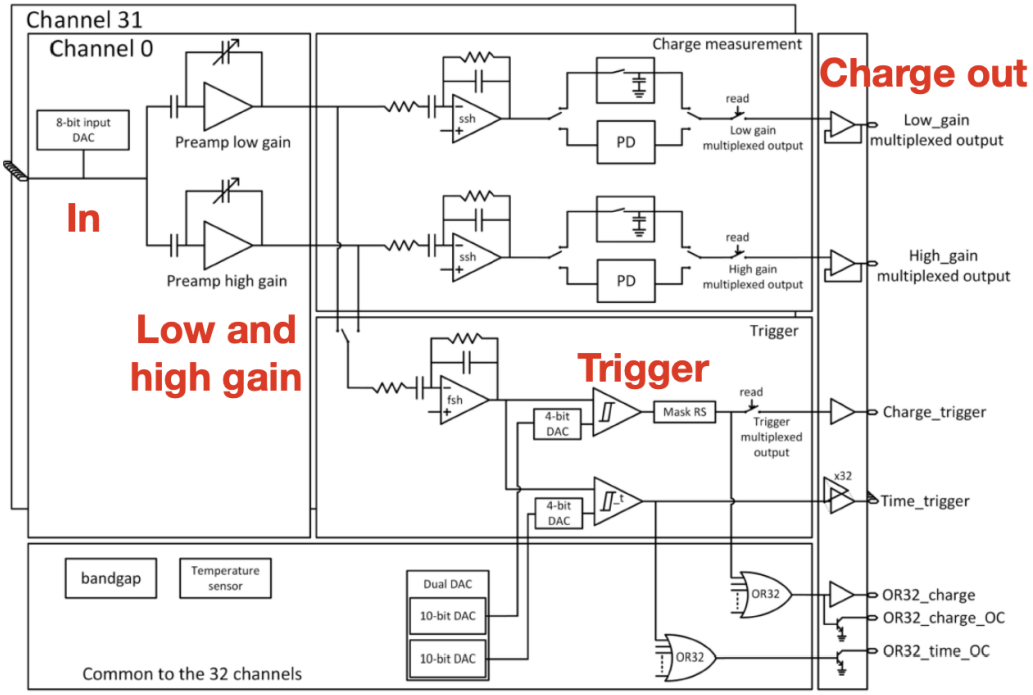

Figure 4.5: CITIROC1A chip used in FEB production[26].

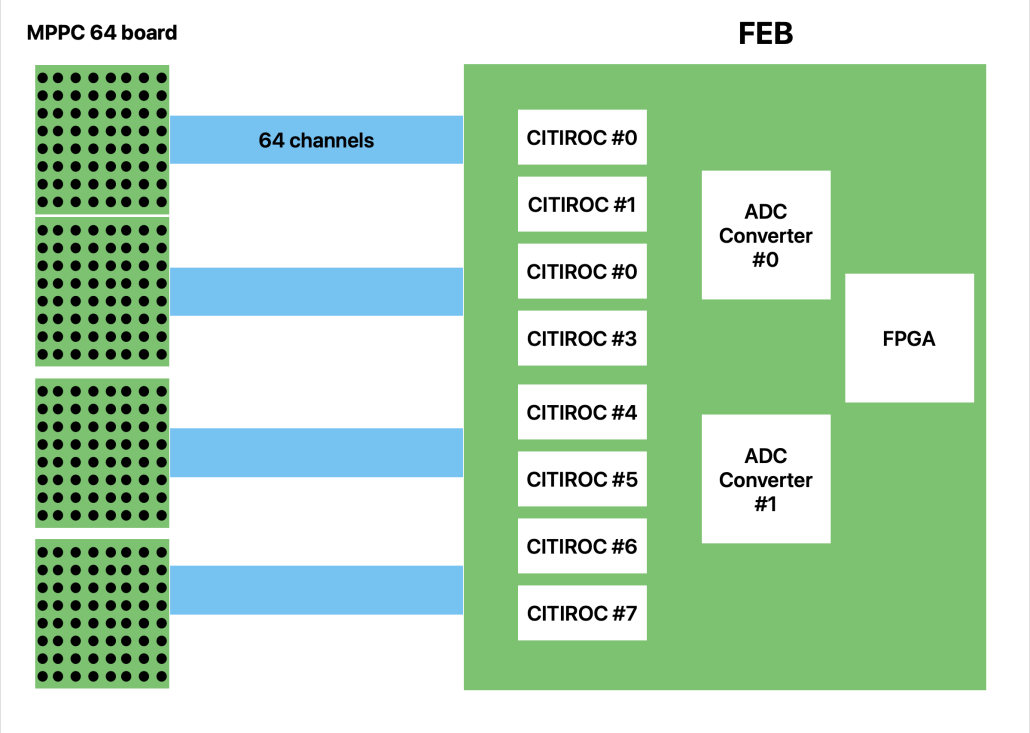

Figure 4.6: FEB to MPPC 64 boards connection.

4.4 FEB test bench plan

The requirement for quality testing of FEBs is that we should be able to perform tests on all readout channels of FEB and testing shouldn't take too long. Our earlier estimate was that we need to test up to 10 boards in a day. Once we receive the board from the manufacturing

company, preliminary tests are done. Preliminary tests include power cycling of the board and make sure all the major components of the board are receiving sufficient voltage and current. After that the firmware is installed onto the board which allows to control the board from graphical user interface. Once this is done board is then given to the test bench for more robust testing.

Our goal is to develop test bench that can test FEB efficiently. We made a new injection board(Kaladin) that can multiply and inject the test signal from function generator into all 256 channels of FEB to speed up the FEB testing process. Figure 4.7 shows the preliminary plan of using a PC to automate the operation of both function generator and Raspberry Pi(controls the Kaladin board) to inject test signal into FEB. The output from FEB is then analyzed to make sure the charge readout of each channel is within expectation for a given input along with several other parameters explained in section 4.5.

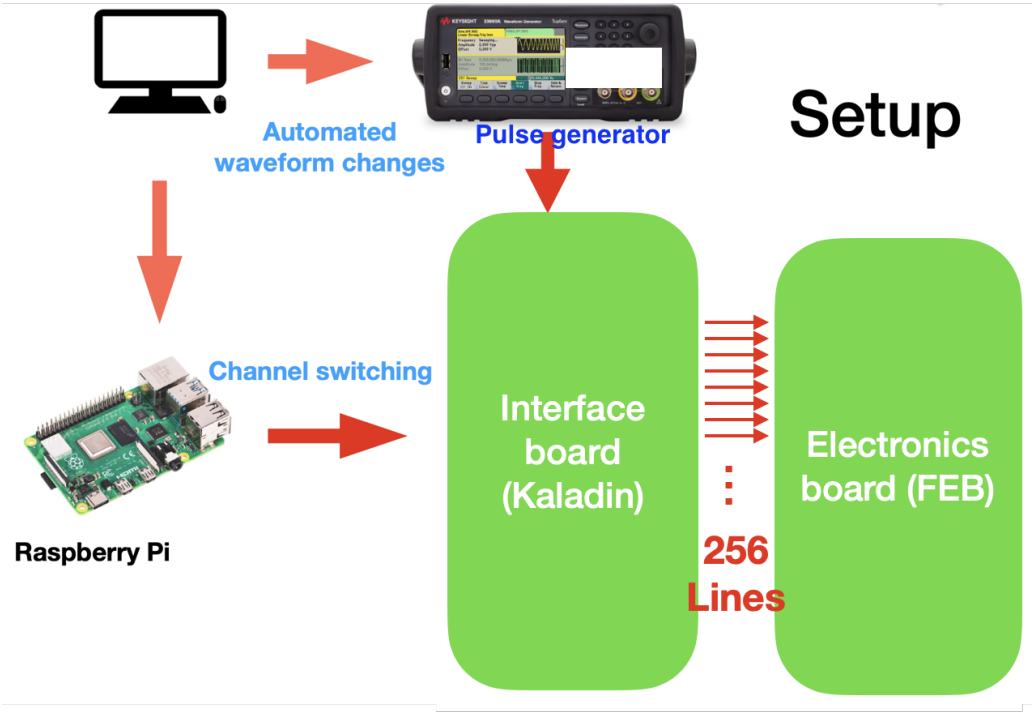

Figure 4.7: FEB test bench plan using an injection board(Kaladin).

4.5 Kaladin injection board

As a starting point, we had a discussion about the requirement for designing an injection board, named Kaladin, that can sufficiently multiply and drive 256 signal lines with up to 3V of input pulse. We first made a conceptual circuit as shown in Fig. 4.8. The input signal is fed into an Op-Amp as buffer and divided into 8 signals. Each of those lines is divided into 4 signals and fed into another Op-Amp. A multiplexer takes the output from each Op-Amp and the output from multiplexer can be selected from of the 8 output lines remotely using a 3 bit switching signal. We used a Raspberry Pi to inject the 3 bit signal and effectively controlling the active channels. We started designing the board using CADENCE simulation and designing software which is used to make complex electrical simulations and design circuit boards.

The work started with making simulations with various Op-Amps and multiplexers at required operating conditions of up to 3V input pulse and 10MHz frequency. After looking at the

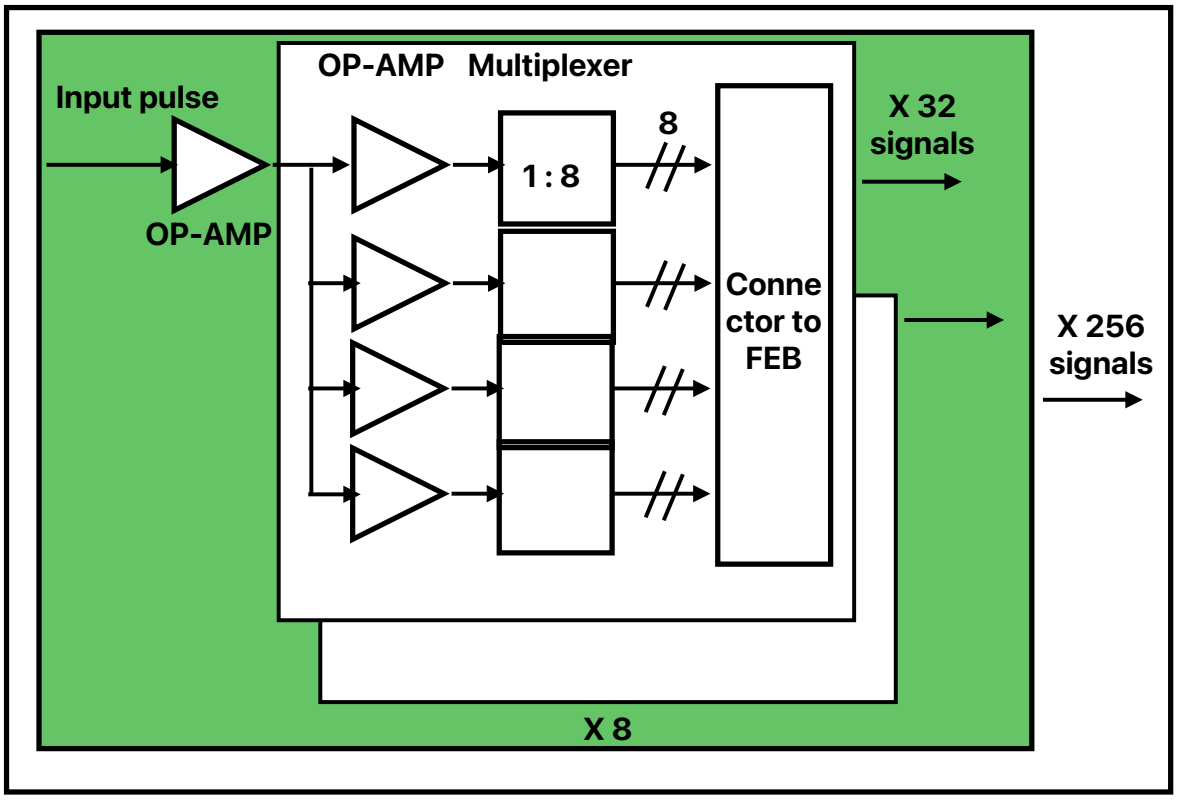

Figure 4.8: Kaladin overview: Utilizing Op-Amps and multiplexers the input pulse gets multiplied into 256 output signals.

results, we decided to use Op-Amp model OPA810 and multiplexer ADG1408(1:8). Figure 4.9a shows our first prototype of Kaladin board we ordered from a company based on our design. In the middle of the board are 8 connectors where a blue ribbon cables are attached, the other end goes to FEB input.

On our first prototype (Fig. 4.9a), we saw unexpected noise and after some investigation we realized that we need to add resistors and capacitors in series and parallel respectively to suppress the noise. A new board (Fig. 4.9b) is ordered with some modification(Fig. 4.10) and we observed the noise reduction as shown in Fig. 4.11. We added extra resistors in series and capacitors in parallel to Op-Amps to mitigate the noise.

4.5.1 Kaladin validation

We had to make sure Kaladin board is suitable for FEB testing, so we purchased a commercial readout electronics board, CAEN A1702[27] 32 channel readouts, which also utilizes CITIROC1A chip. We made the test bench using CAEN board(Fig. 4.13) and injected the Kaladin signal. Following tests are conducted on various aspects of Kaladin board such as output dependency on input signal frequency and amplitude.

Gain vs Frequency: Since Kaladin utilizes Op-Amps, we did a study to understand the output gain (output/input) of Kaladin as a function of input signal frequency. Figure 4.14 shows the decreasing gain curve with increase in frequency, this tendency matches with what is described in the data sheet of the Op-Amp model we used in Kaladin. Our requirement

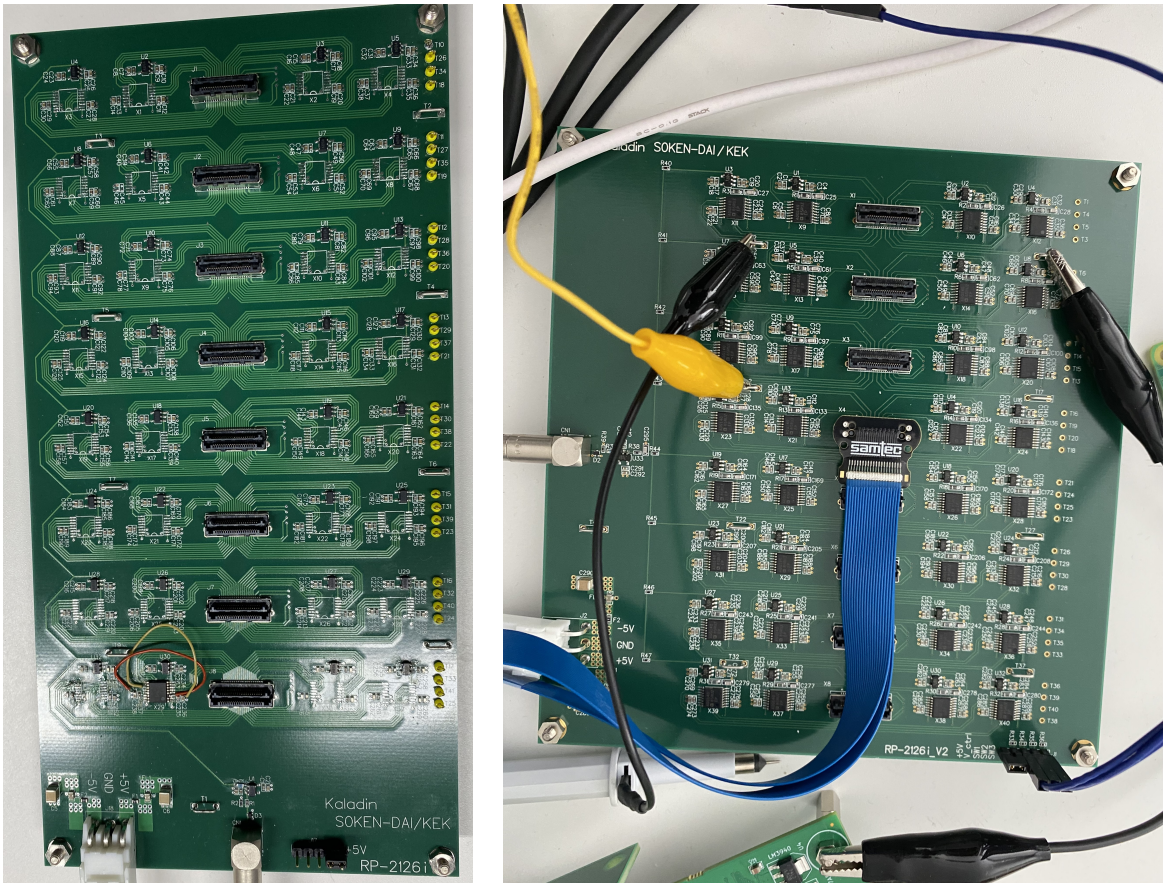

(a) Kaladin V1 (b) Kaladin V2

Figure 4.9: Kaladin boards designed for FEB testing.

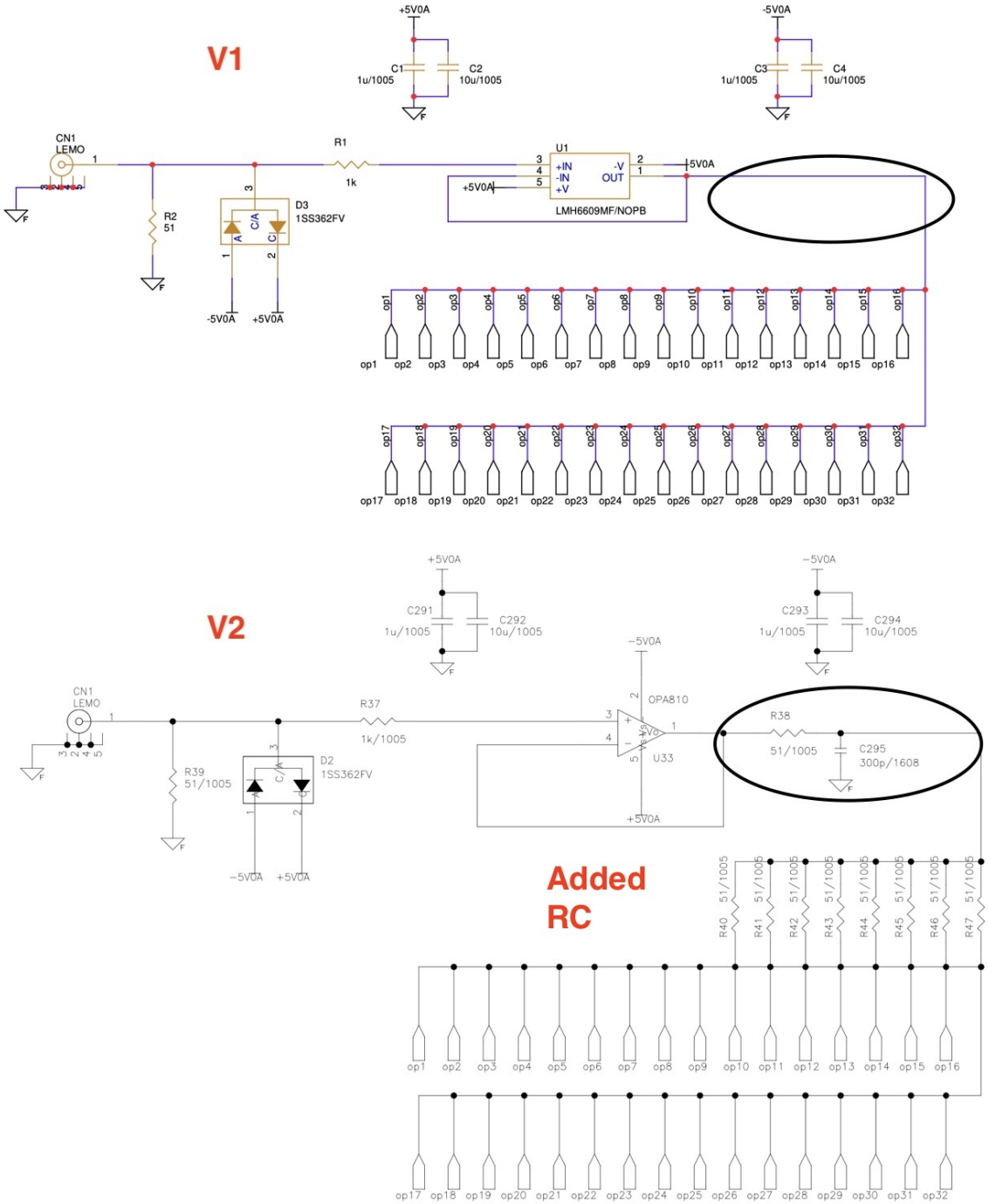

Figure 4.10: Changes made to the lines coming of Op-Amp from version 1 to 2. Added a resistor in series and capacitors in parallel to reduce the noise. Same for all Op-Amps on Kaladin.

for FEB testing signal is 100kHz frequency and using Kaladin board we can keep the gain of testing signal stable at this frequency.

ADC uniformity across multiple channels: Kaladin is not only meant to provide signal for several channels at a time, but we also expect the signal to remain same across all channels. Figure 4.15 shows the mean ADC distribution as a function of input signal amplitude. Figures 4.16 and 4.17 also show the deviation of mean is about 2% which is very stable for our purpose.

Crosstalk: Another aspect of multichannel signal injection is crosstalk in channels without

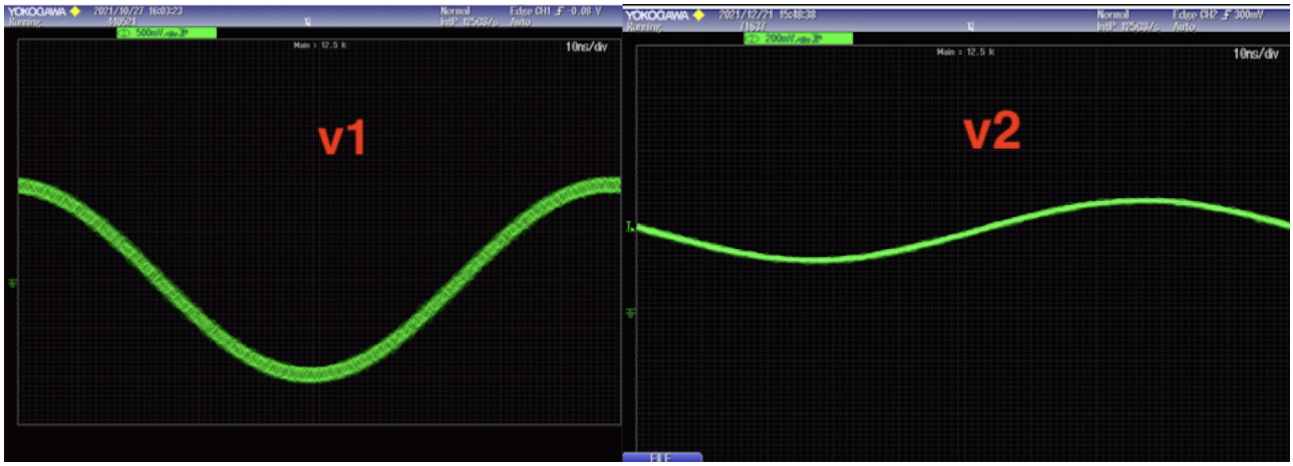

Figure 4.11: Kaladin output noise reduction from version 1 (left) to 2 (right).

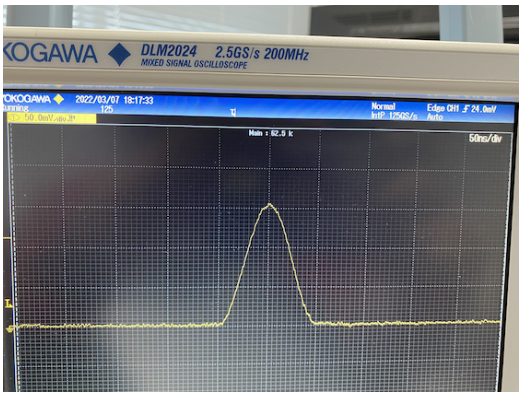

Figure 4.12: Input pulse from a function generator used for testing.

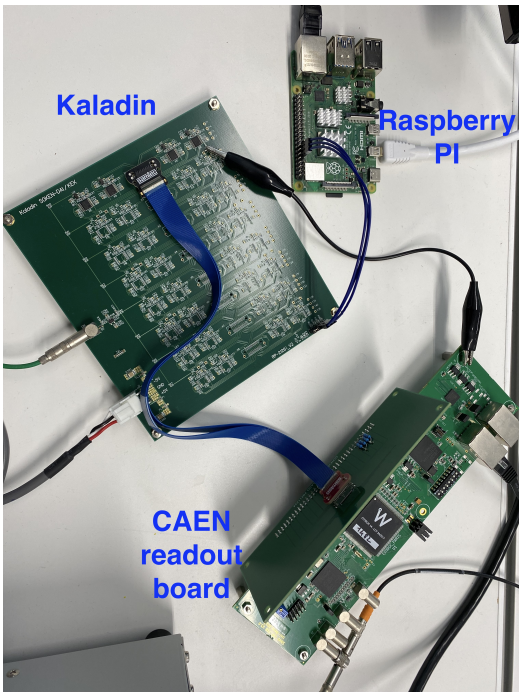

Figure 4.13: Kaladin testing setup using CAEN board.

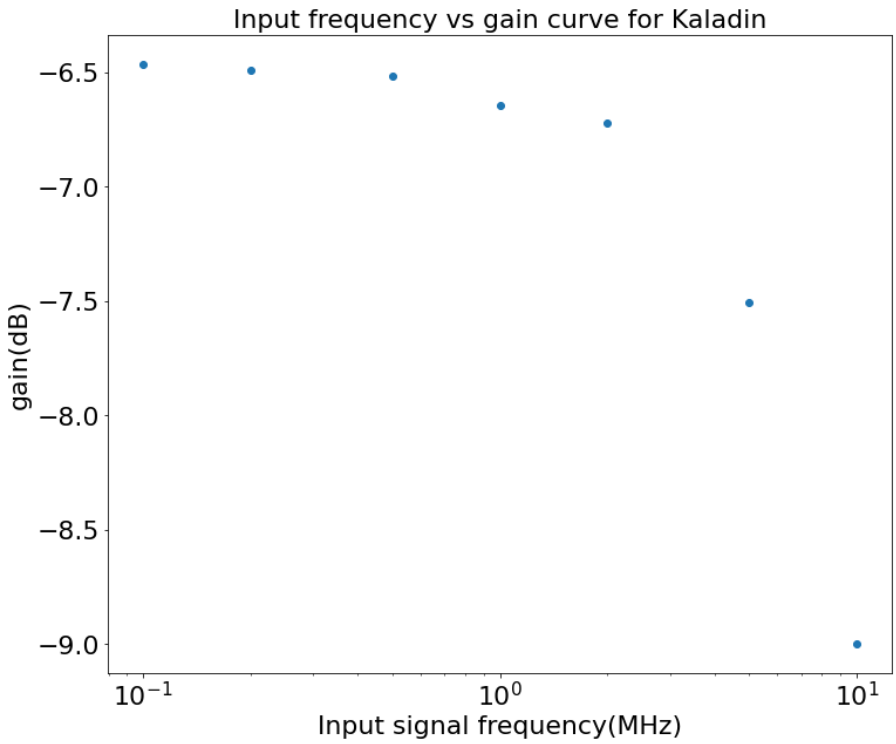

Figure 4.14: Output gain as a function of input frequency.

any signal injection. We ideally want less than 1% crosstalk between kaladin output channels when we eventually use it for FEB. For this we need to be able to see signal that is smaller by a factor of 100 in the crosstalk channels. We modified the gain of CAEN readout board so that the channels with input will have minimum gain(1) and channels to measure crosstalk with maximum gain(60). This allowed us to measure crosstalk. We also recorded channels with readout disabled to get the pedestal noise. As you can see in Fig. 4.18, the crosstalk is very close to the pedestal for low input signal and can only be distinguished as we increase the signal amplitude. The crosstalk is calculated by taking the pulse height ratio of crosstalk channel to active channel after subtracting pedestal value from both and after correcting CAEN readout gain. We saw the crosstalk to be about 0.06% and this value is negligible in terms of FEB testing.

4.5.2 Kaladin testing summary

Kaladin is able to inject signal into multiple channels with minimal deviation across the channels(4%) along with very low crosstalk(0.06%). The output signal is also stable up to 100kHz which allows us to test FEB with various input signals. Kaladin testing produced satisfactory results and is used in the FEB test bench explained in the next section.

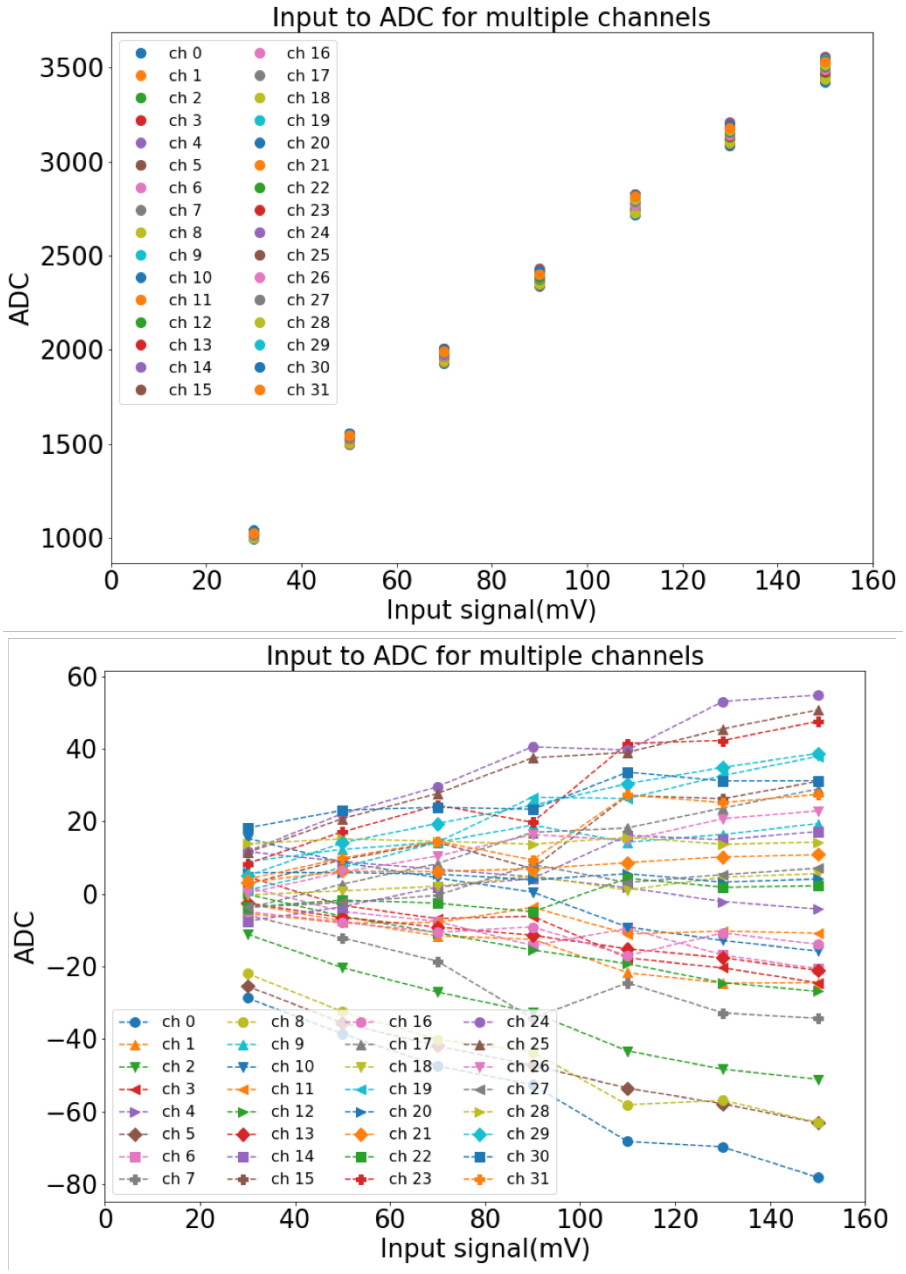

Figure 4.15: Output mean ADC (Top) and deviation with respect to other channels (Bottom) of kaladin board using a commercial readout board(CAEN) for 32 channels. Bottom plot is calculated by (signal - average of all 32 signals).

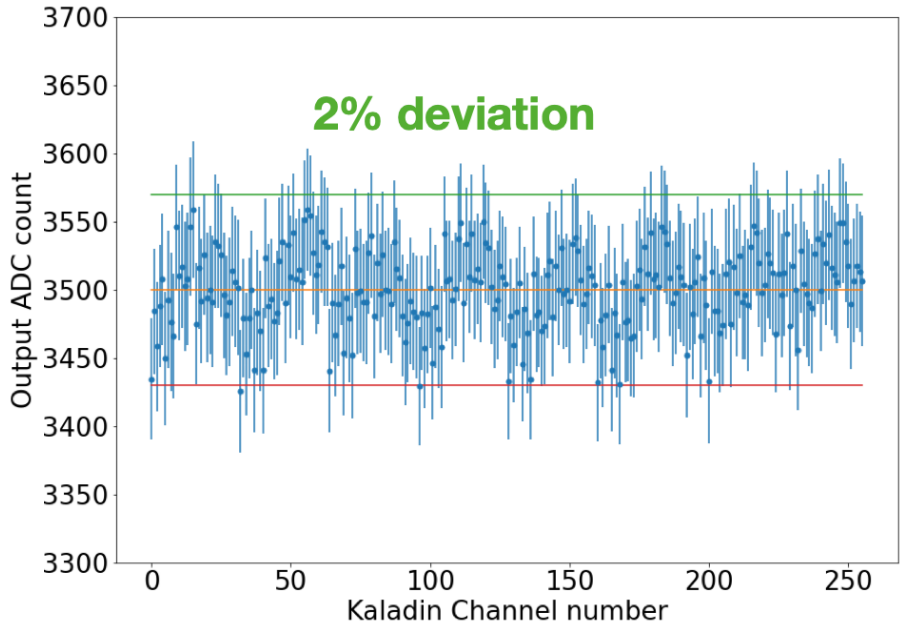

Figure 4.16: Kaladin channels output mean using CAEN board.

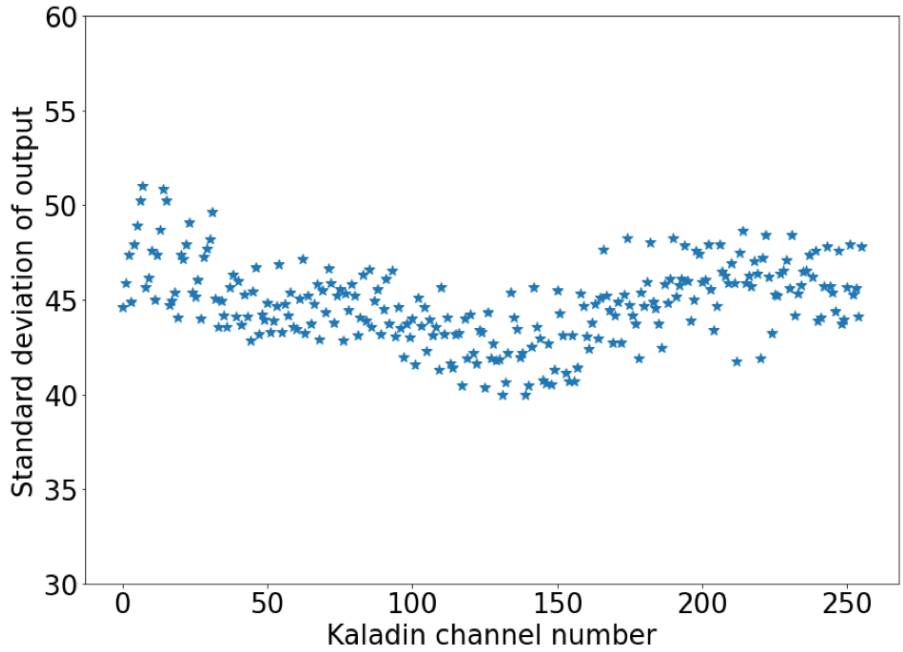

Figure 4.17: Kaladin channels output deviation using CAEN board.

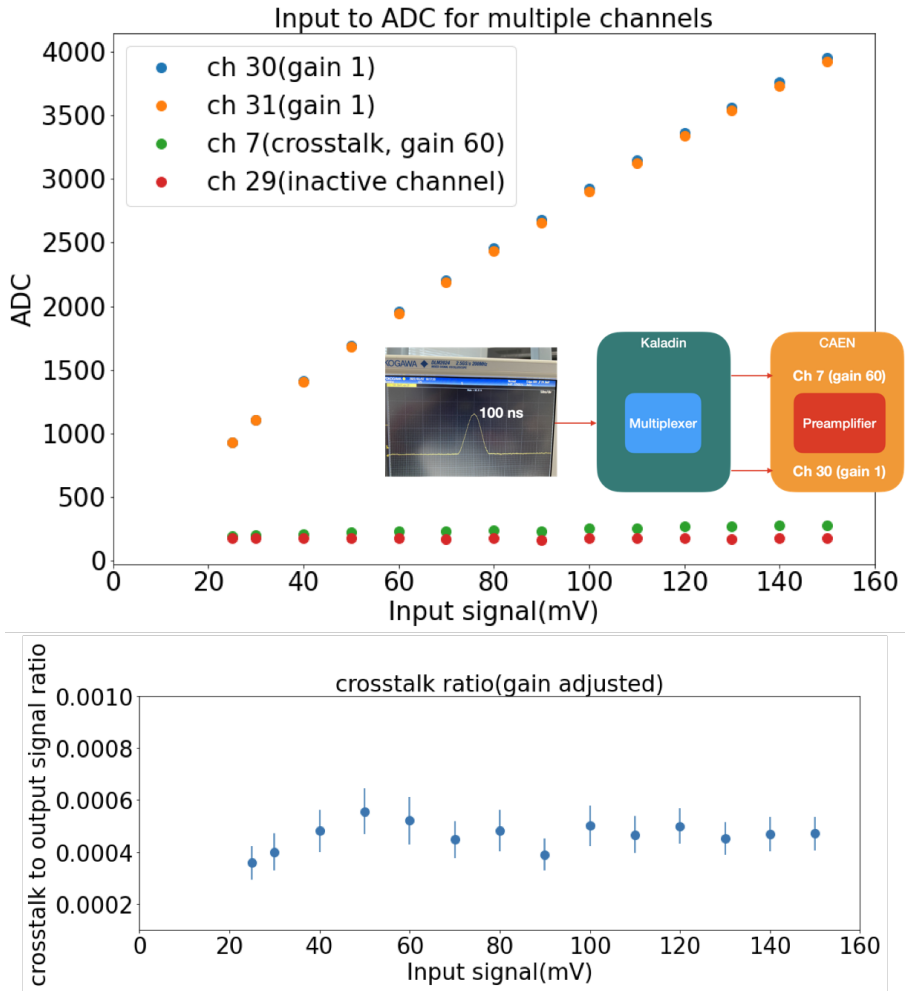

Figure 4.18: Crosstalk of Kaladin channels.

4.6 FEB quality test

Once we are satisfied with the Kaladin performance, we started making the preparations for test bench with FEB. The testing took place in University of Geneva and together with T2K colleagues at Uni Geneva. A mechanical jig(Fig. 4.19a) is made to hold the FEB, Kaladin and other necessary equipment for the quality test. The FEB is connected to Kaladin via MPPC Interface Board(MIB), blue ribbon carry the injection signal from Kaladin to FEB. Each cable corresponds to 32 channels. The mechanical jig allows us to quickly test FEB and replace with a new one without changing other parts of the setup.

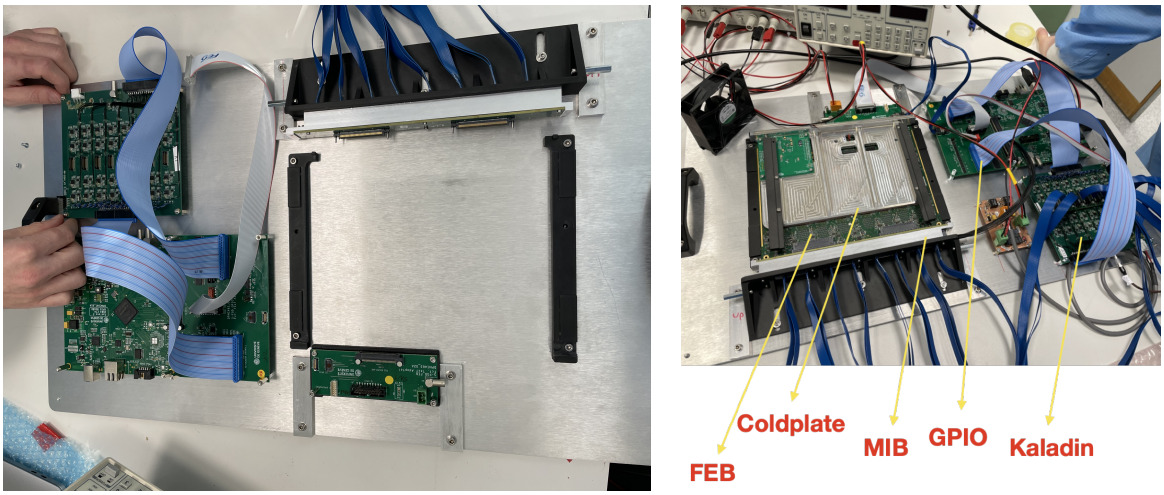

(a) FEB test bench jig.

(b) With FEB.

Figure 4.19: FEB test bench.

The FEBs are equipped with heat sink called "cold plate" to avoid over heating during their operation. A General Purpose Input Output (GPIO) board is used to control configuration, data taking and providing necessary input power of the FEB. GPIO, Kaladin and function generator are connected to one PC and this PC takes care of all the tests using automated scripts we prepared.

Steps for running this setup:

- Put FEB into jig and make sure the connectors are properly aligned with the pins.
- Turn on power supply for the jig(GPIO, Kaladin), function generator.
- Turn on FEB from PC user interface, communicates via GPIO.
- Run automated data taking scripts which performs various tests we prepared that will be explained later.
- Once that is finished a data analysis script is then initiated which judges if FEB passes the quality test or not.
- The result of tests is then displayed on the terminal with all the necessary files for debugging stored in a directory corresponding to given FEB.
- If a FEB does not pass all the tests then depending on the error encountered, further repairs are necessary.

The whole process is optimized over several days to make sure that the testing for each FEB takes around 15 minutes including the data analysis.

We had to test two main aspects of the FEB data taking:

- Stability of parameters such as on board voltage, current and temperature values of ASICs and FPGA.
- Uniformity of the ADC distribution for all channels and proportional change of ADC with baseline value changes.

Kaladin used to inject the pre-defined pulse from function generator into FEB to mimic the MPPC signal. The data scripts goes through various configurations to test following aspects of the FEB.

4.6.1 Channel short circuit test

This test ensures no two channels are shorted with each other, and this is verified by testing one channel at a time. The signal is injected into one channel at a time, and we expect the output in the same channel. Figure (4.20) shows each channel having expected number of events. If there is a short circuit or extra noise from channels we will see more entries in those channels. Figure (4.21) shows output for one channel where all entries are indeed in the correct channel, in case of noisy channels(ADC count<50) they will be recorded in red. The output lines have high gain and low gain lines that are separately analyzed for any problems.

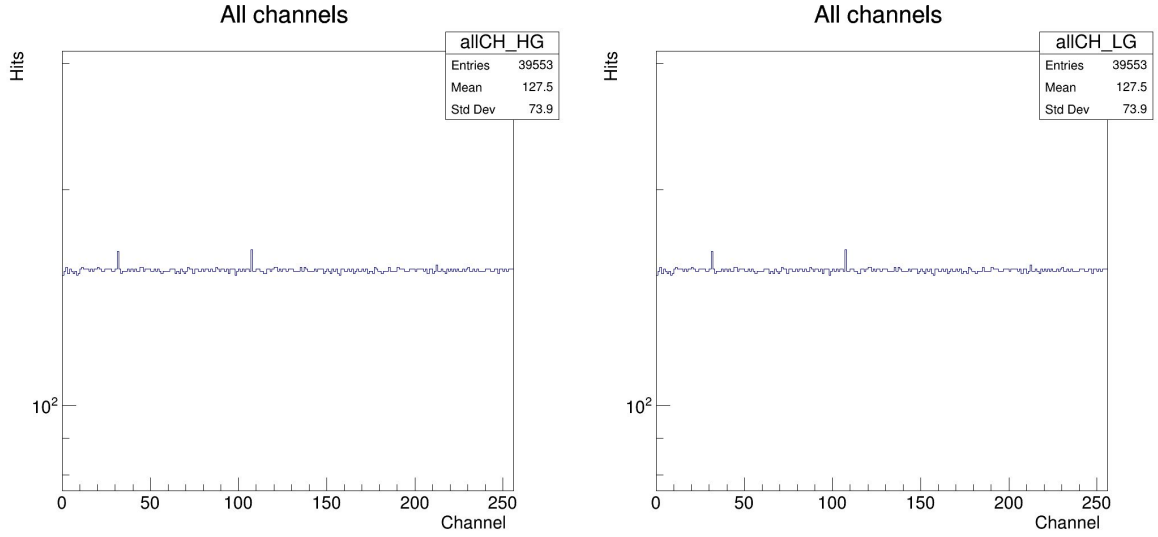

(a) High gain (b) Low gain

Figure 4.20: Open short test results for FEB 168, cumulative plot of Fig. 4.21 for all channels. Any extra noise/crosstalk will show up here. Small bumps seen in the plot are not big enough to be from noise.

4.6.2 Baseline test

CITIROC has capability to adjust input baseline voltage to ADC, which can control pedestal count. A test of this function is indeed performed to make sure the change in "baseline" value

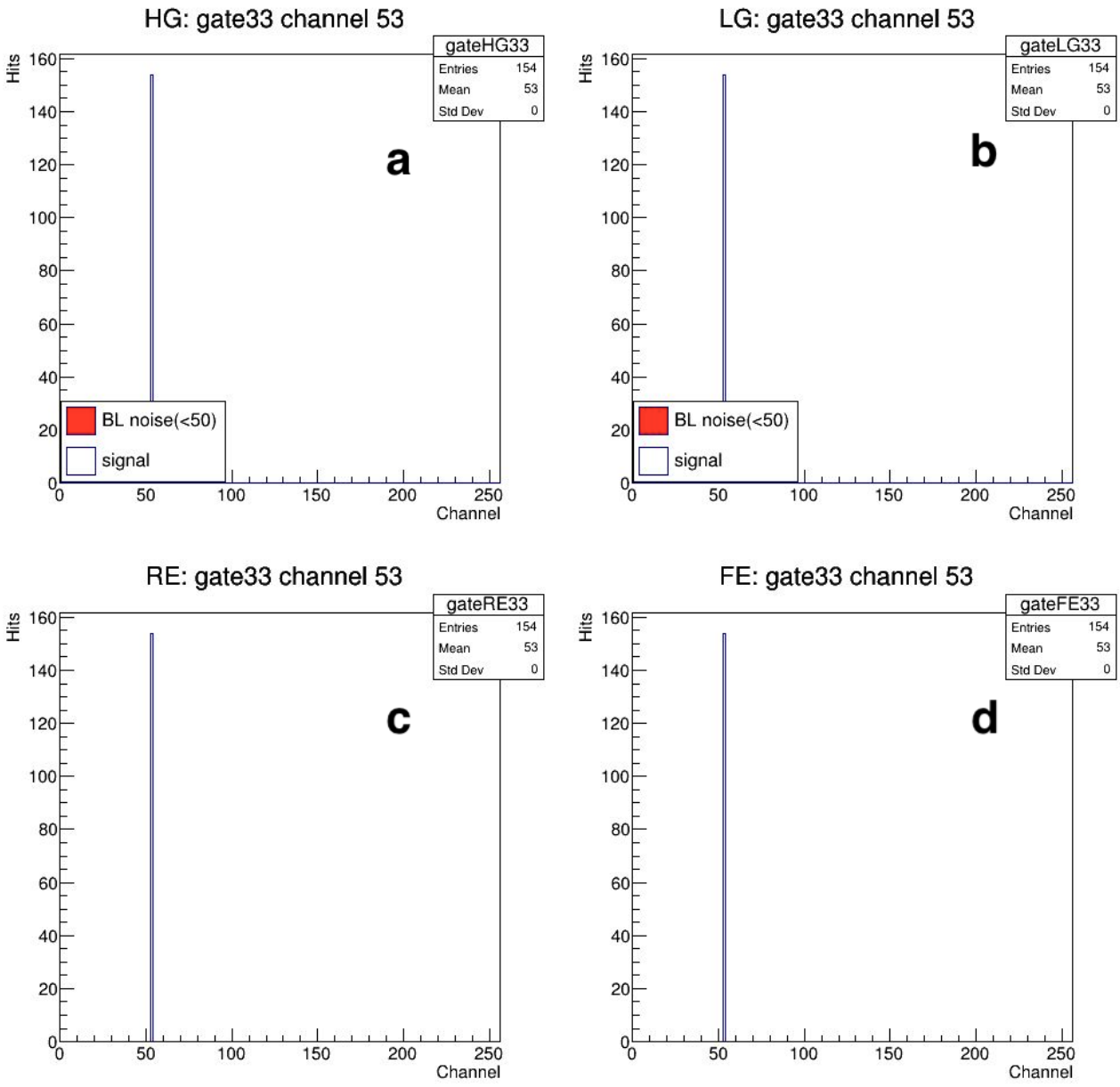

Figure 4.21: Open short test output of one channel of a FEB. The expected feature is all entries in the corresponding channel (53 here). (a) and (b) plots are entries high gain and low gain charge entries. (c) and (d) are rising edge and falling edge of time information.

is changing the observed output ADC count of pedestal. Baseline output voltage of to each CITIROC ASIC chip(8 in a FEB) can be adjusted from configuration side. This baseline value is useful to adjust the ADC count range to ADC full scale for a given gain setting. Figure (4.22) shows the proportional shift of mean ADC with baseline change. Figure (4.23) shows the change in ADC for each CITIROC when baseline values are shifted from 32000 to 50000, the change in pedestal mean is around 265 and as expected. If there is a problem in this baseline test we expect to see significant deviation from the expected ADC change.

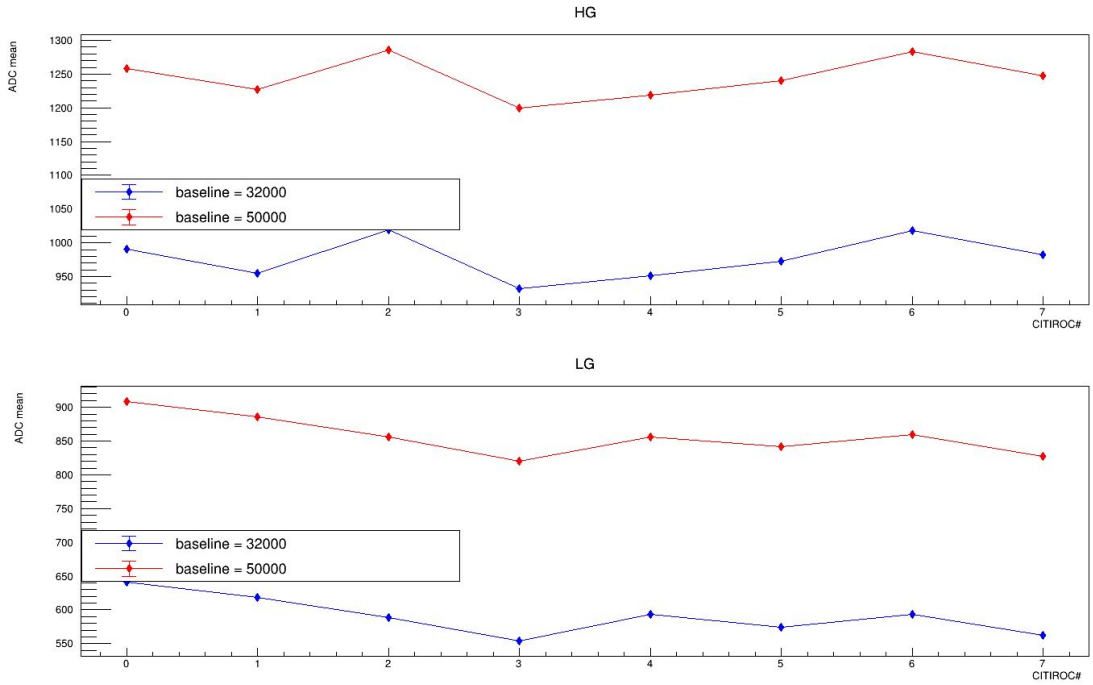

Figure 4.22: Baseline test for FEB 168 with High gain(top) and Low gain(bottom), the pedestal mean ADC count is expected to be shifted based on the baseline value in the configuration as shown in this plot.

4.6.3 Readout mean-sigma test

Best way to confirm the uniformity of the readout values across all channels of FEBs is by comparing their mean and sigma and making sure no channels are deviating too far from the expected values. Here as an example, ADC count distribution measured by one FEB channel is plotted(Fig. 4.24). In Fig.4.25 (a)(b), FEB output signal means for all 256 channels are plotted and RMS is plotted in Fig.4.25 (c)(d). Cuts are implemented to make sure the mean is in the expected range(between 850 and 1150 for HG, between 450 and 750 for LG) and RMS(less than 10 for HG and less than 8 for LG) of the distribution is not too wide. Number of events recorded too far from the mean value are also recorded as shown in Fig.4.25 (e)(f). No entries in this plot shows there are no problematic channels in the board.

4.6.4 Noise in FEB readout

Noisy channels are due to either crosstalk from other channels or from fault in the signal line. Both of these will manifest as more than expected entries in the readout and secondary peaks are seen in output signal distribution. In our test we inject around 150 pulses per channel. Any channel with abnormal entries are classified as noise channels. Figure 4.26 (a)(b) show the number of excess noise hits in the noisy channels in high gain and low gain, while (c)(d) show the mean of noise values. Note that noise can be seen in just one of HG and LG for a given channel. In this instance the problem is in the ASICs of the earlier prototype of the FEBs, and it is fixed before the final production. If we don't see any errors from the tests listed we can conclude that the FEB has passed the quality check. If there are any errors the debugging is done by looking at the plots stored after the data analysis. After this FEB may have to go through multiple runs on the test bench until all errors are rectified.

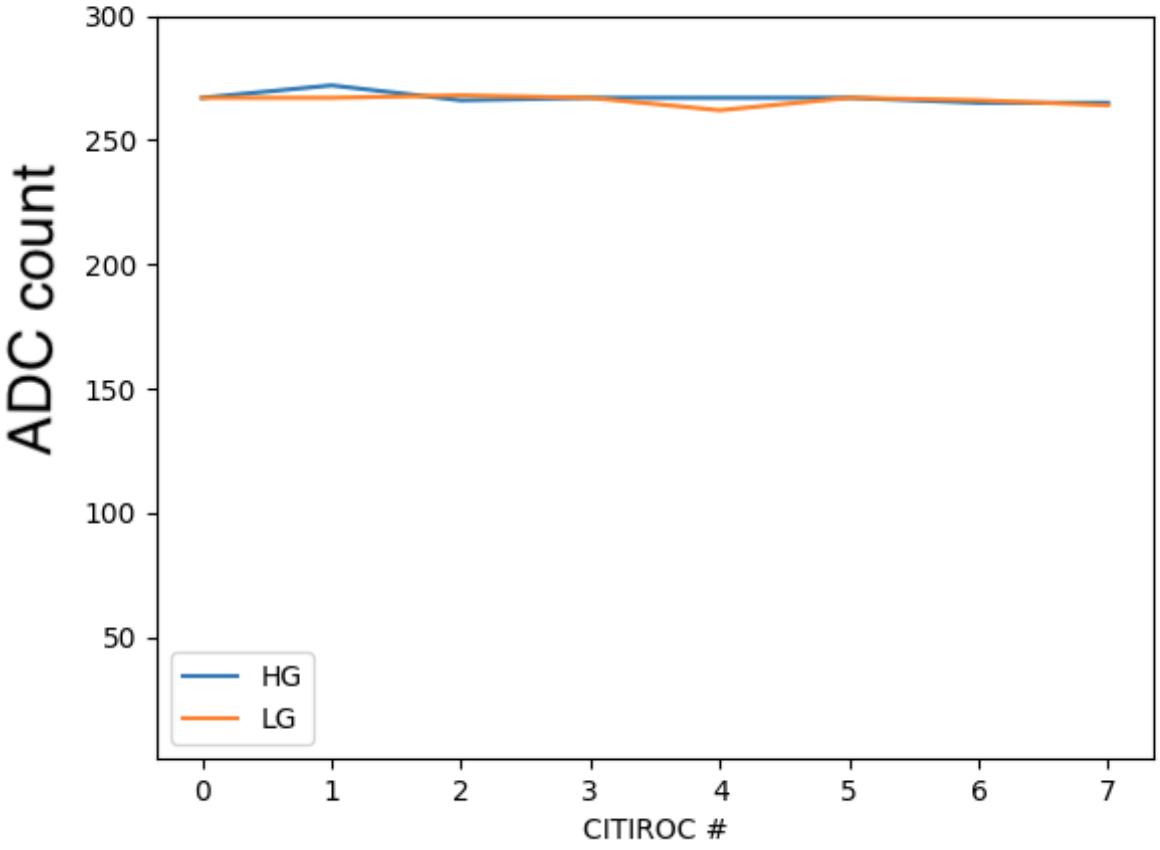

Figure 4.23: Pedestal mean change for each ASIC with baseline value change.

After we finalized tests needed, we made a second test bench using Kaladin and started testing the FEBs that being delivered from the manufacturing company. The schedule is about 30 boards delivered per week and so far we tested 180 boards. Out of them 100 passed without any issues and others are found to fail one or more of the tests on test bench. The engineers onsite are making necessary repairs to the boards. The test benches made with the Kaladin are crucial to test the boards in a timely manner.

4.6.5 QC summary

The test bench for the quality check is developed successfully and is used to test FEBs. In total 243 FEBs (including spares) are tested and 177 of them are delivered to JPARC to be installed in SFGD. The status of FEBs as of now is summarized in Table. 4.1, among the remaining FEBs 10 need repairs at the assembly plant and 25 are undergoing debugging for various issues seen during QC test (Table. 4.2). After debugging, all the FEBs will be delivered to JPARC. Regarding the development of FEB test bench, we were able to optimize the testing time FEB down to ∼12 minutes which is better than our initial expectation of 20 minutes. This test bench using Kaladin enabled us to test FEBs in time for SFGD installation.

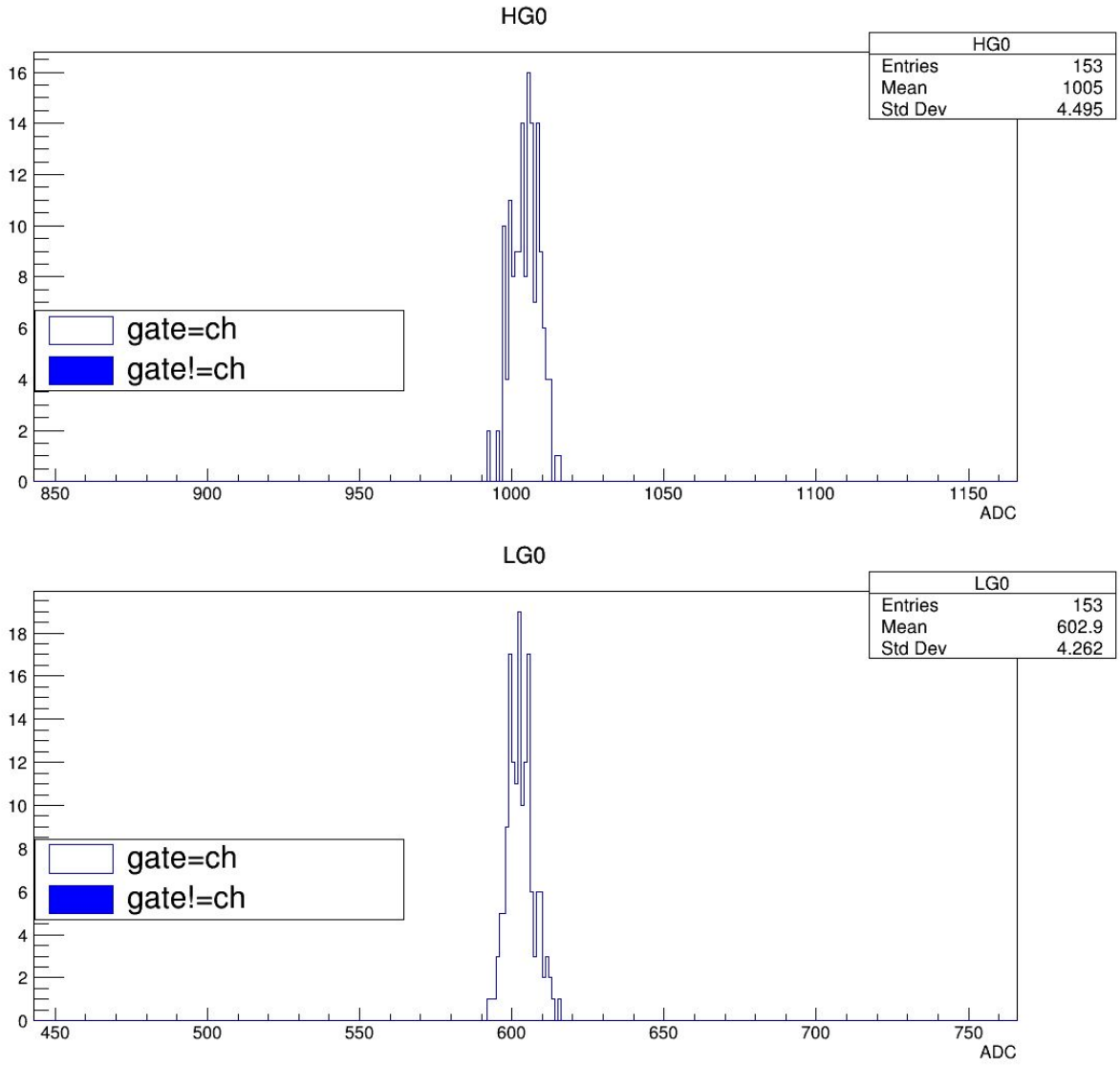

Figure 4.24: Pulse height distribution of one FEB channel using Kaladin.Top: High gain, Bottom: low gain.

Table 4.1: FEB status.

Location	Quantity	Comments
Delivered to J-PARC	177	
At University of Penn	15	To be delivered to Japan
LLR	1	Kept for measurements
Assembly plant repair	10	Repairing
VST and testing @ UniGe	15	Kept for other tests
Debugging @ UniGe	25	Check table. 4.2
Total	243	All went through test bench at least once.

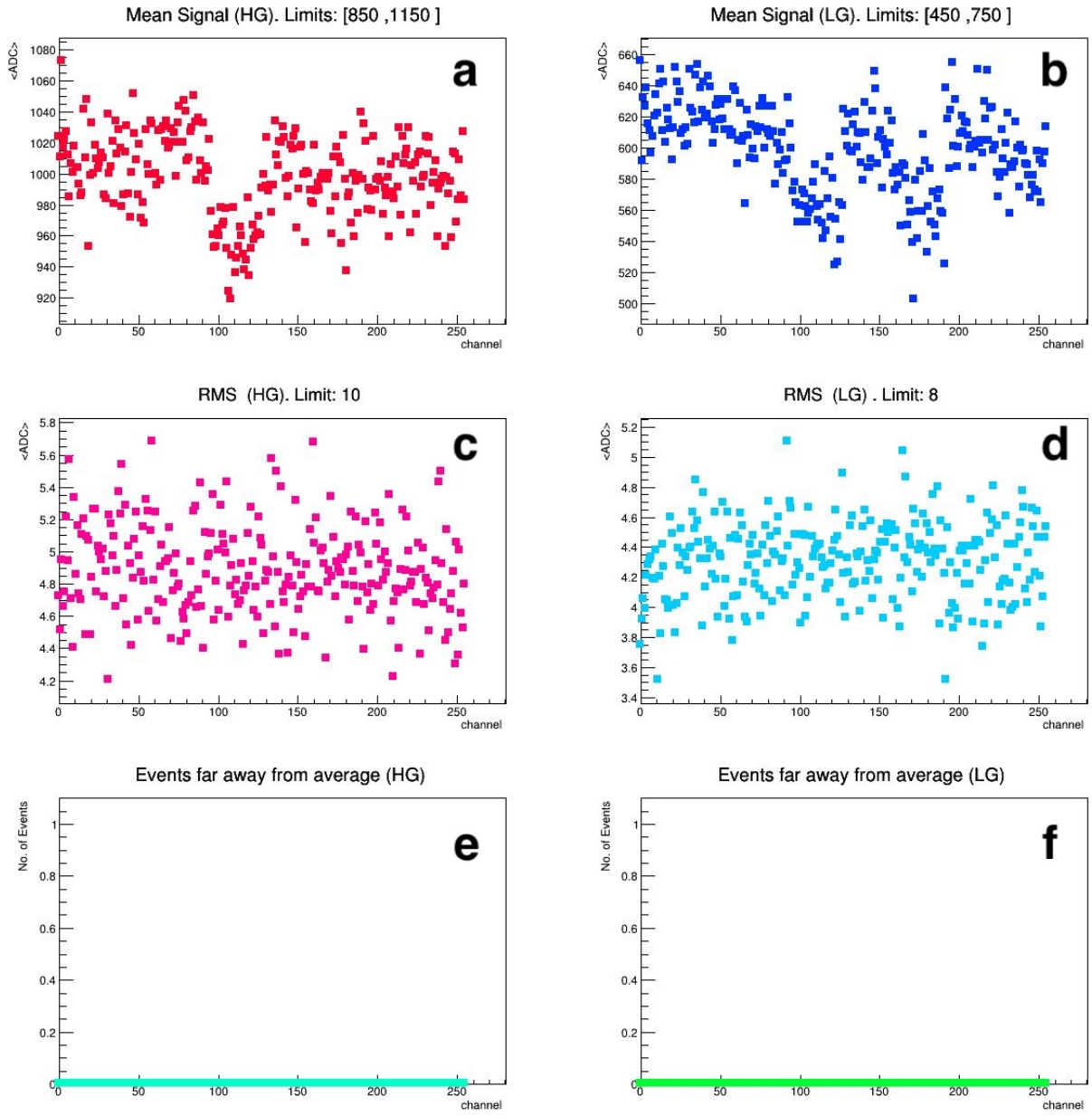

Figure 4.25: Mean(top), RMS(middle) of the ADC distribution and events too far from the average ADC(bottom) for FEB 168 for High Gain(left) and Low Gain(right). Bottom two plots show any channels with abnormal ADC count mean which lies outside our expected range for high gain and low gain values.

Table 4.2: Remaining FEBs undergoing debugging at University of Geneva.

Status	Quantity
Housekeeping noise	10
No housekeeping	2
Supervisor chips	2
Ch./Asic noise	11

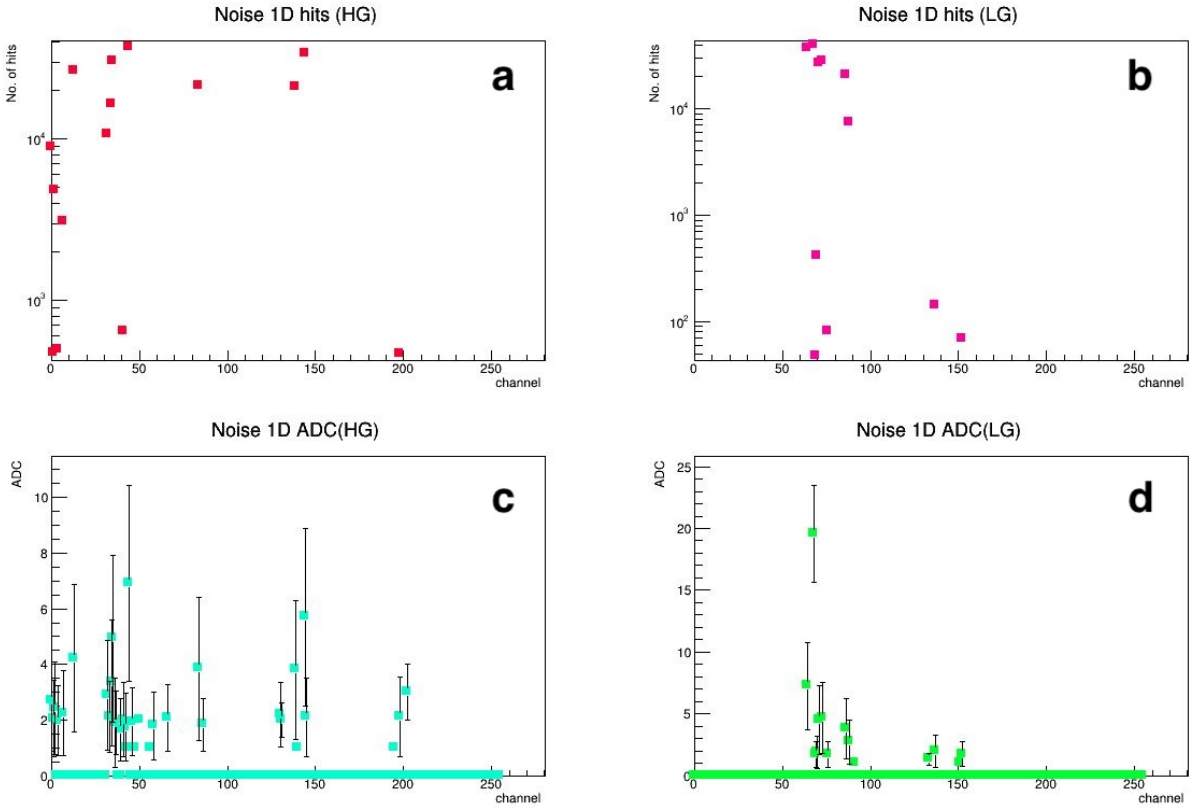

Figure 4.26: Noise in each channel from a FEB test with Kaladin.

4.7 Vertical slice test

The electronics for SFGD are newly designed and manufactured for installing in the new detector. Each component(FEB, OCB, MCB and back plane of the crate) is developed and tested individually similar to how we made a test bench for FEB. But to make sure all the components indeed work well together, we made a small scale test of the SFGD electronics with all the components involved before ordering full production of FEB. The test is called Vertical Slice Test(VST) and done with a small batch of FEBs(18). Further production of FEBs(220 total) was on hold until we give green light from this test in case we find major issues that were not seen in the test bench.

The reason for such a test on top of QC is because in the test bench we are using one FEB at a time and in VST we used multiple FEB(Fig. 4.28) at a time in the crate. The expected results from this test are:

- Being able to communicate from MCB through back plane to OCB to FEBs.
- MCB provides clock, triggers and data taking gate windows.
- OCB enables, configures and communicates with FEBs via back plane.
- FEBs are able to communicate with OCB and successfully take data with signal injected from Kaladin.

During the VST various issues were found and fixed as follows:

- Sync line are shorted on the back plane
- MCB clock signal is out of sync when there are multiple FEBs in the crate.
- OCB cannot differentiate between FEBs when there are more than one FEB in the crate - Fixed with making necessary changes in the FEB firmware.
- FEBs saw multiple peaks(separated by about 2048) in the output when only one is expected(Fig. 4.29) - Firmware issue with multiple FEBs taking data a time.

Once the issues are fixed, we are satisfied that FEBs satisfy the quality to be used in the electronics. The green light for full production is given and the newly delivered boards are tested on the test bench explained in the previous section.

4.8 Discussion

The Front End Boards are newly designed for the new SFGD to accommodate the large number of MPPC readout channels and high data rate. FEBs allows us to probe the short range tracks in SFGD with precise energy deposition and time information from the charged tracks. The FEBs will further play crucial role in reconstructing neutrino interaction vertex with finer position value. This improves neutrino interaction mode identification which in turn improves neutrino interaction cross-section measurements.

Quality test ensured we identified any potential problems which could potentially decrease the detector efficiency by either having dead or noisy channels. As of now the goal is to finish the QC of all FEBs as they are delivered then ship them to Japan for installation at the experimental site. We were able to take cosmic data and neutrino beam data in November 2023 (Fig 4.30).

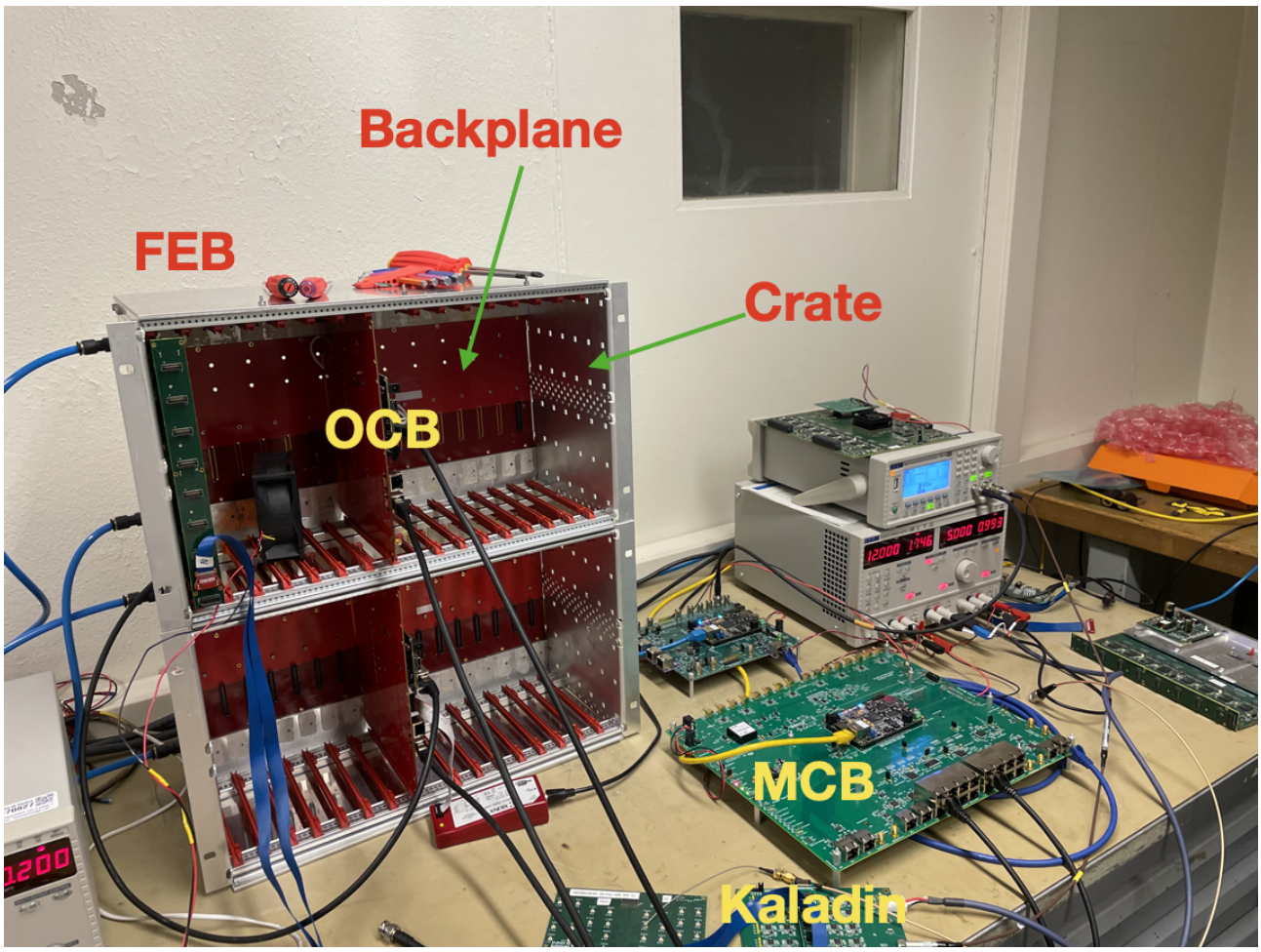

Figure 4.27: Vertical Slice Test(VST) setup.

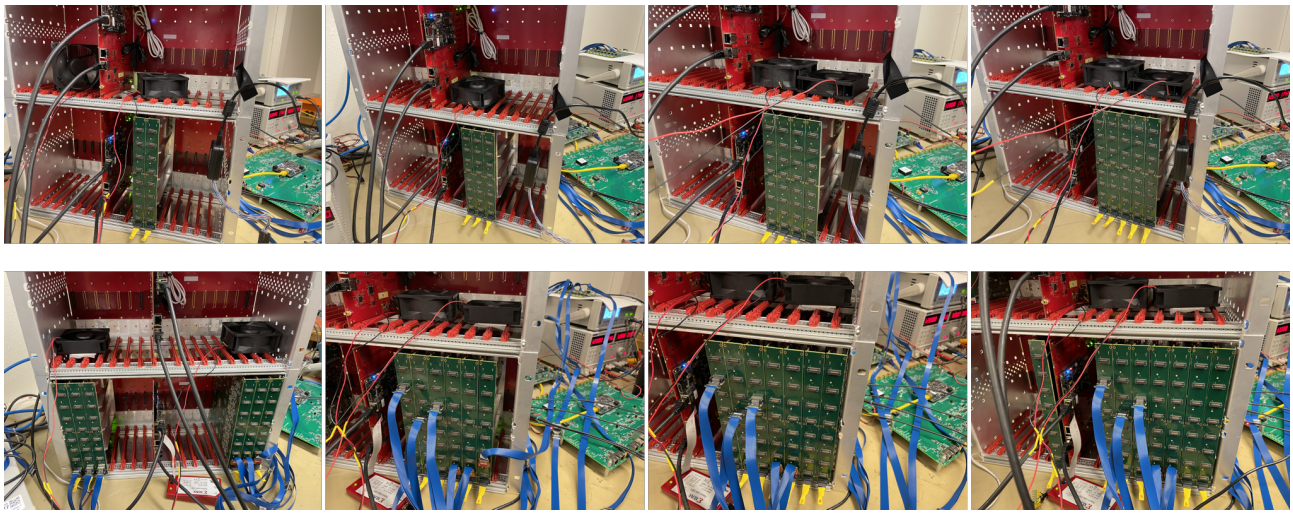

Figure 4.28: Multiple FEBs tested in VST.

4.9 Summary

The FEBs are newly developed and needed to be tested before installing in SFGD. Since we need to test 220 FEBs and each contain 256 readout channels, a test bench had to be

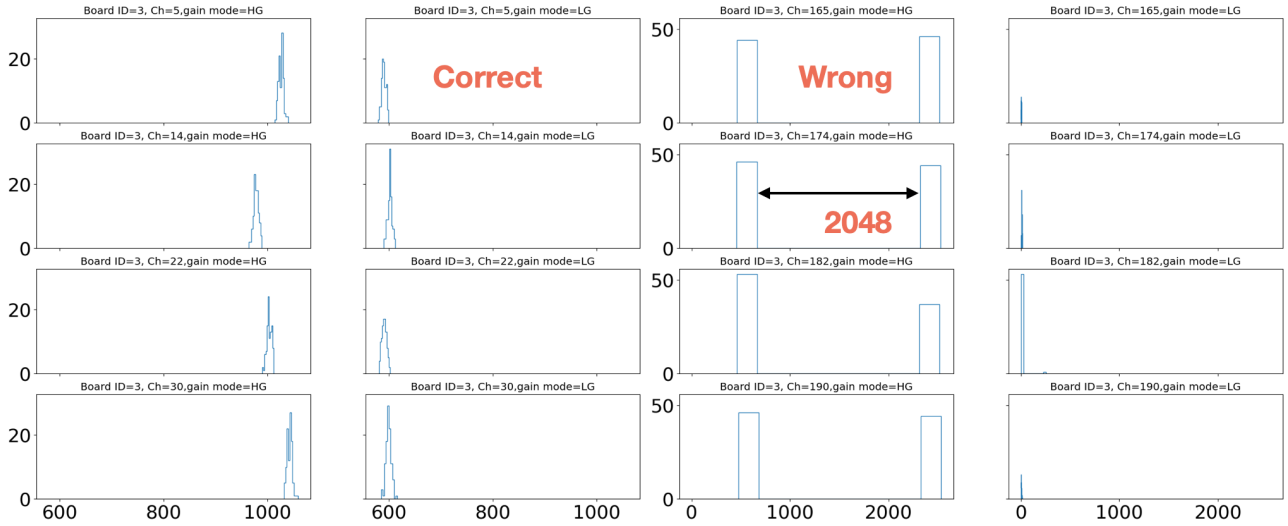

Figure 4.29: Some FEBs recorded multiple ADC peak instead of one due to a firmware issue.

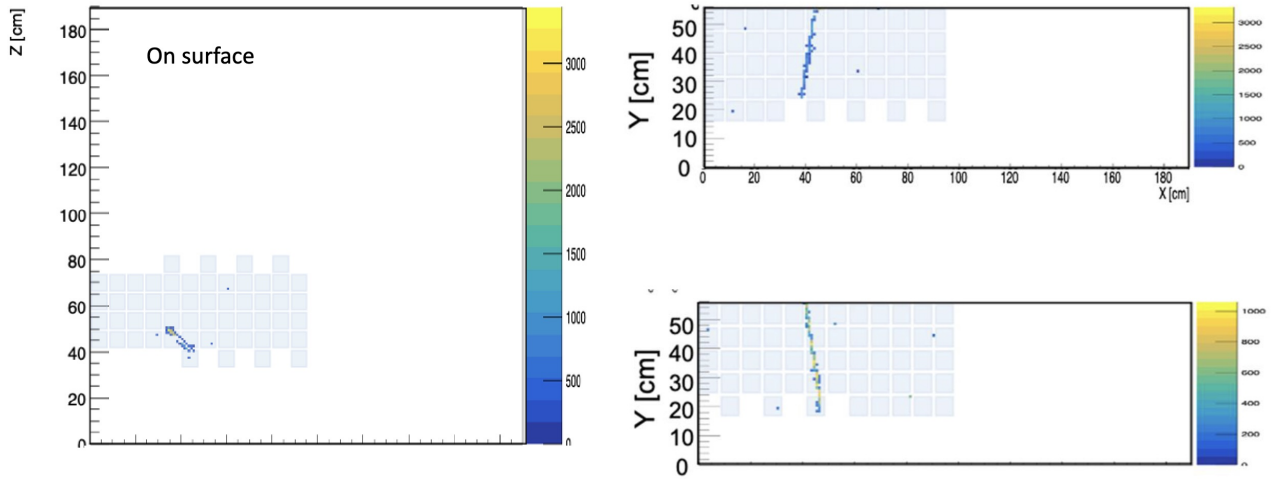

Figure 4.30: First observed cosmic muon in SFGD.

designed. The goal is to reduce the test time of each FEB from several hours down to under 30 minutes and automate the process to require very little manpower. A new signal injection board, Kaladin, that can inject 256 test signals into FEB is designed for this purpose. Kaladin itself has been tested with a commercial electronic readout board to make sure the all signal lines from Kaladin are uniform, linear and have minimal crosstalk. Quality check test bench is developed at University of Geneva using Kaladin. Various tests are prepared to make sure FEBs are up to the standard and test is optimized to take approximately 15 minutes per board. Once the testing scheme is established another test bench is prepared to keep up with number of FEBs needed to be tested. Using the test bench made with Kaladin board, we were able to reduce the testing time of each FEB to less than 15 minutes which our goal when we planned the test bench. The overall testing of full FEB was done in time for them to be assembled in SFGD. The ND280 detector with new SFGD has started taking neutrino beam data from November 2023.

Chapter 5

Muon Neutrino CC1π^+ analysis for upgrade detector

The ND280 upgrade detector enables us to study neutrino interactions in detail. As described in chapter 1, expected performance of CC1π^+ measurement with SFGD is evaluated. This section explains the analysis method of this study, newly developed reconstruction tools and evaluation of the performance of CC1π^+ measurement. A comparison of the performance of upgrade near detector to current near detector is also discussed.

5.1 Analysis method of CC1π^+ with SFGD

CC1π^+ interactions will have a lepton and a positive pion in the final state. Here we select events with muon neutrino(ν_μ) CC interaction vertex in SFGD and muon going into forward TPC(TPC1) and the pion stopping in SFGD as shown in Fig. 5.1. A stopping π^+ decay gives a mono-energetic μ^+(around 20 MeV/c) which decays into a positron within a few mm of pion decay point. In SFGD, where the cube size is 1 cm^3, both π^+ and μ^+ decays happen within one or two cubes therefore muon track cannot be reconstructed. The pion is then identified by associated muon decay time by looking for a positron. Positron from μ^+ decay is detected with delayed signal. SFGD also has excellent track resolution which allows us to make sure π^+ and positron tracks are connected to each other.

This analysis is a continuation of my master's thesis, where we used decay electron signal to identify muon and pion tracks when they are stopping in SFGD. This study was conducted using Monte-Carlo events generated using GEANT4 with SFGD geometry. Momentum range between 0 and 600 MeV/c of μ^- and π^+ generated uniformly in momentum space inside SFGD volume. The performance of particle identification with SFGD was studied. The reconstructed track pairs are selected if ending and starting points are within 1 cube separation. This makes sure that the parent and decay electron tracks are connected to each other. Among the selected track pairs the tracks with energy deposition time difference of more than 50 ns are identified as primary muon(pion) and secondary electron. The selection efficiency is tested by comparing selected tracks with true trajectory information. The results of this study is summarized in Table. 5.1. It shows the selection applied on π^+ and μ^- tracks together and using the explained criteria $\sim$89% of the decay electrons and their respective parent tracks are identified.

In this thesis, the above method is implemented in T2K ND280 analysis. Performance of CC1π^+ measurement with SFGD is studied.

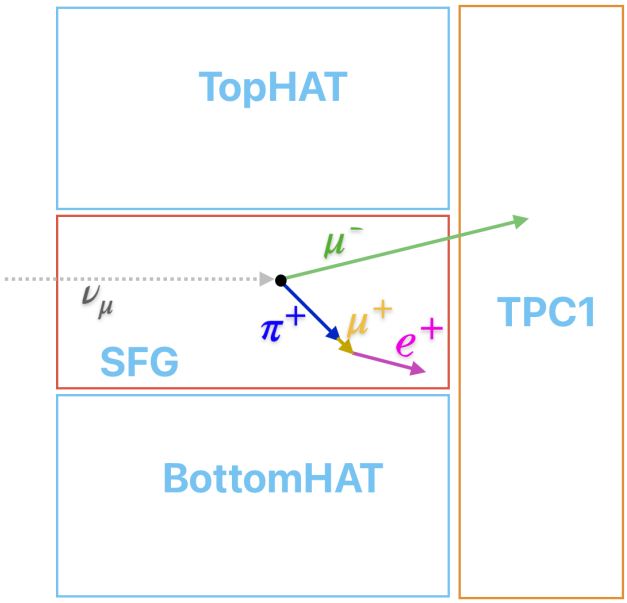

Figure 5.1: Event topology selected in this analysis.

Table 5.1: Decay electron selection results for a simulated sample of μ^- and π^+ as primary particles. Track pairs with more than 50 ns time difference are required.

Time cut (ns)	**50**
No selection	2000
FV (end point of track within SFGD volume)	947
True decay electron produced	647
Reconstructed decay electrons	575
Efficiency	0.89

5.2 Simulation and software tools used for $CC1\pi^+$ selection study

This analysis is performed using software tools which includes ROOT[28], NEUT[29], GEANT[30] and many other tools developed specifically for ND280 simulation, reconstruction and analysis. We used simulated events in this study to understand the potential improvement of our physics analysis using new detectors that are being introduced into ND280. For this purpose, neutrino interactions are generated using NEUT event generator with T2K flux as input. The outgoing particles from the neutrino interactions are then used to make events in upgrade near detector (ND280) geometry using GEANT4 particle simulator. The detector configuration used in this simulation contain all the detectors that are part of upgraded ND280 (SFGD, HATs, FGDs, TPCs). Using the information from GEANT4 simulation, we simulate the electronics readout of each detector to convert the deposited energy into electronics output format. In the reconstruction stage, the electronics information is used to build tracks and clusters in each detector using various techniques that will be explained later. Finally, reconstructed events in each detector is combined to make the full event and appropriate physics cuts are applied for

identifying $CC1\pi^+$ event. Event reconstruction and selection criteria tools for SFGD are newly developed where I contributed significantly together with SFGD reconstruction group.

The general flow of analysis is shown in Table. 5.2, the output from previous tool is used as input for the next tool.

Table 5.2: Software tools used for $\nu_\mu CC1\pi^+$ analysis.

Step	Purpose	Tool used	Input(+previous step output)	Output
Step 1	Generate ν_μ events	NEUT	T2K beam flux and neutrino interaction target elements	Interaction vertex, primary track information
Step 2	Simulate particle tracks	Geant4	ND280 detectors geometry with material composition	Track propagation, energy deposition and time
Step 3	Simulate electronics readout	detResponse	Electronics properties	Electronics output mimicking real beam events
Step 4	Reconstruct events	eventRecon		Reconstructed tracks, clusters
Step 5	Perform physics analysis	highLand		PID and event topology

5.2.1 Generate ν_μ events

NEUT is a neutrino event generator that simulates neutrino interactions with matter. These interactions can happen in several ways such as interaction with proton, neutron or nucleus and resulting particle can vary depending on the cross-section of that particular mode of interaction. NEUT version 5.6.0.0 is used for this study.

ν_μ events are generated using T2K beam flux with ND280 upgrade as the detector including magnet. This generates neutrino events according to the interaction cross-section. The resulting events contain interaction mode and vertex information along with outgoing particle information such as PID, momentum, direction.

5.2.2 Simulate particle tracks

Geant4 is a Monte-Carlo simulation toolkit developed for simulating particles going through matter. It is developed in C++ language and has applications in various fields of Physics including High Energy, Nuclear, Accelerator and Medical Physics. Geant4 version 4.10.1.03.03 is used in this study.

The simulation setup for near detector geometry is made with Geant4 package and configuration of geometry of the upgraded ND280 which includes SFGD and HATs are implemented. The geometry configuration contains the full description of detectors such as material, their location in the coordinate system of the ND280. This analysis is mainly focused on the SFGD, so the parameters used in the simulation are summarized in Table. 5.3. Along with the detector configuration, Genat4 needs to be given particles that traverse the detector volume and this is done by providing the output file from NEUT with neutrino events.

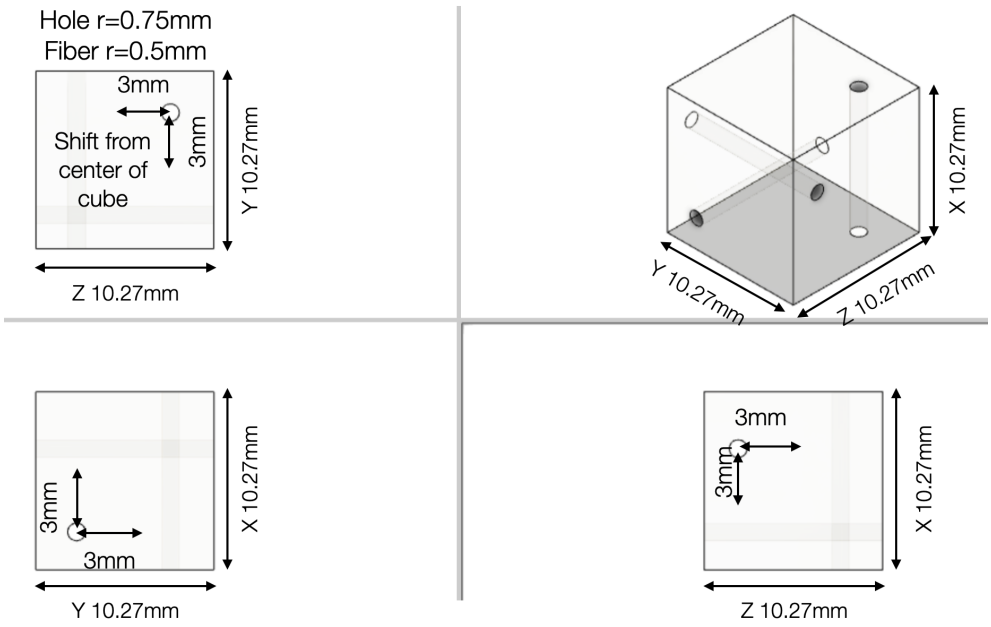

Figure 5.2: SFGD Cube dimensions.

Item	Parameter	value
Cube	Count(nX,nY,nZ)	182,56,184
	Dimensions(X,Y,Z)	10.27 mm,10.27 mm,10.27 mm
	Reflective layer coating	0.1 mm
	Fiber hole radius	0.75mm
	Material	polystyrene doped with 1.5% of paraterphenyl (PTP) and 0.01% of POPOP
	density	1.05 g/cm^3
Fiber	Radius	0.5mm
	Material	Polystyrene (PS)
	Refractive Index	1.59
	Density	1.05 g/cm^3

Table 5.3: Cube and fiber parameters used for the simulations.

Geant4 simulates the propagation and secondary interactions of the particles from neutrino interaction in detector. The energy deposition and time of tracks are recorded in the 1 mm steps throughout the detector. At the end of simulation, we will have all the track information including their energy deposition in each SFGD cube.

5.2.3 Electronics readout simulation

Electronics readout simulation takes the simulated energy deposition, converts it into number of photons and propagate that information through electronics. In SFGD, the deposited energy is in the form of photons produced in the scintillator cubes. Electronics readout simulation contains three main steps:

1. Energy to photon conversion: Deposited energy is converted to photon number and crosstalk to neighboring cubes ($\approx 3\%$) is applied based on beam test results.

2. Photon propagation in wavelength shifting(WLS) fibers: Photons passage in fibers is calculated using probability of photons entering the fibers, fiber attenuation and trapping efficiency. Travel time of photon is calculated using distance of MPPCs from cube and speed of light in fibers.

3. MPPC photon detection: MPPC photon detection efficiency(PDE), taken from data sheet of the MPPC we use, is applied on each photon that arrives at MPPC.

The output analog signal from MPPC is recorded by SFGD electronics discussed in Chapter 4. SFGD contains 3 planes of MPPC readouts, so a cube with energy deposition will have readout in 3 corresponding MPPCs.

5.2.4 Event reconstruction

The event reconstruction software package for ND280 will reconstruct events taking place inside SFGD and receives inputs from electronics simulation. Here the event reconstruction happens using input from MPPC readout information. The algorithms inside SFGD are applied on the input one after another, each taking the previous algorithm's output as its input. The algorithms which I developed together with SFGD reconstruction group are introduced from here on. Some of these reconstruction tools are summarized in my masters thesis[31].

Hit reconstruction - This step takes the 2D MPPC readout information and combines them to rebuild 3D cube hits. Important subroutine here is the charge sharing, which is being optimized currently, which assigns the charge to the cubes the fiber readout passing through based on the charge deposition near that cube. This involves a minimization function whenever a fiber passes through multiple cubes with energy deposition.

Hit Clustering - A clustering algorithm called DBSCAN is used to identify the nearby hits. The algorithm takes a distance parameter(1.5 cm) and minimum number of points(3) in a cluster as input to group the cube hits. It then recursively finds the neighbors for a point within the cluster radius distance and groups them together. Once all the points are either clustered or determined as isolated from the rest of the points, each point is checked whether the number of points within its cluster radius distance is more than minimum number of points parameter. Points satisfying both conditions are grouped into their respective clusters and others are treated as noise.

Hit Ordering - Once the hits are clustered based on the distance, density and hit times, each cluster is then ordered using Minimum Spanning Tree (MST) algorithm. This step is designed to store hits in order based on the distance between them. It starts by finding outermost hits and traverses to its nearest hit, and from there to the next the nearest hit and so on, while storing the hits in that order. When it hits a branch, it takes the shortest path and goes on. Once it finishes visiting all hits in a branch, it traverses back until it finds a hit that is not visited. The algorithm ends once all the hits are visited.

Kink Finding - Kink or branching point finding is implemented to find two or more tracks that are clustered together and identify secondary tracks traveling in a different direction from its parent track. These tracks form a kink-like topology at the point of two tracks boundary. The method finds kink by checking how much the hit is deviating at each point along the track. First, the directional vector from the first hit to the last hit is calculated. Then, directional vector from each hit to the final hit is calculated in order along the track, and search for the

maximum deviation point, "kink-point". If the deviation is larger than a threshold of 2 cm, and the two tracks divided at the kink point have track lengths longer than a threshold length of 6 cubes, the track is broken at the kink point to reconstruct two tracks.

Track building - This step is used to create a smooth track from the previous algorithm. Using positions of three successive hits in the cell-based track, position and direction of a track segment is calculated. This is done from the first cell to the last cell of the cell-based track, and results in a series of track segments which gives position and direction of a physical track object at each point.

Track position - During the track building process, track position is calculated for each segment of the track using the expected position of the track taking the neighboring segments into account. This method gives a more accurate position of the track instead of default center of the cube position.

Output from reconstruction contains reconstructed tracks and hits with position, direction, energy deposition and time.

5.2.5 Perform physics analysis, Highland

First step is to combine all the reconstructed information from the detectors to make an event for physics analysis. This process takes place in the Highland package of ND280 software. Since tracks can have reconstructed information in multiple detectors, there is a track matching algorithm that takes care of this by looking for tracks in adjacent detectors with similar start/end point in first/second detectors along with same direction. If such tracks exists they are combined to make one track. PID algorithms developed using particle gun studies and boosted decision trees are used to separate muon like and proton tracks. The selection uses many tools that are developed to identify various neutrino event information from the reconstructed event. The selection tools are functions applied on the reconstructed event to identify the required event.

Table 5.4: Number of muon neutrino events in various categories in SFGD.

ν_μ events in SFGD	count
Total	180809
Charged current interaction	134252
μ going into TPC1	46847
μ going into TPC1 + π^+ stopping in SFGD	7643

5.3 Event selection of Charged Current interaction in SFGD

In order to study the performance of CC1π^+ measurement with SFDG, first charged current interaction in SFGD are selected by requiring a long muon track reconstructed in SFGD and TPC1. We use the reconstructed information of events such as energy deposition and time information of the tracks in various detectors to filter out the events that are not CC events occurred in SFGD. Flow chart of selection steps is shown in Fig. 5.4. Figure 5.3 shows the distribution of the number of events in each detector in which muon tracks from $\nu_\mu CC1\pi$ interaction passes.

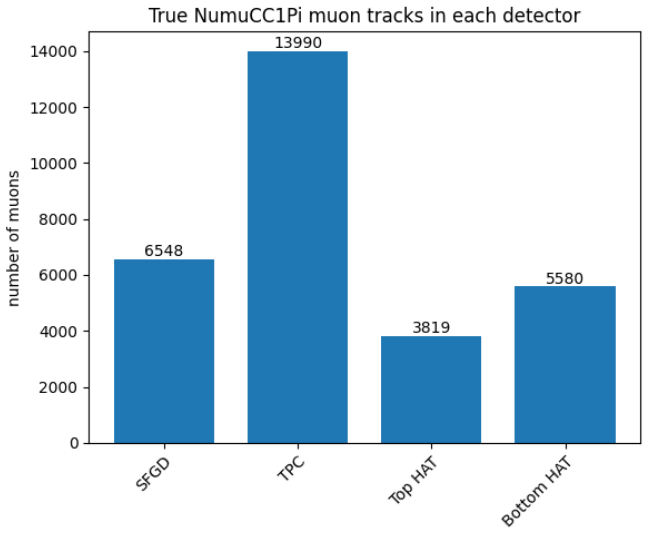

Figure 5.3: Distribution of the number of events in each detector in which muon tracks from $\nu_\mu CC1\pi$ interaction passes. In case of SFGD, muon stopped in SFGD.

An event with $CC1\pi^+$ topology should have a muon and a positive pion in the final state, as explained before the muon should start on SFGD and travel into forward TPC whereas pion should stop and decay inside SFGD. During the selection, we can identify such events by looking at number of tracks in the event (muon, pion and decay electron from pion) and time difference between pion and decay electron due to decay time. Such characteristics of events are used to as cuts in the selection steps explained in this section. At the beginning of the selection we start with full sample and cut by cut we reduce the number of events, this reduction increases the purity of our selection but at the same time reduces the efficiency.

5.3.1 Event quality

This step is used in case of beam data to make sure event is with correct data readout from detector electronics flags to indicate the event is clean without any readout errors. As for the Monte-Carlo sample, this step does not have any function.

5.3.2 Track multiplicity

Each event is checked for minimum one track before performing any selection to save the computational time, here we want at least one track in SFGD presumably muon track from neutrino interaction.

5.3.3 SFGD escaping muon cut

In this step, one muon like track starting in SFGD and passing through TPC1 is required. We select the longest track among the several reconstructed track candidates in ND280. We then require that particle to be muon like, and it should start from SFGD and pass through TPC1. This track is saved as "primary muon" of the event.

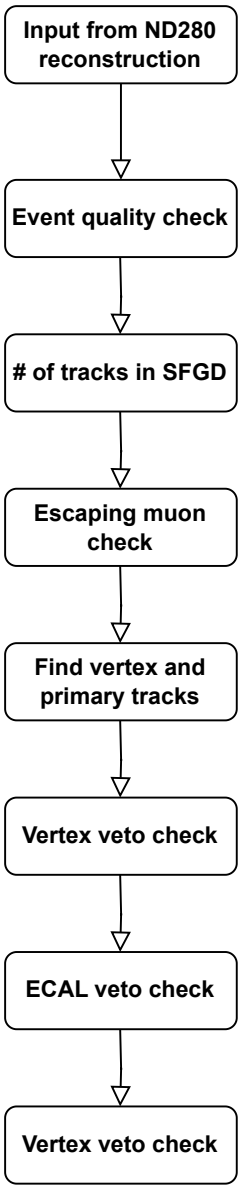

Figure 5.4: Selection steps for charged current event detection in SFGD. "Input from ND280 reconstruction" means output from Step 4 in Table. 5.2.

5.3.4 Find primary vertex and Vertex tracks

Once primary muon is identified, the starting point of the muon track is considered as the event vertex. The vertex has to be within the fiducial volume (FV) of SFGD, where FV is defined as the volume excluding final 2 cube layers of SFGD, otherwise that events will be rejected. All the tracks starting from within 3 cm of the vertex point are considered as "primary tracks" of the event.

5.3.5 Vertex and ECAL veto tracks

It is possible for tracks produced outside the detector volume to stop inside the detector, this behavior creates a fake event and can be identified using time information of the track to get the track direction. Such events are rejected in this step.

5.4 Event selection of CC1π^+ interaction in SFGD

Up to here we selected CC events by identifying muon track and the vertex of the event. In order to categorize event as CC1π^+ we check if the event contains a π^+ candidate in primary tracks. We have 2 sets of tracks in the event:

- Primary tracks - tracks connected to the reconstructed vertex (other than reconstructed muon),
- Non-primary tracks - All other tracks reconstructed in SFGD.

As we discussed in the previous subsection, charged pion is identified using delayed signal. Our goal is to find the positron that is created from $\pi^+ \to \mu^+ \to e^+$ decay, which should be part of non-primary tracks and connected to one of the primary tracks due to short decay μ^+ (∼few mm).

5.4.1 Primary contained track

In this step, we select the events with π^+ stopping in SFGD. We look for events with at least one primary track contained in SFGD, which are tracks with no hits in the last two layers of SFGD. Figure 5.5 shows the distribution of the number of events in each detector containing pion tracks from CC1π^+ events where neutrino event takes place in SFGD based on true information. Most of the CC1π^+ events in SFGD have pion fully contained in SFGD.

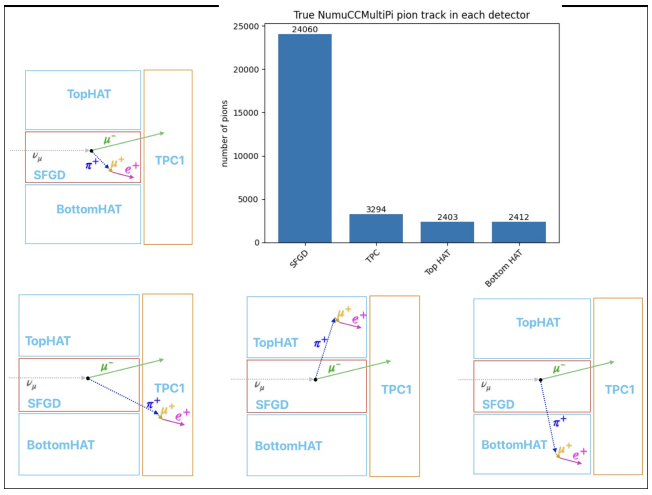

Figure 5.5: Distribution of the number of events in each detector containing pion tracks from CC1π^+ events where neutrino event takes place in SFGD based on true information.

5.4.2 Delayed particles

The key identifier for stopping π^+ is that it decays into μ^+ which decays into e^+. The two decay chains have decay times of 26 ns and 2.2 μs in scintillator medium. Based on my master's thesis study and expected performance of the electronics we require more than 30 ns of time difference between primary and non-primary tracks to identify possible delayed (Michel) positron.

We consider all possible combinations of primary and non-primary tracks which satisfy the time difference condition. Such track pairs are saved for next step.

5.4.3 One pion cut

Another key signature of a stopping pion decay is that the muon decayed from pion is mono energetic and will travel for only a few mm. This means muon from pion will almost always decay in the same scintillator cube as pion since cube size is $1cm^3$. This means the eventual decay positron should also be connected to the primary pion track. All the track pairs with 30 ns time difference from previous step are then compared to see if they are connected within 3 cm. The track pairs that qualify for both conditions are paired as π^+ and e^+.

5.5 Results and improvements from ND280

As explained in Section 5.4, we developed selection cuts to identify the ν_μCC1π+ events with muon going into forward TPC and pion stopping in SFGD. Here the efficiency of selection is defined as

$$\frac{\text{Number of CC1}\pi^+ \text{ events selected with our selection criteria with reconstruction}}{\text{Number of true CC1}\pi^+ \text{ events generated in SFGD FV with topology A}} \tag{5.1}$$

Where the Topology A is muon from interaction going into TPC1 and π^+ stopping in SFGD. Here, the selection criteria are as described in section 5.4.

Whereas, purity is defined as

$$\frac{\text{Number of CC1}\pi^+ \text{ events selected with our selection criteria with reconstruction}}{\text{Number of events with our selection criteria}} \tag{5.2}$$

The denominator for purity calculations take all the selected events which include all the possible CC categories e.g. CC0π, CC other, background and in the numerator we use true event category information to calculate number of CC1π^+ events.

The goal is to adjust cuts values to maximize the purity while keeping efficiency as high as possible. Figure 5.6 shows the efficiency and purity at each step of the selection. When we made this plot we already require the event topology where muon is going into TPC1 is reconstructed. This is the reason why efficiency is 100 % up to the "muon escaping from SFGD cut". Table. 5.5 summarizes the efficiency and purity step by step. At the moment our selection has 59.4% efficiency and 68.2% purity. We will discuss the comparison with existing FGD in ND280 in section 5.6.

Table 5.5: Summary of efficiency and purity of CC1π^+ selection.

Cut	Events	Efficiency(%)	Purity(%)
No cut	4459	100	24.7
Event quality	4459	100	24.7
SFGD track multiplicity (# tracks $\geq$ 1)	4459	100	24.7
Muon escaping from SFGD	4459	100	24.7
Vertex FV	4409	98.9	24.8
Vertex veto	4138	92.8	24.8
ECAL veto	4097	91.9	24.9
Primary track contained(other than muon)	3535	79.3	30.3
One pion cut	2648	59.4	68.2

The distribution and efficiency as a function of the pion angle with beam direction after the pion cut are shown in Fig. 5.7 and 5.8, respectively. The reconstruction efficiency is more

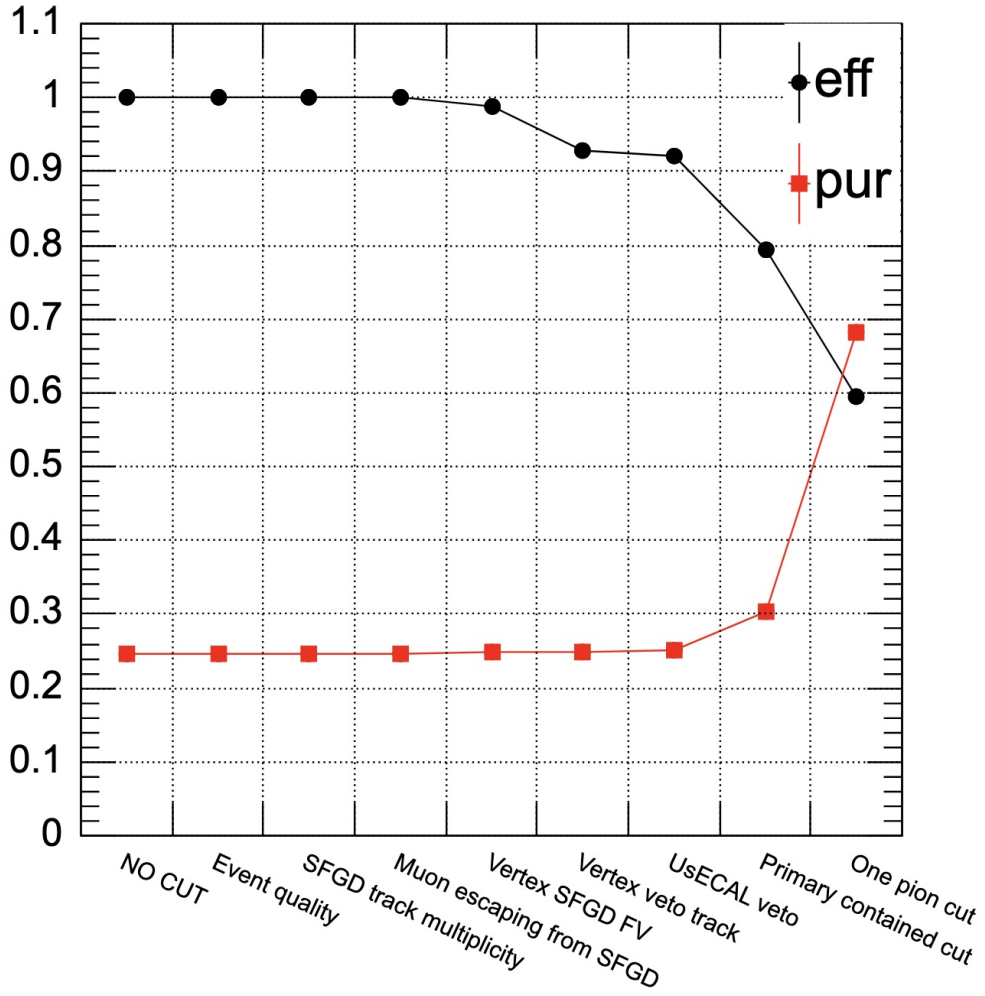

Figure 5.6: Efficiency and purity of the event selection as a function of cuts applied on the ν_μ event sample with interaction vertex inside SFGD.

or less same for all angles of pion tracks with respect to the neutrino beam direction. This is the result of SFGD's uniform geometry. There is a slight increase in efficiency for forward and backward going pions. This behavior could be due to the fact that SFGD is 2 m along the beam direction but only about 56 cm in high angle direction (perpendicular to beam direction) which means forward direction tracks are easier to reconstruct with longer traveling distance.

The distribution and efficiency as a function of the pion momentum after one pion cut are shown in Fig. 5.9 and 5.10, respectively. Since we are only using pions stopping/decaying in SFGD in this study, the size of detector limits the pion momentum we can reconstruct. For a scintillator detector like SFGD with 2 m length the maximum momentum we can expect the track to be is about 300-400 MeV. But in addition to this, pion can also decay in flight. In such cases, the even higher momentum pions can produce muons. There are few events in the 0-50 MeV bin and even with SFGD we don't expect detection for such low momentum tracks as they seldom travel 3 cm required for track reconstruction. In the 50-300 MeV region the efficiency looks as stable and as we expected. Above this region the efficiency goes down mainly due to not being able to reconstruct both pion and michel electron together along with increase in probably pion undergoing inelastic interaction. There are several reasons for this drop in efficiency. One is that the michel electron might be produced near the edge of SFGD where it cannot leave sufficiently long enough track in SFGD to be reconstructed, and other one is

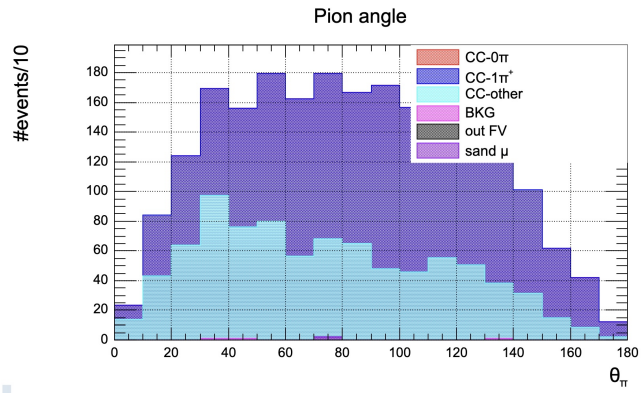

Figure 5.7: Distribution of reconstructed pion angle with respect to beam axis after the final cut.

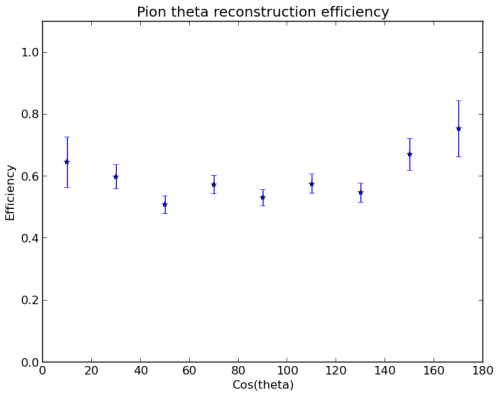

Figure 5.8: Efficiency of pion reconstruction as a function of its angle with respect to beam axis after the final cut.

pions undergoing inelastic interaction will not produce michel electrons. There is an increase in efficiency again above 600 MeV which is most likely statistical fluctuation as the sample I am using do not have enough events with high momentum pions stopping in SFGD.

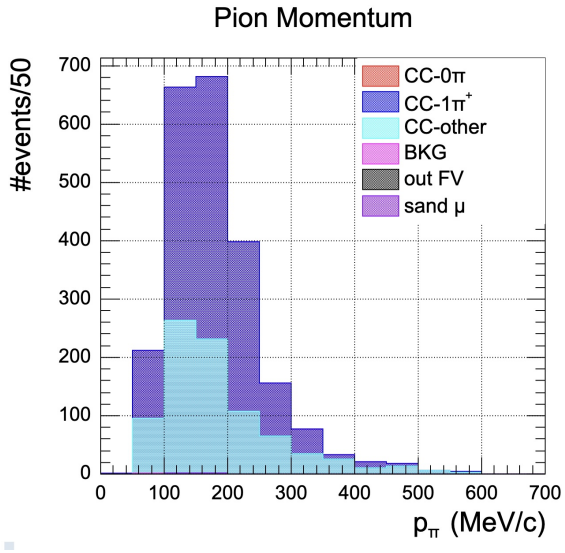

Figure 5.9: Pion reconstructed momentum distribution after final cut.

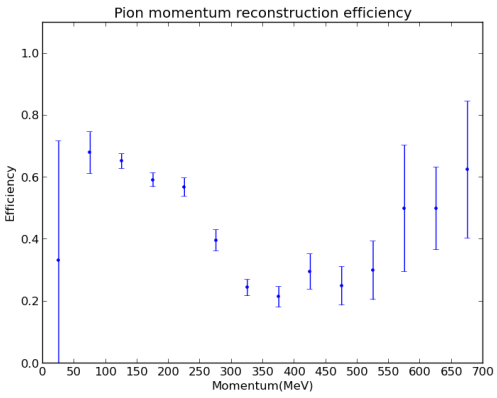

Figure 5.10: Pion reconstructed momentum efficiency after final cut.

The main contamination in the $CC1\pi^+$ event selection comes from CCother events as seen in the previous plots. The main reason for that is because this selection does not have π^0 cuts. CCother events are when there are more than one pion irrespective of whether they are neutral or charged pion. Based on this a CCother event with a π^+ and π^0(s) looks exactly same as $CC1\pi^+$ if we cannot detect π^0s. We are working on implementing π^0 cut using EM shower that comes from $\pi^0 \rightarrow 2\gamma$.

5.6 Discussion

The main goal of this analysis is to understand the performance improvement of SFGD compared to existing FGD. We expect an improvement of high angle efficiency for tracking and momentum reconstruction due to super fine-grained structure of SFGD instead of conventional scintillator bars. Based on this study we evaluate improvements in event reconstruction of SFGD compared to existing FGD in ND280. I will explain those findings here.

5.6.1 FGD pion reconstruction approach

FGD pion reconstruction using michel electron uses delayed hit signal due to decay electron coming from pion. Unlike SFGD, looks for delayed signal out of beam bunch time window. This reduces the efficiency since the hits recorded during subsequent bunches needed to be masked for this selection.

5.6.2 Comparison of FGD and SFGD for track reconstruction

Pion reconstruction has improved for high angle (perpendicular to the neutrino beam direction) compared with FGD from almost zero to 50 % which is expected when we compare scintillator cube structure of SFGD to bar structure of FGD. Momentum reconstruction threshold is also improved from 160 MeV in FGD to 50 MeV in SFGD (Fig. 5.9) for pions. This is again because of SFGD's ability to reconstruct tracks with lengths as small as 3 cm (3 cubes) while FGD requires tracks to traverse 5 cm (5 scintillator planes) for a reconstructed track.

5.6.3 Comparison of FGD and SFGD for pion detection efficiency

In terms of pion reconstruction, both FGD and SFGD use decay time difference. T2K neutrino beam is produced from proton beam coming in regular intervals we call spills and each spill contains 8 bunches each separated by 560 ns. If a delayed positron is produced from pion decay FGD identified it by delayed time hits compared to tracks in beam bunches. To avoid mislabeling positron, FGD analysis implements a masking of 200 ns around each bunch time and only considers hits outside this window for positron tracks. Due to this, FGD loses significant efficiency of π^+ selection with delayed positrons. In SFGD, in addition to delay time hits we also require π^+ and positron tracks to be connected to each other which allows us to use hits from other bunches too without having to worry about misidentifying. Based on this CC1π^+ selection efficiency has improved from $\sim$25% in FGD to $\sim$60% SFGD while purity has improved from $\sim$60% to $\sim$68%.

Chapter 6

Conclusion

The aim of introducing SFGD in T2K Near detector is to improve the systematic uncertainties of the neutrino interaction by utilizing its superior ability of neutrino event reconstruction. CC1π^+ mode of interaction is expected to have improved selection efficiency by utilizing SFGD capabilities.

This thesis work is done during the development of SFGD newly designed electronics and analysis software. The test bench was designed and developed to test large number of new electronic boards ($\sim$240) for SFGD. This work is successfully completed in time and electronics are installed in SFGD.

Analysis study to evaluate the selection capabilities of CC1π^+ interaction in SFGD is performed using Monte Carlo sample of ν_μ beam generated using T2K flux parameters and ND280 detector geometry. The reconstruction tools for SFGD are newly made for the 3D event reconstruction from MPPC readouts. According to our simulations, we expect an improvement in CC1π^+ detection efficiency of 60% using my selection method with a purity of 68%. This is a clear improvement from existing FGD's efficiency of 25% and purity of 60%.

In addition to this, we also confirmed SFGD is indeed very much capable of reconstructing large angle tracks due to its 3D isotropic structure. Momentum reconstruction threshold improved compared FGD as we are able to probe down to 50 MeV momentum pions, previously we were restricted to about 160 MeV momentum pions using FGD.

There is still a scope for improving this analysis by implementing π^0 cuts to reduce background from CCOther interaction mode and tuning the parameters used in the CC1π^+ selection. The later will be done once we have the beam data to understand the full implication of cut parameters values on efficiency and purity of pion selection.

Bibliography

[1] R. L. Workman et al. "Review of Particle Physics". In: *PTEP* 2022 (2022), p. 083C01. DOI: 10.1093/ptep/ptac097.

[2] W. Pauli. "Dear radioactive ladies and gentlemen". In: *Phys. Today* 31N9 (1978), p. 27.

[3] G. J. Neary and John Douglas Cockcroft. "The beta-ray spectrum of radium E". In: *Proceedings of the Royal Society of London. Series A. Mathematical and Physical Sciences* 175.960 (1940), pp. 71–87. DOI: 10.1098/rspa.1940.0044. URL: https://royalsocietypublishing.org/doi/abs/10.1098/rspa.1940.0044.

[4] C. L. Cowan et al. "Detection of the Free Neutrino: a Confirmation". In: *Science* 124.3212 (1956), pp. 103–104. DOI: 10.1126/science.124.3212.103. eprint: https://www.science.org/doi/pdf/10.1126/science.124.3212.103. URL: https://www.science.org/doi/abs/10.1126/science.124.3212.103.

[5] B. T. Cleveland et al. "Measurement of the solar electron neutrino flux with the Homestake chlorine detector". In: *Astrophys. J.* 496 (1998), pp. 505–526. DOI: 10.1086/305343.

[6] K. Eguchi et al. "First results from KamLAND: Evidence for reactor anti-neutrino disappearance". In: *Phys. Rev. Lett.* 90 (2003), p. 021802. DOI: 10.1103/PhysRevLett.90.021802. arXiv: hep-ex/0212021.

[7] Y. Fukuda et al. "Evidence for oscillation of atmospheric neutrinos". In: *Phys. Rev. Lett.* 81 (1998), pp. 1562–1567. DOI: 10.1103/PhysRevLett.81.1562. arXiv: hep-ex/9807003.

[8] Q. R. Ahmad et al. "Direct evidence for neutrino flavor transformation from neutral current interactions in the Sudbury Neutrino Observatory". In: *Phys. Rev. Lett.* 89 (2002), p. 011301. DOI: 10.1103/PhysRevLett.89.011301. arXiv: nucl-ex/0204008.

[9] P. F. de Salas et al. "2020 global reassessment of the neutrino oscillation picture". In: *JHEP* 02 (2021), p. 071. DOI: 10.1007/JHEP02(2021)071. arXiv: 2006.11237 [hep-ph].

[10] Sunny Vagnozzi. "Weigh them all! - Cosmological searches for the neutrino mass scale and mass ordering". PhD thesis. June 2019.

[11] Teppei Katori. "Meson Exchange Current (MEC) Models in Neutrino Interaction Generators". In: *AIP Conf. Proc.* 1663.1 (2015). Ed. by H. Da Motta, Jorge G. Morfin, and M. Sakuda, p. 030001. DOI: 10.1063/1.4919465. arXiv: 1304.6014 [nucl-th].

[12] K. Abe et al. "The T2K experiment". In: *Nuclear Instruments and Methods in Physics Research Section A: Accelerators, Spectrometers, Detectors and Associated Equipment* 659.1 (2011), pp. 106–135. ISSN: 0168-9002. DOI: https://doi.org/10.1016/j.nima.2011.06.067. URL: http://www.sciencedirect.com/science/article/pii/S0168900211011910.

[13] *Accelerator technical design report for high-intensity proton accelerator facility project, J-PARC*. 2003. URL: https://cds.cern.ch/record/747209.

[14] Y. Fukuda et al. "Measurements of the Solar Neutrino Flux from Super-Kamiokande's First 300 Days". In: *Physical Review Letters* 81.6 (Aug. 1998), pp. 1158–1162. ISSN: 1079-7114. DOI: 10.1103/physrevlett.81.1158. URL: http://dx.doi.org/10.1103/PhysRevLett.81.1158.

[15] K. Abe et al. "Measurements of neutrino oscillation parameters from the T2K experiment using 3.6×10^{21} protons on target". In: *Eur. Phys. J. C* 83.9 (2023), p. 782. DOI: 10.1140/epjc/s10052-023-11819-x. arXiv: 2303.03222 [hep-ex].

[16] Christophe Bronner. *Accelerator Neutrino I_Recent results from T2K*. June 2022. DOI: 10.5281/zenodo.6683821. URL: https://doi.org/10.5281/zenodo.6683821.

[17] Ko Abe et al. "Sensitivity of the T2K accelerator-based neutrino experiment with an Extended run to 20×10^{21} POT". In: (July 2016). arXiv: 1607.08004 [hep-ex].

[18] K. Abe et al. "Updated T2K measurements of muon neutrino and antineutrino disappearance using 3.6×1021 protons on target". In: *Phys. Rev. D* 108.7 (2023), p. 072011. DOI: 10.1103/PhysRevD.108.072011. arXiv: 2305.09916 [hep-ex].

[19] T. Sekiguchi et al. "Development and operational experience of magnetic horn system for T2K experiment". In: *Nuclear Instruments and Methods in Physics Research Section A: Accelerators, Spectrometers, Detectors and Associated Equipment* 789 (July 2015), pp. 57–80. ISSN: 0168-9002. DOI: 10.1016/j.nima.2015.04.008. URL: http://dx.doi.org/10.1016/j.nima.2015.04.008.

[20] Ke. Abe et al. "Measurements of the T2K neutrino beam properties using the INGRID on-axis near detector". In: *Nuclear Instruments & Methods in Physics Research Section A-accelerators Spectrometers Detectors and Associated Equipment* 694 (2012), pp. 211–223.

[21] K. Kin et al. "New experiment at J-PARC to measure the muon neutrino cross section ratio between water and hydrocarbon". In: *J. Phys. Conf. Ser.* 888.1 (2017), p. 012125. DOI: 10.1088/1742-6596/888/1/012125.

[22] M. Antonova et al. "Baby MIND: A Magnetised Spectrometer for the WAGASCI Experiment". In: *Prospects in Neutrino Physics*. Apr. 2017. arXiv: 1704.08079 [physics.ins-det].

[23] K. Abe et al. "T2K ND280 Upgrade - Technical Design Report". In: (Jan. 2019). arXiv: 1901.03750 [physics.ins-det].

[24] Yury Kudenko. "Physics and Status of SFGD Detector for T2K Experiment". In: *Moscow Univ. Phys. Bull.* 77.2 (2022), pp. 375–378. DOI: 10.3103/S0027134922020564.

[25] Hamamatsu. *MPPC S13360 series*. URL: https://www.hamamatsu.com/jp/en/product/optical-sensors/mppc/mppc_mppc-array/S13360-1325PE.html.

[26] Weeroc. *Citiroc1A data sheet*. URL: https://www.weeroc.com/my-weeroc/download-center/citiroc-1a/89-citiroc1a-datasheet-v2-53/file.

[27] CAEN. *CAEN-1702: 32 channel SiPM readout board*. URL: https://www.caen.it/products/a1702/.

[28] Rene Brun et al. *root-project/root: v6.18/02*. Version v6-18-02. June 2020. DOI: 10.5281/zenodo.3895860. URL: https://doi.org/10.5281/zenodo.3895860.

[29] Yoshinari Hayato and Luke Pickering. "The NEUT neutrino interaction simulation program library". In: *Eur. Phys. J. ST* 230.24 (2021), pp. 4469–4481. DOI: 10.1140/epjs/s11734-021-00287-7. arXiv: 2106.15809 [hep-ph].

[30] S. Agostinelli et al. "Geant4—a simulation toolkit". In: *Nuclear Instruments and Methods in Physics Research Section A: Accelerators, Spectrometers, Detectors and Associated Equipment* 506.3 (2003), pp. 250–303. ISSN: 0168-9002. DOI: https://doi.org/10.1016/S0168-9002(03)01368-8. URL: http://www.sciencedirect.com/science/article/pii/S0168900203013688.

[31] Mahesh Jakkapu. "Particle identification performance of SuperFGD in T2K near detector upgrade". In: SOKENDAI Master thesis (2020).